



Elementary Reactive Processes of Nitrogen and Hydrogen on Metal Surfaces: A Theoretical Study

Mohamed Ahmed Nosir
CENTRO DE FÍSICA DE MATERIALES
Centro Mixto CSIC-UPV/EHU

Doctoral Thesis submitted in accordance with the requirements of the University of the Basque Country for the Degree of Doctor in Physics

Doctoral Supervisor
Dr. Ricardo Díez Muño

December 16, 2016

To
My Parents
Dina
Hamsa & Ghada
Mustafa, Sherief
and
Smiley faces around

Acknowledgements

I would like to express my gratitude to my supervisor *Dr. Ricardo Díez Muíño*, for being an outstanding advisor and excellent professor, as well as for his constant encouragement, support, and valuable suggestions. He has been everything that one could want in an advisor. He is the best person I have met ever in my life.

Besides my supervisor, I would also like to acknowledge my collaborators *Dr. Gisela A. Bocan*, and *Dr. Ludovic Martin-Gondre*, for their contribution to the main part of the work presented in my thesis. They facilitated my work by their rich discussions, insight comments, and valuable advices. I would like also to thank our collaborators *Dr. Pascal Larrégaray*, *Dr. Cedric Crespos*, and *Dr. Rémi Pétuya* for their help during my stay in the University of Bordeaux.

Many, many thanks go to my colleagues: *Giuseppe*, *Itziar*, *Natalia*, *Ohiana*, and *Ivor*. Thanks for your quiet atmosphere, continuous help and encouragement.

Special thanks for all friends: *Salil*, *Gerardo*, *Luisa*, *Elizabeth*, *Petra*, and *Eneritz*. Those were nice years having you around, and being often close.

Deep thanks for *Zakaria*, *Ahmed*, *Afaf*, *Talaat*, and *Gamal*, the great Egyptian family. They were always there, ready to help. Thanks for sharing all these good moments.

I would like to express my thanks to my friends in Egypt, for their never-ending friendship.

I would like to express my deep gratitude to *Dr. Mohamed Abdelmajed*, for his continuous encouragement and support during the last years.

I am also very grateful to my brothers *Mustafa* and *Sherief*, and to my sister *Raghda*, as well as *Ahmed*.

Many hugs go to my nieces *Hamsa* and *Ghada*. They are the deep smile I have in my life.

I am very much indebted to my wife *Dina*, for her support, for being close, for being my best friend, and for being patient during all the hard days. I love you.

I am deeply and forever grateful to my *Parents* for their love, support and encouragement throughout my entire life. *Papa*, you taught me that a good education gives me wings and, by personal example, instilled in me this love of learning. Thanks for believing in me, for taking care of me, and for helping me; never-ending thanks for you.

Mama, you are the brightness of my life, you are the big reason behind this degree. I owe you my life.

To those who did not feel appreciated at that time - I apologize.

Shokran, Eskerrik Asko, Gracias, Thanks for all the people who one way or another contributed to the success of this work.

Contents

1	Introduction	1
1.1	Heterogeneous Catalysis	2
1.2	Reactions at Surfaces	3
1.3	Metal Surfaces	5
1.4	Experimental Techniques	7
1.5	Molecular Dynamics Simulations	7
1.6	Purpose and Structure of this Work	8
2	Density Functional Theory	11
2.1	The Many-Body Problem	12
2.2	Born-Oppenheimer Approximation	14
2.3	Density Functional Theory	16
2.3.1	Thomas-Fermi Model	17
2.3.2	Hohenberg-Kohn Theorems	18
2.3.3	Kohn-Sham Formalism	20
2.4	Exchange-Correlation Functionals	21
2.4.1	Local Density Approximation	23
2.4.2	Generalized Gradient Approximation	24
2.4.3	Meta Generalized Gradient Approximation	25
2.4.4	Hybrid Functionals	26
2.5	Implementation of Density Functional Theory	27
2.5.1	Plane Waves Basis Set	27
2.5.2	Pseudopotential Approximation	29
2.5.3	K-points Sampling	32
2.5.4	Numerical Calculations - VASP	33

CONTENTS

3	Theory of Gas/Surface Dynamics	37
3.1	Continuous Potential Energy Surface	38
3.1.1	Corrugation Reducing Procedure	39
3.1.2	Flexible Periodic London-Eyring-Polanyi-Sato	42
3.2	Classical Dynamics Simulations	45
3.2.1	Generalized Langevin Oscillator	46
3.2.2	Sampling the Initial Conditions	49
3.2.3	Final Channels of the Dynamics	49
3.3	Summary	50
4	Fe(111) Surface Slab Relaxations	53
4.1	Methodology	54
4.2	Relaxation of the Fe(111) Surface Slab	55
4.3	Summary	59
5	Potential Energy Surfaces of Nitrogen on Iron	61
5.1	Electronic Structure Calculations	62
5.2	N/Fe(111) Potential Energy Surface	63
5.3	N ₂ /Fe(111) Potential Energy Surface	65
5.3.1	System Geometry	67
5.3.2	Potential Energy Surface Properties	70
5.4	Summary	74
6	Adsorption Dynamics of Molecular Nitrogen at a Fe(111) Surface	77
6.1	Quasi-Classical Trajectory Calculations	78
6.2	Adsorption Dynamics	79
6.3	Summary	86
7	Dissociative Adsorption Dynamics of Nitrogen at a Fe(111) Surface	87
7.1	Molecular Trapping	88
7.2	Dissociative Dynamics of N ₂ on Fe(111)	88
7.3	Fe(111) versus Fe(110)	96
7.4	Summary	97

8 Isotope Effects in Eley-Rideal Abstraction Dynamics of Hydrogen from Tungsten W(100) and W(110) Surfaces	99
8.1 Methodology	100
8.2 Results and Discussion	102
8.3 Comparison with Experiments	108
8.4 Summary	112
9 Conclusions	115
Appendix A Interpolation Procedures	119
References	127
Resumen	143
Publications	149

CONTENTS

1

Introduction

We are surfaces, we walk on surfaces, we touch surfaces, and we constantly deal with surfaces in our daily life. We are surrounded by atoms and molecules that interact with the surfaces of our body all the time. Have we ever thought that we are a living example of a gas-solid interface? There are numerous examples of interfaces phenomena in everyday life. The corrosion of a coin is due to the interaction between the oxygen in the air and the coin's metal surface. Catalytic converters in cars are based on the reaction of different harmful molecules at surfaces to recombine into less dangerous species. Surface chemistry is able to explain several manifestations of our daily life. Industrially, progress in the understanding of the molecule-surface interactions has fostered applications of substantial economic importance, such as those in the fields of hydrogen storage, semiconductor devices, biomedical devices, and heterogeneous catalysis. Due to its vast practical applications, the modeling of gas-surface interactions has been one of the most attractive scopes in surface science during the last decades. Computational physics and chemistry have become powerful enough to set in motion extensive numerical studies of surfaces and interfaces using first principles [1].

The Nobel Prize in Chemistry awarded to Gerhard Ertl in 2007 for his studies on the detailed description of the sequence of elementary reactions of molecules on solid surfaces set a landmark for surface science in general and for surface chemistry in particular. However, Ertl was not the first Nobel Laureate in the history of catalysis. Wilhelm Ostwald also received the Nobel Prize in Chemistry in 1909 for his studies on catalysis. The Ostwald process for the production of nitric acid was one of the first catalytic processes introduced at industrial scale. The development of a catalyst

1. INTRODUCTION

that could increase the reaction rate of N_2 with H_2 to form ammonia was the reason behind the Nobel Prize in Chemistry awarded to Fritz Haber in 1918. Carl Bosch was able to solve some engineering problems derived from the very high pressure necessary for ammonia synthesis, and received the Nobel Prize in Chemistry in 1931. The basis for understanding the surface reactivity was mainly established by the work of Irving Langmuir, who was awarded the Nobel Prize in Chemistry in 1932. Nevertheless, it was only many decades later that surface chemistry emerged from its black box: thanks to the work of Ertl, we were able to understand many dynamical properties of surface reactions, opening the door for further studies on surface chemistry and its applications.

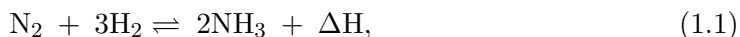
1.1 Heterogeneous Catalysis

Catalysis is the traditional realm of surface chemistry and most of the chemical industry products are made under catalytic processes [2]. In 1835, J. J. Berzelius coined the word 'catalysis' to describe the property of a substance that facilitates the chemical reaction without being consumed in the process. This ability is usually referred as the activity of a catalyst. The broad definition of catalysis also allows the term to be used for materials that slow the rate of a chemical reaction. In chemical reactions, there are quite often several possible products. The catalyst may promote the production of a specific product. This is referred as the selectivity of a catalyst. Heterogeneous catalytic reactions occur on the surface of solid catalysts. These reactions involve some elementary surface chemical processes, such as adsorption of reactants from a reaction mixture, diffusion and reaction of adsorbed species, and desorption of the reaction products. The acceleration of the chemical reaction is due to the reactivity of the surface atoms, which play a role in bond making and breaking, and to the bond rearrangement of the adsorbed molecules [3].

Heterogeneous catalysis is of tremendous practical applications. Approximately 85 - 90 % [2] of the current industrial processes in the chemical, petrochemical, and biochemical industry, as well as in the production of polymers, use catalysis [4]. Among the processes based on heterogeneous catalysis, ammonia synthesis is considered as one of the most important industrial applications. The commercial production of 160 million tons per year and the consumption of ≈ 1 % of the energy generated in the world every year

[5–7], are the raw data that make of ammonia synthesis one of the most attractive processes for both technological applications and scientific research.

The chemical reaction for the ammonia production is the interaction of hydrogen and nitrogen according to the equation:



where ΔH refers to the energy arising from this reaction (i.e., it is an exothermic process). The traditional catalysts used for the ammonia production are iron (Fe) and ruthenium (Ru). Moreover, the synthesis process requires high temperatures and pressures [8]. Since Haber and Bosch designed the first industrial reactor of ammonia synthesis, great efforts have been made to improve the design of the reactor and understand the nature of the catalytic process, and its associated reactions. Concerning the latter, the difficulty is that elementary reactions at surfaces are complex phenomena, which can be highly dependent on minor details of the electronic interaction [1, 9]. A generally accepted conclusion extracted from previous studies is that the dissociative energy of $\text{N} \equiv \text{N}$ is the rate-determining step in the catalytic formation of ammonia at surfaces [10–16]. A large body of research has thus been devoted to the study of fundamental processes of nitrogen atoms and molecules at metal surfaces.

1.2 Reactions at Surfaces

For the creation, improvement, and new design of catalysts at the atomic scale, it is essential to have a detailed knowledge of the dynamical processes that rule the molecular reactions on surfaces [17]. Therefore, the basic principles that govern the geometry and electronic structure of surfaces, as well as the elementary reactions that take place on these surfaces, have to be addressed in detail. In this regard, there are several physical and chemical processes associated with the interaction between diatomic molecules and surfaces. Let us classify them into three main categories [18]:

- (1) **Molecular adsorption (Fig. 1.1):** Defined as a physical process in which the molecule coming from the gas-phase hits the surface and dissipates all or part of its kinetic energy in order to accommodate at least one of its atoms at the surface. There are four mechanisms associated with the molecular adsorption:

1. INTRODUCTION

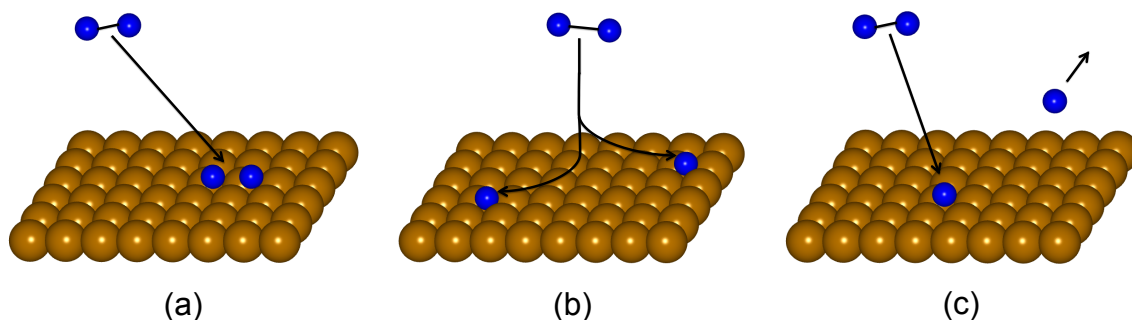


Figure 1.1: Schematic representation of the (a) molecular chemisorption mechanism, (b) dissociative adsorption mechanism, (c) abstraction mechanism, for a diatomic molecule at a surface.

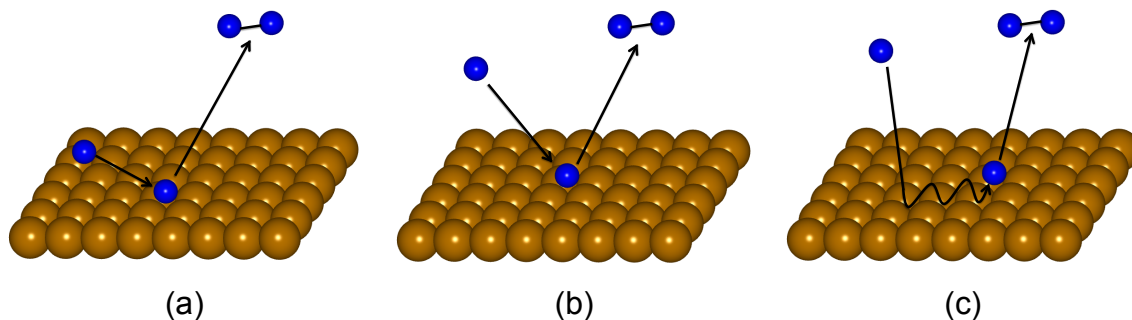


Figure 1.2: Schematic representation of the (a) Langmuir-Hinshelwood mechanism, (b) Eley-Rideal mechanism, (c) Hot-Atom mechanism.

- (a) **Molecular physisorption:** for which the molecule adsorbed at the surface is weakly bound to it, due to van der Waals forces.
- (b) **Molecular chemisorption:** for which the adsorption is characterized by a strong attachment of the molecule to the surface, due to the formation of new chemical bonds (Fig. 1.1.a).
- (c) **Dissociative chemisorption:** in which the molecule breaks its internal bond and its individual atoms, as a result, get adsorbed at the surface (Fig. 1.1.b).
- (d) **Abstraction mechanism:** the molecule breaks its internal bond, one of its atoms becomes adsorbed at the surface and the second atom escapes to the vacuum (Fig. 1.1.c).

- (2) **Molecular desorption (Fig. 1.2):** By definition, it is the opposite of the molecular adsorption process. In this case, some adsorbed atoms or the entire molecule are in thermal equilibrium with the surface and receive sufficient energy to escape from the surface toward the gas-phase. There are three main mechanisms associated with the molecular desorption category:
- (a) **Langmuir-Hinshelwood mechanism:** two individual atoms thermally adsorbed at the surface interact with each other to form a molecule that eventually escapes into the gas-phase (Fig. 1.2.a).
 - (b) **Eley-Rideal mechanism:** an atom coming from the vacuum interacts with an atom adsorbed at the surface and forms a molecule that leaves the surface (Fig. 1.2.b).
 - (c) **Hot-Atom mechanism:** in which an atom approaching the surface from the gas-phase diffuses over the surface without reaching thermal equilibrium, meets and interacts with another atom previously adsorbed at the surface, to form a molecule that desorbs into the gas-phase (Fig. 1.2.c).
- (3) **Molecular scattering:** In this process, a molecule coming from the gas-phase collides with the surface, transfers or gains energy to or from the surface, and is eventually reflected to the vacuum again.

In this thesis work, we will mainly focus on the first and second categories.

1.3 Metal Surfaces

Understanding the catalyst nature is essential for any comprehensive study of the elementary reactions taking place at surfaces, as well as for understanding the surface chemical bonding [19, 20]. Catalysts are developed, in general, for a particular process, for a certain reaction, in a certain reactor, and under certain conditions [2]. In the particular case of heterogeneous catalysis, solids catalyze reactions of molecules in gas or solution.

In gas-solid interfaces, the incoming atoms and molecules may interact with all valence electrons of the surface. Metal surfaces are known to provide a semi-infinite source of electrons at the Fermi level [21]. Moreover, all the transition metals have s electrons

1. INTRODUCTION

and a d -band within few eV of the Fermi level. The occupancy of the d -band varies along the transition metals as the band energy shifts through the Fermi level. Since the d -band can be relatively narrow, bonding and antibonding states can be often created in the interaction of adsorbates with the d -electrons. In other words, the nature of the d -bands often brings about a splitting of the adsorbates resonance into one state with bonding character with respect to the adsorbate and the metal d -states and another state above the d -bands with antibonding character [19]. This feature of transition metal surfaces is ideal for catalysis because of the multiplicity of the degenerate electronic states that can readily donate or accept electrons to or from the adsorbed species [22]. Consequently, the change of reactivity from one metal to another much depends on the occupancy of the d -bands; i.e. the farther to the left in the periodic table, the stronger the chemical bonds to the surface; and the farther down in the periodic table, the weaker the interaction. Thus, in general, the $5d$ metals are more noble than the $4d$ and $3d$ metals.

Furthermore, the chemical reactivity can be enhanced or hindered depending on the particular crystal face under study. Existing molecular beam measurements show dramatic changes, for instance, in the initial sticking probability or sticking coefficient S_0 for N_2 molecules at two different tungsten faces, W(100) and W(110). At relatively low surface temperature and thermal energies of the beam, the sticking coefficient is roughly $S_0 \approx 1$ on W(100) [23–25]. However, the dissociation probability is decreased by two orders of magnitude on W(110) for the same range of surface temperature and kinetic energies [26, 27]. The variation in the reactivity between the two tungsten faces is due to the appearance of dynamical effects at distances relatively far from the surface and not due to specific features of the surface active sites in which the atoms are eventually adsorbed after dissociation [28–30]. Iron surfaces are also reported to undergo tremendous variations in the chemical activity when going from one crystal face to another. Under low pressures, the maximum value of the nitrogen molecule dissociation probability is obtained at the most open iron face, Fe(111). A less reactive face is the Fe(100), while the lowest reactivity was observed for the close-packed Fe(110) surface [31]. Although Fe(111) is the most reactive iron face, the observed dissociation probability is still extremely low $S_0 \approx 10^{-6}$ at incident energies of $E_i \approx 0.1$ eV. The sticking is increased by five orders of magnitude and approaches a saturation

value of $S_0 \approx 10^{-1}$ when the initial kinetic energy is increased up to $E_i \approx 4.3$ eV [32, 33].

1.4 Experimental Techniques

Experiments used for the study of surface properties as well as for the study of the catalytic action often require to be performed under ultrahigh vacuum conditions [34]. Molecular beam experiments are considered as a standard technique for the investigation of the dynamics of elementary reactions at surfaces at the molecular level. However, there are plenty of other techniques that can be used for the molecular-level surface characterization. Let us mention, for instance, X-ray photoelectron spectroscopy (XPS), low energy electron diffraction (LEED), and medium-energy ion scattering (MEIS), which are instrumental to measure the surface structure and the surface chemical composition. Other widely used techniques are: high resolution electron energy loss spectroscopy (HREELS), Auger electron spectroscopy (AES), and thermal desorption spectroscopy (TDS). The outcome of all these techniques can be indirectly used to estimate or evaluate the rates of some elementary reactive processes at surfaces. Some of the experimental data used for the comparison with our theoretical results in this thesis are obtained from these techniques.

1.5 Molecular Dynamics Simulations

The theoretical description of surface chemical reactions is one of the central topics of surface science. Beside its importance in providing accurate insight into experimental results, it may also help to reduce the number of trials in experiments. One of the major advantages is the prediction of new trends and processes. In surface science, atomic-level studies are often based on well defined single crystal surfaces that make it simpler to analyze and understand the elementary reactive processes arising on them [19]. Industrial catalysts, however, usually have large surface areas and thus the single crystal is a very rough model for their description. Recently, some calculations have tried to describe the catalytic action under high temperature and pressure [35], making the surface science theoretical studies more realistic for the conditions in which the

1. INTRODUCTION

industrial catalysts function.

When there is a large mass mismatch between the gas-phase molecules and the surface atoms, the Born-Oppenheimer static surface (BOSS) approximation has been widely used to describe the molecule-surface interactions. Within the BOSS approximation, electronic structure calculations are performed to draw the system energy landscape. This can be considered as the first step in adiabatic calculations. Density functional theory has become a common choice for the calculations of the equilibrium structures, adsorption energies, reaction paths, and activation barriers for different processes on metal surfaces. It is important to mention that these methods provide an accurate quantitative description of these properties for many systems.

Coupled with the electronic structure calculations, interpolation methods have been applied to build continuous representations of potential energy surfaces accounting for the different degrees of freedom of the system under study. Based on these global energy maps, molecular dynamics simulations can be launched to analyze the dynamics of different processes. A useful approximation for this is to remain at the level of classical dynamics in which classical trajectory calculations are performed by the integration of the classical equations of motion. By averaging over all possible initial conditions, statistical information about the individual reactions probabilities can be obtained. For the purpose of describing the macroscopic processes that take place in a real reactor, more global statistical theories have to be used, which usually include the different reaction rates as input information.

1.6 Purpose and Structure of this Work

The main purpose of my thesis is a theoretical study of the interaction of nitrogen with a clean Fe(111) surface. Electronic structure calculations for the surface geometry and relaxation, as well as calculations for the interaction of nitrogen atoms and molecules with the static Fe(111) surface have been performed.

A detailed study of the Fe bulk properties and the atomic multilayer relaxations will be the starting point of our work. After the minimum energy structure arrangement of the low-index Fe(111) surface is obtained, we will use first-principles calculations to describe the interaction of N and N₂ with the Fe(111) surface. The most difficult part of this task

is to codify into a single function, namely, the potential energy surface (PES), the full energy landscape of the system. Finally, we perform classical trajectory calculations in order to study the dissociative and non-dissociative adsorption mechanisms of N_2 on the Fe(111) surface. The final analysis of these calculations will allow us to understand the dynamics of the different reaction channels of nitrogen on Fe(111), the most reactive iron face.

A complementary point of this work is the study of the isotope substitutions of hydrogen in the Eley-Rideal recombination mechanisms on the H(D,T) pre-covered tungsten surfaces W(110) and W(100). The recombination of atoms with other atoms already adsorbed at the surface is another physico-chemical process of great interest. The theoretical description is in this case more involved due to the large surface areas required to properly describe the dynamics. We think that it is relevant to include the study in this thesis in order to give an example of other elementary reactive processes that may occur at metal surfaces.

The thesis manuscript is structured as follows:

- **Chapter 2:** We describe the theoretical methods used to perform first-principles calculations.
- **Chapter 3:** We describe the interpolation methods used to build potential energy surfaces (PESs), as well as the dynamical methods used to perform classical trajectory calculations.
- **Chapter 4:** This is the first chapter of our results, which includes the investigation of the Fe(111) surface structure properties. It also defines the minimum energy structure for the surface slabs later used for our calculations of the interaction with nitrogen atoms and molecules.
- **Chapter 5:** This chapter includes the construction of the PESs for N and N_2 on the Fe(111) surface, as well as a description of the PESs properties.
- **Chapter 6:** Based on the pre-constructed 6D-PES, we present our results for the molecular adsorption dynamics of N_2 on a clean Fe(111) surface.
- **Chapter 7:** The dissociative adsorption dynamics of N_2 on Fe(111) is introduced, together with the comparison between the chemical reactivity of N_2 on Fe(111) and Fe(110) surfaces.

1. INTRODUCTION

- **Chapter 8:** Study of the isotope effects in Eley-Rideal abstraction dynamics for hydrogen on W(100) and W(110) surfaces, precovered with hydrogen and its isotopes.
- **Chapter 9:** The conclusions and highlights of this thesis work are summarized.

2

Density Functional Theory

The simulation of gas-solid interfaces has become an important field of research during the last decades. The immense progress achieved is due to advances in computer science and to the development of efficient algorithms for electronic structure calculations. The theoretical descriptions using first-principles methods provide a microscopic insight into the properties of atoms and molecules in their interaction with solids, which is complementary to the experimental investigations. Indeed, the development of theoretical surface science and computational chemistry opens the door for a large collaboration between theory and experiment. Thus, experimental findings can be explained in further detail from the theoretical field, or the theoretical predictions can be verified experimentally.

The last two decades show that density functional theory (DFT) is one of the most widely used methods for the electronic structure calculations in surface science. In this chapter, we present an introduction to the standard time-independent DFT, as well as the practical implementation of the theory by Kohn and Sham. First, Sec. 2.1 illustrates the complexity of the many-body problem. A major approximation of the many-body problem will be introduced under the name of Born-Oppenheimer approximation in Sec. 2.2. Then, Sec. 2.3 contains a brief history and the derivation of DFT. The exchange-correlation functionals, as described in the Jacob's ladder scheme, will be the topic of Sec. 2.4. Implementation of DFT will be the topic of Sec. 2.5.

2. DENSITY FUNCTIONAL THEORY

2.1 The Many-Body Problem

In quantum-mechanics, the many-body Schrödinger equation is an eigenvalue equation that, in stationary and non-relativistic terms, is written as

$$\hat{H} |\Psi\rangle = E |\Psi\rangle, \quad (2.1)$$

where \hat{H} is the Hamiltonian operator, $|\Psi\rangle$ is an eigenstate of the system and E is the eigenvalue corresponding to this eigenstate. In solid state physics and chemistry, the relevant Hamiltonian has to include both the nuclei and the electrons. The only fundamental interaction between them that has to be considered is the electrostatic interaction. If only the valence electrons are considered, relativistic effects are usually neglected [36]. Consequently, the Hamiltonian operator that determines the total energy of the system can be split into two terms: the electronic term and the nuclei term,

$$\hat{H}_{eN} = \underbrace{\hat{T}_{el} + \hat{V}_{el-el} + \hat{V}_{el-nucl}}_{\hat{H}_e} + \underbrace{\hat{T}_{nucl} + \hat{V}_{nucl-nucl}}_{\hat{H}_N}. \quad (2.2)$$

T_{el} and T_{nucl} are the kinetic energy operators of electrons and nuclei, respectively. The other terms represent the electrostatic interaction among the electrons and the nuclei. Let us consider a system consisting of N nuclei and n electrons, with nuclear mass M and electronic mass m . Let us call the nuclei coordinates (R_I, \dots, R_N) and the electron coordinates (r_i, \dots, r_n) , as shown in Fig. 2.1. In atomic units (i.e., $m_e = \hbar = e = 1$), the individual terms in Eq. 2.2, in the coordinates representation, are given by

$$\text{Kinetic energy of electrons} \quad T_{el} = -\frac{1}{2} \sum_{i=1}^n \vec{\nabla}_i^2, \quad (2.3)$$

$$\text{Electron-electron interaction} \quad V_{el-el} = \sum_{i \neq j}^n \frac{1}{|\vec{r}_i - \vec{r}_j|}, \quad (2.4)$$

$$\text{Electron-nuclei interaction} \quad V_{el-nucl} = -\sum_{i=1}^n \sum_{I=1}^N \frac{Z_I}{|\vec{r}_i - \vec{R}_I|}, \quad (2.5)$$

$$\text{Kinetic energy of nuclei} \quad T_{nucl} = -\frac{1}{2} \sum_{I=1}^N \frac{1}{M} \vec{\nabla}_I^2, \quad (2.6)$$

$$\text{Nuclei-nuclei interaction} \quad V_{nucl-nucl} = \sum_{I \neq J}^N \frac{Z_I Z_J}{|\vec{R}_I - \vec{R}_J|}. \quad (2.7)$$

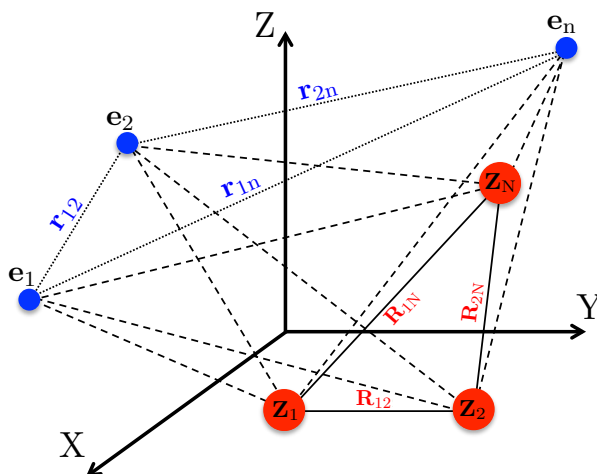


Figure 2.1: Representation of the molecular system in cartesian coordinates. Blue colour represents electrons and red colour denotes the nuclei. Dotted, dashed and solid lines illustrate interactions between electron-electron, electron-nuclei and nuclei-nuclei, respectively.

The whole physical information is contained in the Hamiltonian (Eq. 2.2), except for the symmetry of the wave function. Nevertheless, the Hamiltonian in Eq. 2.2 is too complex to be exactly solved in most cases, due to the dependence of the wave function Ψ on a large number of variables. For a system containing N nuclei and n electrons, there are $3N + 4n$ degrees of freedom, arising from $3N$ spatial coordinates of the nuclei $\{\vec{R}\}$, $3n$ spatial coordinates of the electron $\{\vec{r}\}$, and in addition the spin coordinates $\{\sigma_i\}$ of the electrons. Due to the complexity of the wave function, Eq. 2.1 is practically insoluble, except in the case of the Hydrogen atom, in which an exact solution can be derived. Thus, the challenge in physics and chemistry is to look for approximate solutions, within a reasonable accuracy, for the time-independent many-body Schrödinger equation, in order to determine the static properties of a non-relativistic quantum system, using the Hamiltonian of Eq. 2.2. The first simplification of the problem is the Born-Oppenheimer Approximation that will be described in the next section.

2.2 Born-Oppenheimer Approximation

The first approximation in the way of solving the many-body Schrödinger equation, which is actually a common one in quantum chemistry, is the so-called Born-Oppenheimer or adiabatic approximation [37]. The main idea of such an approximation is the separation of the electronic and nuclear motion. It is based on the fact that the nuclear mass is $\approx 10^4$ to 10^5 larger than the mass of the electron. Then, the speed of the electrons is $\approx 10^2$ to 10^3 faster than the speed of the nuclei at the same kinetic energy. The electrons response to an external perturbation will be much faster than the nuclei response. We can assume that the electron will follow the motion of the nuclei instantaneously. Hence, we can consider that the electrons stay in their ground state irrespectively of the nuclei configuration. At the same time, the nuclei move in a potential created by the electron distribution. In practice, the nuclear kinetic energy term T_{nucl} in Eq. 2.2 is set to be zero and the electronic Hamiltonian H_{el} for fixed nuclear positions $\{\vec{R}\}$ is then given by:

$$H_{el} \{\vec{R}\} = T_{el} + V_{el-el} + V_{el-nucl} + V_{nucl-nucl}, \quad (2.8)$$

in which the nuclei coordinates, $\{\vec{R}\}$, serve as a parameter and not as a variable. In addition, $V_{nucl-nucl}$ is inserted to the Hamiltonian as a constant. One can write the total wave function Ψ as a product of two functions such that:

$$\Psi(\vec{r}, \{\vec{R}\}) = \psi(\vec{r}, \{\vec{R}\}) \phi(\vec{R}), \quad (2.9)$$

where the first term $\psi(\vec{r}, \{\vec{R}\})$ represents the wave function of the electronic motion at fixed nuclei position $\{\vec{R}\}$, with explicit dependence on the electronic position \vec{r} , and again the nuclei coordinates $\{\vec{R}\}$ are not variables but parameters. $\phi(\vec{R})$ describes the static nuclei wave function. Thus, the Schrödinger equation for electrons at fixed nuclei position is

$$H_{el} (\{\vec{R}\}) \psi(\vec{r}, \{\vec{R}\}) = E_{el} (\{\vec{R}\}) \psi(\vec{r}, \{\vec{R}\}). \quad (2.10)$$

In Eq. 2.10, the eigenenergy $E_{el} \{\vec{R}\}$ describes the electronic energy for a fixed position of the nuclei. Therefore, we can identify $E_{el} \{\vec{R}\}$ as the Born-Oppenheimer or adiabatic potential energy for the nuclear motion. The nuclei can be then assumed to move in the Born-Oppenheimer potential energy according to the nuclear Schrödinger equation

$$\{T_{nucl} + E_{el} (\vec{R})\} \phi(\vec{R}) = E_{nucl} \phi(\vec{R}). \quad (2.11)$$

2.2 Born-Oppenheimer Approximation

Often, the Born-Oppenheimer approximation assumes that the nuclei can be treated as classical particles, for which the quantum effects are neglected. If so, the atomic motion can be solved by applying the classical equation:

$$M_I \frac{\partial^2}{\partial t^2} \vec{R}_I = -\frac{\partial^2}{\partial \vec{R}_I^2} E_{el} (\{\vec{R}\}). \quad (2.12)$$

Furthermore, the forces acting on one nucleus at a given position R can be evaluated using the Hellmann-Feynman theorem [38, 39]

$$F_I = -\frac{\partial^2}{\partial \vec{R}_I^2} E_{el} (\{\vec{R}\}) = \langle \psi(\vec{r}, \{\vec{R}\}) | \frac{\partial^2}{\partial \vec{R}_I^2} H_{el} (\{\vec{R}\}) | \psi(\vec{r}, \{\vec{R}\}) \rangle. \quad (2.13)$$

The Born-Oppenheimer approximation is based on the small value of the ratio $m_e/M \ll 1$, which is crucial for its validity. In fact, the Born-Oppenheimer approximation neglects the electronic transitions due to the motion of the nuclei. One may think about the accuracy of such an approximation in surface science. On one hand, for semiconductor materials as well as insulators, in which there is a band gap, the adiabatic approximation should not pose major problems. On the other hand, at metals in which no band gap exists, small excitation energies are available and it would be easier to break down the Born-Oppenheimer approximation.

Within the Born-Oppenheimer approximation, the original Schrödinger equation 2.1 is simplified, but further approximations have to be introduced yet for solving the electronic part in Eq. 2.8. In principle, in the quest for the ground state total energy, there are two fundamental electronic structure methods:

1. The wave function based methods, in which the many-body problem is transferred into a single particle problem and the Slater determinant is used to ensure the antisymmetry of the electronic wave function $\psi(\vec{r}, \{\vec{R}\})$. Electron correlation can be added through several methodologies. Nevertheless, the use of these methods is limited to few number of atoms and molecules. Hartree-Fock theory is one of the most popular methods based on the approximation of the wave function, but unfortunately becomes too demanding as the number of electrons in the system increases.
2. The electronic density based methods, which rely on the density of electrons instead of the electronic wave functions to describe the quantum mechanical system.

2. DENSITY FUNCTIONAL THEORY

Density functional theory (DFT) is by far the most widely used in condensed matter physics during the last fifty years. We will have a close look to DFT in the next sections.

2.3 Density Functional Theory

The central idea of DFT is that one can replace the dimensionality dependence on $3N$ variables, which appears in the wave function based methods, into only 3 variables, thanks to the electronic density. The story of DFT started almost one century ago. In 1927, the British physicist Llewellyn Thomas shared his ideas with the Italian physicist Enrico Fermi to create the Thomas-Fermi model. This is considered to be the first try to calculate the electronic structure of atoms by introducing an approximation method based on the ground state density. Many years after this, in Paris in 1964, the French-American physicist Pierre Hohenberg was a postdoctoral researcher working with the American theoretical physicist Walter Kohn when they proved that there is an exact method that can be used to calculate the electronic structure properties of different systems based on the electronic charge density. One year later, in 1965, Walter Kohn and the Chinese physicist Lu Sham derived the self-consistent equations that must be solved for a set of orbitals whose density is defined to be exactly that of the real system. The Kohn-Sham formalism is the most standard practical application of DFT theory [40].

Due to its low computational cost and relatively high accuracy, DFT has become a standard theoretical technique in many branches of physics, chemistry, and materials science. The coupling of DFT with the revolution in computing hardware and software during the last decades, made it possible to perform systematic comparisons of theoretical results with experiments over a wide range of materials, and set up first-principles predictions of new materials. In principle, the prediction of new catalysts is one of the notable successes of DFT, which is our main interest in this thesis. In 1998, the development of DFT opened the door for Walter Kohn to share the Nobel Prize in Chemistry with John Pople, the latter recognized for his work on developing computational methods in quantum chemistry.

In this section, we will present the basic ideas about the standard time-independent

density functional theory. The first attempts to use the electronic charge density, introduced in the Thomas-Fermi model, will be our starting point. After this, we will discuss the Hohenberg-Kohn theorems. We will finish with a general introduction of the Kohn-Sham self-consistent equations.

2.3.1 Thomas-Fermi Model

The statistical theory of atomic electrons was first proposed by Thomas [41] and Fermi [42] in 1927 and was originally introduced in order to study the electron energy and the charge density for atoms or molecules with a large number N of electrons. The idea behind Thomas-Fermi is to replace the complicated 3- N wave function $\psi(\vec{r}_1, \vec{r}_2, \dots, \vec{r}_N)$ and the associated Schrödinger equation by the simpler electron density $n(\vec{r})$ and its associated calculations [43]. In this model, the kinetic energy of electrons is derived from quantum statistical theory based on the uniform electron gas, while the electrostatic potential representing the electron-electron and the electron-nucleus interaction is treated classically. The total energy of the system is a functional of the ground state charge density $n(\vec{r})$ and can be expressed as

$$\begin{aligned}
 E_{TF}[n(\vec{r})] &= \frac{3}{10} (3\pi^2)^{2/3} \int n(\vec{r})^{5/3} d\vec{r} \\
 &\quad - Z \int \frac{n(\vec{r})}{r} d\vec{r} + \frac{1}{2} \int \int \frac{n(\vec{r}_1) n(\vec{r}_2)}{|\vec{r}_1 - \vec{r}_2|} d\vec{r}_1 d\vec{r}_2,
 \end{aligned}
 \tag{2.14}$$

where the first term is roughly the minimum quantum mechanical kinetic energy of noninteracting N -electrons needed to produce an electron density $n(\vec{r})$. The second and third terms in Eq. 2.14 represent the electron-nucleus and electron-electron interactions, respectively. As we mentioned above, the electrostatic interactions are treated classically and introduced as an external potential.

The advantages of the Thomas-Fermi model are its simplicity and clarity over a wide range of densities and temperatures. However, this model is not particularly efficient because the ground state energy can be determined only by using the electronic density. The model is only valid for systems with a constant external potential. Indeed, clear connection between the electronic density and the electronic wave function is still missing. This connection is provided in the Hohenberg-Kohn and Kohn-Sham theoretical framework, as we will see next.

2. DENSITY FUNCTIONAL THEORY

2.3.2 Hohenberg-Kohn Theorems

In 1964, Hohenberg and Kohn [44] formulated the theorems that provided the basis of density functional theory. Their approach allows us to express the electronic Hamiltonian as a functional of the ground state electronic density.

Hohenberg-Kohn (HK) first theorem states that: For any system of interacting particles under the influence of an external potential, the external potential is uniquely determined by the non-degenerate ground state density $n_0(\vec{r})$. The proof of this theorem proceeds through two steps. First, we need to be sure that two different external potentials will not produce the same ground state density. Second, two ground state densities can not be produced by the same ground state wave function. Let us assume that there is a number of electrons enclosed inside a box and let us take two external potentials, $v_1(\vec{r})$ and $v_2(\vec{r})$, that differ by more than a constant (i.e., $v_1(\vec{r}) \neq v_2(\vec{r}) + \text{constant}$). Let us assume, nevertheless, that the two potentials give the same electron ground state density $n(\vec{r})$. Now, if there are two different Hamiltonians H_1 and H_2 , even if they give the same ground state density $n(\vec{r})$, their normalized wave functions ψ_1 and ψ_2 respectively have to be different. Since the ground state energy is non-degenerate, one can apply the Rayleigh-Ritz variational principle on the trial wave function ψ_1 with the Hamiltonian H_1 and then the ground state energy E_1 would satisfy that:

$$\begin{aligned} E_1 < \langle \psi_1 | H_1 | \psi_1 \rangle &= \langle \psi_1 | H_2 | \psi_1 \rangle + \langle \psi_1 | H_1 - H_2 | \psi_1 \rangle \\ &= E_2 + \int n_0(\vec{r}) [v_1(\vec{r}) - v_2(\vec{r})] d^3\vec{r}. \end{aligned} \quad (2.15)$$

In Eq. 2.15, H_1 and H_2 differ only by their external potentials v_1 and v_2 , respectively. Similarly, the non-degenerate ground state energy E_2 would satisfy:

$$\begin{aligned} E_2 < \langle \psi_2 | H_2 | \psi_2 \rangle &= \langle \psi_2 | H_1 | \psi_2 \rangle + \langle \psi_2 | H_2 - H_1 | \psi_2 \rangle \\ &= E_1 + \int n_0(\vec{r}) [v_2(\vec{r}) - v_1(\vec{r})] d^3\vec{r}. \end{aligned} \quad (2.16)$$

Then, by adding Eq. 2.15 and Eq. 2.16, we obtain

$$E_1 + E_2 < E_2 + E_1. \quad (2.17)$$

Equation 2.17 obviously shows a contradiction. Hence, we can conclude that there cannot be two different external potentials (v_1, v_2) that give the same ground state density $n_0(\vec{r})$. Indeed, the ground state density uniquely determines the external potential

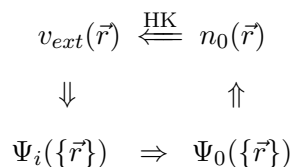


Figure 2.2: Schematic representation of Hohenberg-Kohn Theorem. The smaller arrows denote the usual solution of the Schrödinger equation, while the long arrow labeled ‘HK’ denotes the Hohenberg-Kohn theorem, which completes the circle. The potential $V_{ext}(\vec{r})$ determines all states of the $\Psi_i(\{\vec{r}\})$, including the ground state $\Psi_0(\{\vec{r}\})$ and ground state energy $n_0(\vec{r})$

$V_{ext}(\vec{r})$ within a constant and all ground state properties, including the electronic wave function $\psi(\vec{r})$.

The second Hohenberg-Kohn theorem says that the ground state energy is a functional of the electronic density that reaches its minimum value for the exact electronic density of the system:

$$\begin{aligned}
 E_v[n(\vec{r})] &= T_e[n(\vec{r})] + V_{ee}[n(\vec{r})] + V_{ext}[n(\vec{r})] \\
 &= \int n(\vec{r}) V_{ext}(\vec{r}) dr + F_{HK}[n(\vec{r})],
 \end{aligned} \tag{2.18}$$

where F_{HK} is the Hohenberg-Kohn functional, that depends only on $n(\vec{r})$. It is in principle universal as it does not depend on any external potential $V_{ext}(\vec{r})$,

$$F_{HK}[n(\vec{r})] = T_e[n(\vec{r})] + V_{ee}[n(\vec{r})]. \tag{2.19}$$

Since, the electronic density is related to the number of electrons as

$$N = \int n(\vec{r}) d^3\vec{r}, \tag{2.20}$$

and the potential $V_{ext}(\vec{r})$ is external, it follows that $n(\vec{r})$ determines the full system Hamiltonian. Hohenberg and Kohn proved, by applying the variational principle to this energy functional, that the electronic density that minimizes the energy is the exact ground state density [36].

Although the Hohenberg-Kohn theorems are extremely powerful, they do not offer a way of computing the ground-state density of a system in practice. The appearance of Kohn-Sham article in 1965 opened a straightforward door to perform calculations based on the density functional theory proposed by Hohenberg and Kohn.

2. DENSITY FUNCTIONAL THEORY

2.3.3 Kohn-Sham Formalism

One year after the article of Hohenberg and Kohn [44], in 1965, Kohn and Sham published an article [45] that transformed DFT into a way to perform electronic structure calculations. They suggested that, instead of finding the correct ground state density $n(\vec{r})$ of the full-interacting system, one can use the picture of non-interacting particles moving in an effective potential to calculate the same density $n(\vec{r})$. The Kohn-Sham (KS) method is based on solving a set of Schrödinger-like equations, in which each equation involves only one single electron. If $\psi_i(\vec{r})$ are the one-electron wave functions, then the total electron density is obtained by summing over N electron states,

$$n(\vec{r}) = \sum_{i=1}^N |\psi_i(\vec{r})|^2. \quad (2.21)$$

The expression of the so-called KS equations is then given as:

$$\left[-\frac{\hbar}{2m} \vec{\nabla}^2 + v_{eff}(\vec{r})\right] \psi_i(\vec{r}) = \varepsilon_i \psi_i(\vec{r}). \quad (2.22)$$

The solution of Eq. 2.22 is a single electron wave function, which depends only on three spatial variables, $\psi_i(\vec{r})$. In Eq. 2.22, $v_{eff}(\vec{r})$ is the effective potential in which the electron is moving, namely:

$$v_{eff}(\vec{r}) = v_{ext}(\vec{r}) + v_H(\vec{r}) + v_{xc}(\vec{r}), \quad (2.23)$$

where v_{ext} is the external potential. When describing condensed matter, this is typically the potential that represents the interaction between one electron and the collection of atomic nuclei. The potential v_H is the so-called Hartree potential, which is defined as:

$$v_H(\vec{r}) = \int \frac{n(\vec{r}')}{|\vec{r} - \vec{r}'|} d^3\vec{r}'. \quad (2.24)$$

The Hartree potential v_H , represents the Coulomb potential between the electron and the electron density involved in the problem. The potential v_{xc} that appears as the third term in Eq. 2.23 defines the exchange and correlation contributions to the single electron equations. The exchange-correlation potential is the functional derivative of the exchange-correlation energy functional $E_{xc}[n(\vec{r})]$.

$$v_{xc} = \frac{\delta E_{xc}[n(\vec{r})]}{\delta n(\vec{r})} \quad (2.25)$$

The procedure to solve the KS equations looks like circular. In order to solve the KS equations, we need to define the Hartree potential, which depends on the electronic density, as shown in Eq. 2.24. To find the electronic density, we need to define the electron wave functions, which are the solutions of the KS equations. To break this circle, KS equations are solved in a self-consistent way. One can start with an initial guess of the electron density, $n(\vec{r})$. Then, the effective potential, v_{eff} , can be extracted from Eq. 2.23, and the KS equations can be solved in Eq. 2.22. Based on the KS solutions, $\psi_i(\vec{r})$, we obtain from Eq. 2.21 a new electronic density, $n_{KS}(\vec{r})$. If the new density is equal to the trial one (i.e., $n_{KS}(\vec{r}) = n(\vec{r})$), then, $n_{KS}(\vec{r})$ is the ground state density. Consequently, it can be used to calculate the minimum energy of the system. In case that the two densities are different, then the trial energy has to be updated and the process is started anew by using the last KS electron density as the trial density. This process is repeated iteratively until equality between the trial density and the KS density is achieved. A schematic representation of the search for a self-consistent solution of the Kohn-Sham equations is illustrated by a flow-chart in Fig. 2.3.

In principle, the results of the Kohn-Sham procedure, as illustrated above, will be the exact ground state density and energy. Unfortunately, the exact form of the exchange-correlation energy functional $E_{xc}[n(\vec{r})]$ is unknown. Again, the difficulty of the many-body problem is confronted. Looking for good approximations for the term $E_{xc}[n(\vec{r})]$ is one of the challenges of modern work on density functional theory. In the next section we will present some ideas that are used in the generation of some approximations for the exchange-correlation term in the KS formalism.

2.4 Exchange-Correlation Functionals

The proposals of Hohenberg, Kohn, and Sham are in principle an exact alternative to the Schrödinger equation to find the exact ground state energy. However, the key point is that an exact definition of the energy exchange-correlation functional, $E_{xc}[n(\vec{r})]$, should exist, and this is not the case. Fortunately, there is one case where this functional can be derived exactly, which is the uniform electron gas. In the uniform electron gas, the electron density is constant at all points in space. Actually, this is not the case in real materials, where the variations in electron density define the chemical bonds and

2. DENSITY FUNCTIONAL THEORY

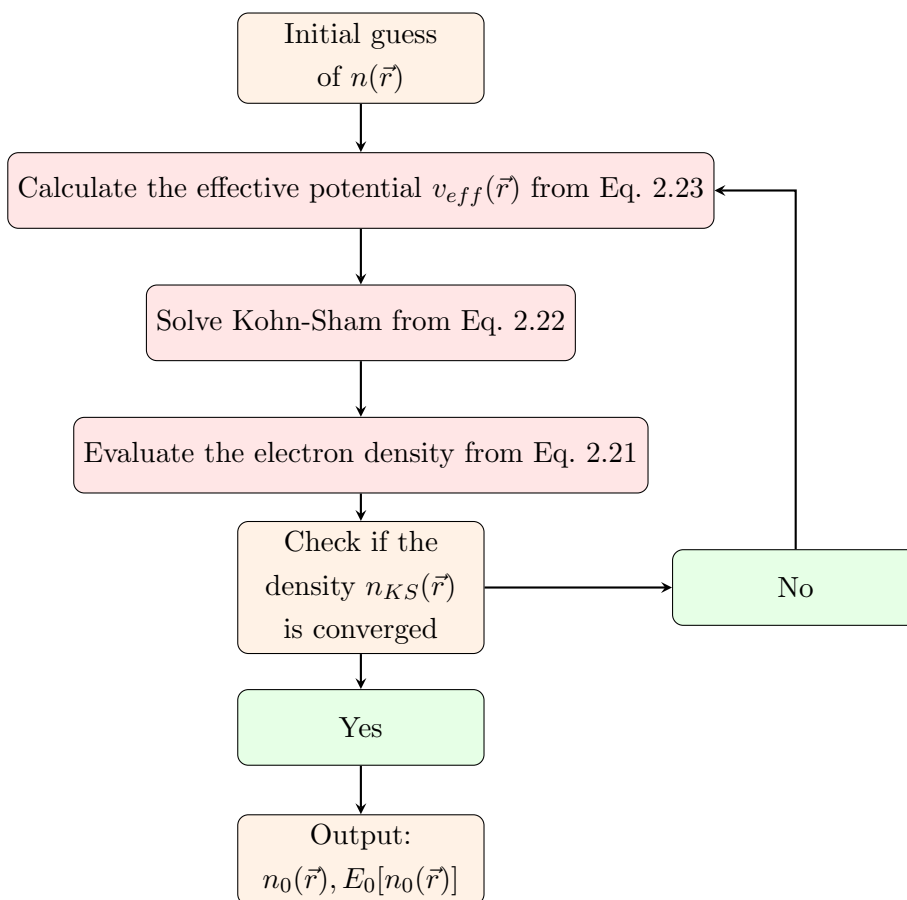


Figure 2.3: Flow-chart diagram of the self-consistent scheme to solve the one-particle Kohn-Sham equation.

this is what makes the materials interesting. Nevertheless, the uniform electron gas is an invaluable tool to develop new knowledge on electron exchange and correlation.

The search for functionals that can reproduce exchange and correlation over inhomogeneous electron densities is one of the most interesting areas of condensed matter physics and quantum chemistry. In the following, we will briefly describe the main approximations currently in use. According to Jacob's ladder [46], there are four main generations of exchange-correlation functionals. Climbing stairs toward chemical accuracy we will pass by the so-called LDA, GGA, meta-GGA and hybrid functionals. This will be discussed in more detail in the following.

2.4.1 Local Density Approximation

The local density approximation (LDA) is considered to be the simplest approximation to the exchange-correlation energy functional, $E_{xc}[n(\vec{r})]$. It was introduced in the original article of Kohn and Sham [44] to provide a solution for Kohn-Sham equations. In LDA, we set the exchange-correlation energy per electron at each point in space as the known exchange-correlation energy in a homogeneous electron gas of the same density,

$$\varepsilon_{xc}[n(\vec{r})] = \varepsilon_{xc}^{hom}[n(\vec{r})], \quad (2.26)$$

and the analytical expression of the total exchange-correlation energy is written as

$$E_{xc}^{LDA}[n(\vec{r})] = \int \varepsilon_{xc}^{hom}[n(\vec{r})] n(\vec{r}) d^3\vec{r}, \quad (2.27)$$

where $\varepsilon_{xc}^{hom}[n(\vec{r})]$ is the homogeneous exchange-correlation energy per particle for a given electronic density.

In practice, the exchange and correlation terms are calculated separately [47]. A customary expression for the exchange term is given by the Dirac exchange-energy functional [48]:

$$\varepsilon_x^{hom}[n(\vec{r})] = -\frac{3}{4} \left(\frac{3n(\vec{r})}{\pi} \right)^{1/3}. \quad (2.28)$$

The sphere radius in which an electron can exactly be found in the homogeneous electron gas density n , is called the Wigner-Seitz radius r_s , that is related to the density as $r_s = \left(\frac{3}{4\pi n} \right)^{1/3}$. The exact expression of the correlation term is also unknown. However, approximate expressions can be proposed based on properties of the homogeneous

2. DENSITY FUNCTIONAL THEORY

electron gas.

The local density approximation, LDA, provides a full definition of the Kohn-Sham equations but the results do not give the exact solution of the Schrödinger equation because the exchange-correlation functional does not correspond to the case of real materials. In addition, LDA ignores the inhomogeneities in electron density due to the nearby electrons. One can assume that the LDA is more accurate for a slowly varying density. For other cases, we may need to take into account not only the local value of the electron density, but also its gradients. This is the generalized gradient approximation.

2.4.2 Generalized Gradient Approximation

The generalized gradient approximation (GGA) is a correction of the LDA, in which the electron density gradient, $\vec{\nabla}n(\vec{r})$, is taken into account in addition to the local density $n(\vec{r})$. The exchange-correlation energy functional is given by

$$E_{xc}^{GGA}[n(\vec{r})] = \int \varepsilon_{xc}^{hom} [n(\vec{r}), |\vec{\nabla}n(\vec{r})|] n(\vec{r}) d^3\vec{r}. \quad (2.29)$$

Including the electron density gradient in GGA functional forms is a very common option in the field of electronic structure calculations. In some of them, the accuracy of the results from GGA calculations approaches the accuracy of traditional quantum chemistry methods [49].

The first reasonable attempt to construct a functional satisfying GGA's properties was made by Perdew and Wang in 1991. They provided the well known functional PW91 [50]. PW91 opened the door for a more accurate application of DFT over a wide range of materials. Based on the PW91 functional, Perdew, Burke, and Ernzerhof introduced a common and widely used GGA functional [51], namely the PBE functional. There are some modified versions or extensions of the PBE functional that are also used in electronic structure calculations. Zhang and Yang introduced a slight revision on the PBE functional and called their functional revPBE [52]. Later on, in 1999, in Nørskov's group, a new functional with the name, RPBE was proposed [53]. The most recent PBE functional appeared in 2008 under the name PBEsol [54].

GGA functionals include more physical ingredients than LDA functionals. Therefore, GGA should describe the electronic system with higher accuracy as compared with

LDA functionals. This assumption is quite often true, but there are some cases however for which LDA functionals give better results than GGA ones. Let us also remark that, among the most popular GGA functionals, the PBE functional is just a modified version of PW91.

In Eq. 2.27 the LDA functional is a local functional of the electron density. Similarly, in Eq. 2.29, the GGA functional is a semi-local functional of the electron density. LDA and GGA often use some empirical parameters from computer and real experiments to fit the exchange and correlation parts of the energy. Beyond LDA and GGA, there are new generations of functionals treating the exchange and correlation term that take into account the non-locality of the electron density and that use non-empirical parameters. This new generation of exchange-correlation functionals can lead to better accuracy in the description of the electronic system. We only present here some general ideas about them.

2.4.3 Meta Generalized Gradient Approximation

A new form of the exchange-correlation energy functional that goes beyond the GGA is the meta generalized gradient approximation (meta-GGA) [55]. Meta-GGA is a non-empirical exchange-correlation functional, which makes use of the kinetic energy density $\tau(\vec{r})$ in the calculation of the exchange-correlation energy, as an additional term to the electron density $n(\vec{r})$ and the electron density gradient $\vec{\nabla}n(\vec{r})$. The exchange-correlation form of meta-GGA is expressed as:

$$E_{xc}^{meta-GGA}[n(\vec{r})] = \int \varepsilon_{xc}^{hom} [n(\vec{r}), |\vec{\nabla}n(\vec{r})|, \tau(\vec{r})] n(\vec{r}) d^3\vec{r}. \quad (2.30)$$

The kinetic energy density functional, $\tau(\vec{r})$, of the occupied Kohn-Sham orbitals can be expressed as:

$$\tau(\vec{r}) = \sum_i^{occup} |\vec{\nabla}\psi_i(\vec{r})|^2. \quad (2.31)$$

Meta-GGA functionals are correct up to the fourth order in the electron density gradient expansion for a slowly varying density. Meta-GGA functionals show a semi-local dependence on the electronic wave functions or the Kohn-Sham orbitals. Performing calculations by using meta-GGA functionals is not much more demanding than using the GGA functionals. Calculations including meta-GGA functionals show in general

2. DENSITY FUNCTIONAL THEORY

very good accuracy for a wide variety of properties and systems, although in some cases the meta-GGA functionals result in poor equilibrium bond lengths.

2.4.4 Hybrid Functionals

The exchange-correlation functional is often constructed from a linear combination of the separated exchange and correlation functionals, as we mentioned above. Hybrid functionals are the fourth generation of exchange-correlation energy functionals (E_{xc}), which include partially or totally the exact form of Hartree-Fock (HF) exchange functional,

$$E_x^{HF}[n(\vec{r})] = -\frac{1}{2} \int \int \frac{\psi^*(\vec{r}) \psi(\vec{r}) \psi^*(\vec{r}') \psi(\vec{r}')}{|\vec{r} - \vec{r}'|} d\vec{r} d\vec{r}', \quad (2.32)$$

as well as some exchange and correlation functionals that were used before in the first three generations (i.e., LDA, GGA and meta-GGA), in such a way that:

$$E_{xc}^{hybrid} = E_{xc}^{GGA} + a \left(E_x^{exact} - E_x^{GGA} \right), \quad (2.33)$$

where a is a mixing parameter. The most common functionals that illustrate the hybrid scheme of E_{xc} are B3LYP [56], PBE0 [57], and HSE [58], that differ on the choice of the value of the mixing parameter a , as well as on the exchange-correlation GGA functional used.

We can summarize the exchange-correlation functional methods that we have discussed by making use again of the Jacob's ladder [46] that appears in Fig. 2.4. In Jacob's ladder, the development of methods to improve the exchange-correlation functional is a succession of ladder steps. The highest steps in the ladder lead us to the best possible accuracy for the electronic structure calculations in the DFT frame. However, we should mention that each improvement also requires in general additional computer power. The development of functionals that are even more accurate is one of the most active research areas in quantum chemistry and condensed matter physics.

In the next sections we will show how can we implement DFT in practice in the electronic structure calculations of a periodic system.

2.5 Implementation of Density Functional Theory

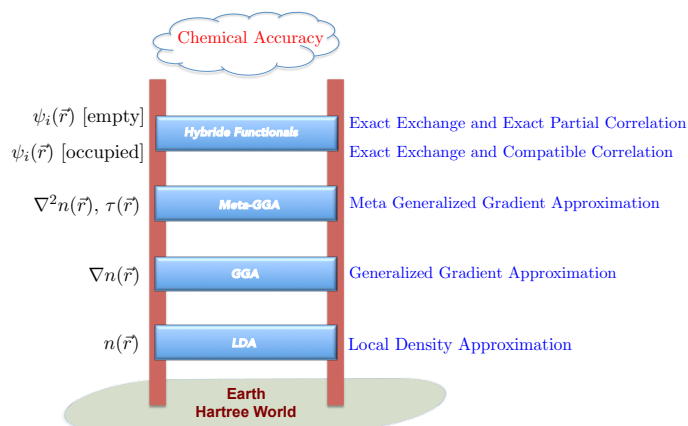


Figure 2.4: Jacob's ladder for exchange-correlation functionals [46].

2.5 Implementation of Density Functional Theory

In this section, we will introduce the computational methods that can be used for the solution of Kohn-Sham equations. In this thesis, we are mainly interested in simulations of periodic systems. Therefore, we choose the Vienna Ab initio Simulation Package (VASP), which is a suitable and powerful computational code. In VASP, the wave function is expanded in a plane-waves basis set. Further approximations are also needed to reduce the calculation expenses, still reaching high accuracy. In principle, for the chemical interactions among atoms, the valence electrons can be considered to be the main player, and its role is more important than that of the core electrons. For this reason, pseudopotentials are introduced to reduce the basis-set expansion and, hence, reduce the computational cost. In the following, we will describe in detail the methods that have been used in this thesis to perform DFT calculations.

2.5.1 Plane Waves Basis Set

For practical implementations of DFT, it is quite general to rely on an expansion of the unknown KS wave functions in terms of a set of basis functions, such that

$$\psi_i(\vec{r}) = \sum_{i=1}^m a_i \chi_i(\vec{r}), \quad (2.34)$$

2. DENSITY FUNCTIONAL THEORY

where a_i are the expansion coefficients, $\chi_i(\vec{r})$ is a given basis set, and m is the number of basis functions to be employed. There are many forms of basis sets that can be used for the expansion of the wave function, such as Gaussian, exponential, plane-wave, spline, polynomial, etc. Nevertheless, the choice of the basis functions has to take into account the computational cost as well as the main purpose of the problem. For electronic structure studies, the plane-waves basis set is one of the most common choices for periodic systems.

In solid state simulations, which is the problem of our interest, ions in perfect crystal structures are arranged in a regular periodic way. In this case, we have to deal with an infinite number of electrons moving in the static potential of an infinite number of ions. With this in mind, the electronic wave function has to be calculated for the infinite number of electrons which extend over the whole space and the basis set in which the wave function will be expanded should be in principle infinite. However, because of the periodicity of the solid, we can apply the well known Bloch's theorem to simplify our problem. Bloch's theorem states that any single-particle wave function in a periodic system can be written as the product of a plane-wave and a lattice-periodic part. Then, the wave function will be:

$$\psi_{n,\vec{k}}(\vec{r}) = e^{i\vec{k}\cdot\vec{r}} u_{n,\vec{k}}(\vec{r}),$$

where (2.35)

$$u_{n,\vec{k}}(\vec{r}) = u_{n,\vec{k}}(\vec{r} + \vec{t}).$$

Here, \vec{k} represents the wave vector, n is the band index, and \vec{t} is the lattice translational vector of the simulation cell [47]. Furthermore, $e^{i\vec{k}\cdot\vec{r}}$ refers to the wave-like part, while $u_{n,\vec{k}}(\vec{r})$ is the cell periodic part of the wave function. From Eq. 2.35, we can evaluate the wave function at any point (\vec{r}) in the configuration space. According to the periodic boundary conditions, the periodic function $u_{n,\vec{k}}(\vec{r})$ can be expressed by expanding it in a Fourier series into plane-waves:

$$u_{n,k}(\vec{r}) = \frac{1}{\sqrt{\Omega}} \sum_{\vec{G}} C_{n,\vec{k}+\vec{G}} e^{i\vec{G}\cdot\vec{r}},$$
(2.36)

where \vec{G} is the reciprocal lattice vector of the periodic crystal, and Ω is the volume of the unit cell. Therefore, the electronic wave function is written as a sum of plane-waves as:

$$\psi_{n,k}(\vec{r}) = \frac{1}{\sqrt{\Omega}} \sum_{\vec{G}} C_{n,\vec{k}+\vec{G}} e^{i(\vec{k}+\vec{G})\cdot\vec{r}}.$$
(2.37)

2.5 Implementation of Density Functional Theory

By substitution of Eq. 2.37 into the Kohn-Sham Eq. 2.22, we will have

$$\sum_{\vec{G}} \left[\frac{1}{2} |\vec{k} + \vec{G}|^2 \delta_{\vec{G}\vec{G}'} + v_{eff}(\vec{G} - \vec{G}') \right] C_{n,\vec{k}+\vec{G}} = \varepsilon_{n,\vec{k}} C_{n,\vec{k}+\vec{G}}. \quad (2.38)$$

where, $\delta_{\vec{G}\vec{G}'}$ is the Kronecker δ which reflects that the kinetic energy is diagonal, $v_{eff}(\vec{G} - \vec{G}')$ are the Fourier transforms of the effective potential in real space, and $\varepsilon_{n,\vec{k}}$ are the electronic energies.

For an exact solution of Eq. 2.38, we need an infinite number of plane-waves. Fortunately, the coefficients $C_{n,\vec{k}+\vec{G}}$ for the plane-waves with a small kinetic energy are typically more important than those of large kinetic energy. Thus the plane-wave basis-set can be truncated to include only plane-waves that have kinetic energies less than a particular energy cutoff E_{cut} ,

$$E_{cutoff} \geq \frac{1}{2} |\vec{k} + \vec{G}|^2. \quad (2.39)$$

However, by utilizing a finite basis-set we are actually introducing approximations which may result in less accurate results. But we can overcome this problem by increasing the number of plane-waves that are used in the expansion, i.e., by increasing the cut-off energy.

Up to this point we are handling all electrons included in the system, which is computationally heavy. As we mentioned above, for the chemical bonding, the valence electrons are indeed much more important than the core electrons. We can overcome the heavy computational cost of including all electrons by introducing the pseudopotentials.

2.5.2 Pseudopotential Approximation

Electrons in an atom are classified into valence electrons and core electrons. Valence electrons are the ones playing a role in chemical bonding and chemical reactions. Most interesting physical and chemical properties are determined by the valence electrons. Core electrons, on the other hand, hardly participate in any chemical reaction. Core electrons are strongly bound to the nucleus and largely unperturbed by the surrounding environment, which makes them not essentially involved in chemical bondings. In general, the less important core electrons require more computational cost than the more important valence electrons because the number of the former is usually much larger.

2. DENSITY FUNCTIONAL THEORY

Consequently, we need to search for additional approximations for the simplification of the electronic problem. The use of the pseudopotential approximation [59], which replaces the strong ionic potential with a weaker pseudopotential, will be instrumental in simplifying the problem without losing much accuracy. Generally speaking, the pseudopotential formalism is applied for two main reasons: (i) to reduce the number of plane-waves that are needed to describe the core electrons, and (ii) to eliminate the fast oscillation part in the wave functions of the valence electrons. Figure 2.5 shows that a typical pseudopotential is much weaker than the all-electron potential, and that the pseudo wave function has no radial node inside the core region[47], whereas outside the core radius r_c , it is essential that the pseudo wave function becomes the same as the full wave function.

A common form of the pseudopotential is given by

$$v_{ps}(r) = v_{eff}(r) + \sum_i (\varepsilon_v - \varepsilon_{ci}) |\psi_{ci}\rangle \langle \psi_{ci}|, \quad (2.40)$$

where ε_v and ε_{ci} are one particle valence and core energies, respectively, and ψ_{ci} are the wave functions of the core electrons.

From Eq. 2.40, one notes that the pseudopotential can be a non-local potential because it shows a dependence on the energy and does not operate on a wave function by a multiplication of a r -dependent function. For this reason it is called ‘pseudo-potential’ as it differs from a true potential.

There are two widely used schemes for the introduction of pseudopotentials in electronic structure calculations. The ultra soft pseudopotential (USPP) scheme was proposed by Vanderbilt in 1990 [60]. In this procedure, a very soft kind of pseudopotential was proposed, which enabled dramatic reduction in the necessary size of the basis-set. The second procedure, namely, the projector-augmented wave method (PAW), was proposed by Blöchl in 1994 [61, 62], and is the procedure we are using for the calculations performed in this thesis. It will be presented in the next few lines.

Projector Augmented Wave

The conceptual idea of Blöchl when he proposed the Projector Augmented Wave (PAW) method is that the all-electron valence states ψ_i can be expressed in terms of a smooth

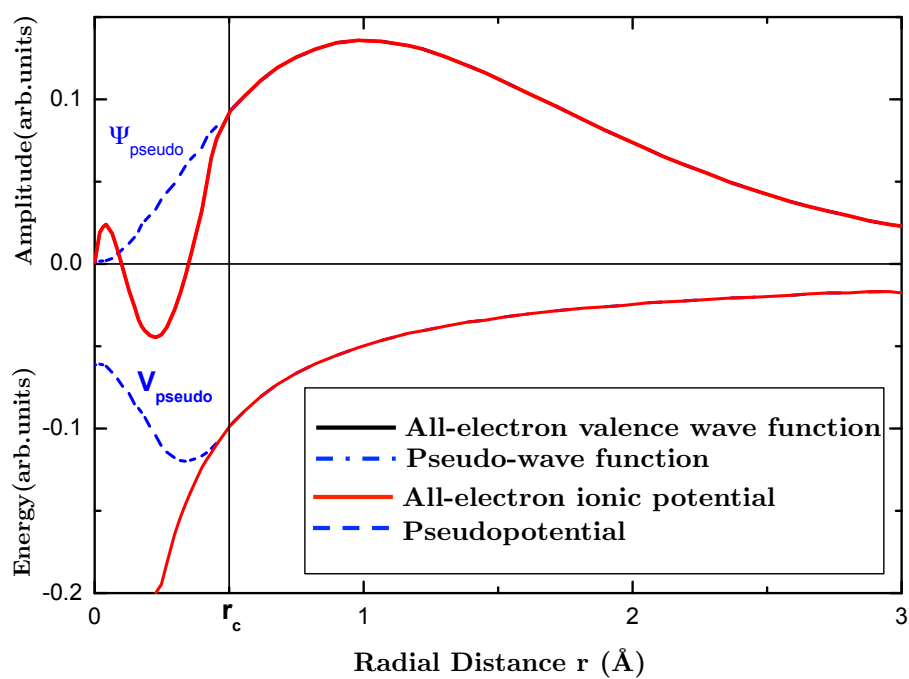


Figure 2.5: Schematic illustration of the difference between the all-electron (red solid line) and the pseudo 3s wave function (blue dashed line) and their corresponding potentials. The core radius r_c is indicated by the vertical line [36].

2. DENSITY FUNCTIONAL THEORY

pseudo wave function, which is augmented by a local basis-set expansion, restricted to a small region around each atom, called the augmentation sphere. The atomic core states are considered to be frozen. The all-electron wave function can be obtained through a linear transformation operator $\hat{\tau}$ as:

$$\psi_i(\vec{r}) = \hat{\tau}\tilde{\psi}_i(\vec{r}), \quad (2.41)$$

such that

$$\hat{\tau} = 1 + \sum_i |\phi_i^{AE}\rangle\langle\tilde{p}_i|\tilde{\psi}_n - \sum_i |\phi_i^{PS}\rangle\langle\tilde{p}_i|\tilde{\psi}_n. \quad (2.42)$$

In Eq. 2.42, the all-electron partial waves are denoted by ϕ_i^{AE} , while the pseudo-partial waves are indicated by ϕ_i^{PS} and both match at the core radius. Also, \tilde{p}_i are the projector functions, which are characteristic for each atom and that are non-zero only inside the augmentation sphere around the atom. The projector function \tilde{p}_i is required to fulfill the orthonormality condition:

$$\langle\tilde{p}_i|\tilde{\psi}_j\rangle = \sigma_{ij}. \quad (2.43)$$

Note that the larger is the augmentation sphere the smoother are the pseudo wave functions [47]. For the PAW method to be exact, an infinite number of projectors and partial waves is required. For practical applications of the PAW method, an accurate dataset usually needs one or two projection functions for each angular momentum.

Let us now jump to a different difficulty. Calculations in infinite systems like solids require quite often integrations over a continuum of variables. This will be our next point of interest in this section.

2.5.3 K-points Sampling

In practice, for the calculation of physical quantities such as wave functions, total energies, and electron densities, a summation over all the lowest eigenvalues has to be performed. For systems like solids, which are represented through infinite periodic components, the set of wave vectors \vec{k} is a continuum. As a consequence, the electronic charge density can be written as an integral over the first Brillouin-zone (BZ):

$$n(\vec{r}) = \frac{V_{\text{cell}}}{(2\pi)^3} \int_{\text{BZ}} n(\vec{k}) d\vec{k}, \quad (2.44)$$

2.5 Implementation of Density Functional Theory

where V_{cell} is the real space unit cell volume and $n(\vec{k})$ is established from the number of occupied bands N_{bands} of the electronic structure so that:

$$n(\vec{k}) = \sum_{j=1}^{N_{bands}} |\psi_{jk}|^2 \quad (2.45)$$

Hence, the band structure energy in the total energy expression can be also written in the same way as the electron density in Eq. 2.44, as a sum over all the occupied energy bands:

$$\varepsilon_{band} = \sum_{j=1}^{N_{bands}} \frac{V_{cell}}{(2\pi)^3} \int_{BZ} \varepsilon_j(\vec{k}) d^3\vec{k}. \quad (2.46)$$

Fortunately the wave functions at k -points which are close to each other, are usually very similar. This allows for a discrete sampling of the first Brillouin-zone with a finite set of k -points, instead of performing the integral over all the k -space.

There are several methods through which the integral over the Brillouin-zone is approximated and discretized as a sum over a finite number of k -points. Efficient methods are the linear tetrahedron method [63] and the Monkhorst-Pack (MP) method [64]. We will explain here the latter, which is the one used in our calculations.

By increasing the density of k -points, we may expect an increase in the calculation accuracy. However, this will result in an increase in the computational cost. Reducing the computational cost can be achieved by the method proposed by Monkhorst and Pack (MP) in 1976, which uses a uniform distribution of k -points over the Brillouin-zone. Simply, the MP method is based on the generation of a regular mesh of equally spaced k -points along the three lattice vectors in reciprocal space. Therefore, the BZ integration of a function is approximated by calculating the average value of the function over the selected k -points.

2.5.4 Numerical Calculations - VASP

All procedures that have been explained previously in this chapter served to introduce DFT as a practical method for electronic structure calculations. As we mentioned above, the solution of Kohn-Sham equations are usually obtained iteratively. Due to the huge improvements in computer's software and hardware during the last decades, the

2. DENSITY FUNCTIONAL THEORY

simulation of materials is now available with high accuracy and including an increasing number of system atoms. Nowadays, there are several DFT codes on the market for the purpose of predicting the electronic properties of materials. A general classification of the DFT codes splits them into two groups, depending on the implementation. First category would be the all-electrons codes, for which all electrons surrounding the atoms can be included in the calculations. Wien2K [65] and Gaussian [66] are popular examples for the all-electron method. The second category of DFT codes would be those specially prepared for the pseudopotential implementation. The well known SIESTA [67], CASTEP [68] and VASP [69–72] codes are among the most popular programs that allow to consider only the valence electrons, and introduce the core electrons by an effective pseudopotential. The choice of the software is usually made by a trade-off between numerical accuracy and system size.

Let us also remark that there are other possible criteria to classify the electronic structure codes. Another possibility is to distinguish between periodic and non-periodic systems. Codes can be also classified depending on the basis-set used to expand the wave functions. A first class of codes includes softwares that use atomic orbitals as the basis-set (e.g. SIESTA). A second class includes programs that apply the plane-wave basis set (e.g. VASP). All electronic structure calculations presented in this thesis are performed by VASP. In the following lines we summarize how VASP carries out DFT calculations.

VASP is considered one of the most powerful computational tools in the field of electronic structure calculations. In VASP, the DFT is applied to periodic systems, like solids, for which first-principles electronic structure calculations and molecular dynamics simulations can be performed. VASP operates by expanding the wave functions into the plane-waves basis-set. The pseudopotential approximation is introduced for the description of the core electrons. Many exchange-correlation functionals are implemented in VASP, including LDA, GGA, meta-GGA and hybrid functionals.

In order to run calculations by using VASP, there are many input files that have to be provided to the program as a first step. POSCAR, POTCAR, INCAR, and KPOINTS are the most important files. POSCAR is the file that contains the system geometry and the ionic positions in real or reciprocal space. POTCAR is the file that contains the pseudopotential information for each atom included in the calculations. In VASP, Ultra-Soft (US-PP) and Projector Augmented Wave (PAW) pseudopotentials for most

2.5 Implementation of Density Functional Theory

of the periodic table elements can be used. The INCAR file, considered to be the driver of the program, contains all parameters that tell the program ‘what to do and how to do it’. The KPOINTS file contains the k -points grid for sampling the first Brillouin-zone. In VASP, the solution of the Kohn-Sham equations is achieved self-consistently with an iterative matrix diagonalization scheme combined with the Broyden/Pulay mixing method [73, 74] for the acceleration of the convergence of the charge density. The algorithm implemented in VASP is based on the conjugate gradient scheme. Fast Fourier Transformations (FFT) are used to switch from direct to reciprocal space and vice versa. For a given geometry, VASP algorithms first predict the Kohn-Sham wave functions, from which the electronic density can be obtained, and subsequently the electronic Hamiltonian is calculated. Then, a new value of the energy is calculated. These steps are iteratively repeated until the energy convergence criterion is reached.

Summary

The theoretical description of atoms and molecules at metal surfaces can be obtained from quantum mechanical calculations, based on the solution of Schrödinger equation. The many-body problem is insoluble analytically for systems that contain more than one electron around an atom. To simplify the problem, first, the Born-Oppenheimer approximation is introduced to separate between the nuclear and the electronic motions. The Born-Oppenheimer approximation proposes a separation between the wave functions of electrons and nuclei. The electrons are kept in their ground state and they are independent of the nuclei motion.

The appearance of DFT in the mid sixties of the last century allowed to reformulate the many-body problem. By DFT, we can deal with any number of electrons as a cloud of electron density moving in an effective potential. Several decades before, the Thomas-Fermi model was the first to use the electron density instead of the wave function to describe the electronic motion. The missing relation between electronic density and the electronic wave function was found by Hohenberg-Kohn theorem. HK first theorem proved the relation between the ground state density and the external potential. However, HK did not show a practical way to solve the many-body problem. It was later that Kohn and Sham paved the way to the now standard application of DFT, by

2. DENSITY FUNCTIONAL THEORY

proposing a set of self-consistent one-particle equations, which can be solved iteratively to find the exact ground state energy. The KS formalism provides an exact solution to the problem, but only if the exchange-correlation functional is exact. Unfortunately, the exact form of the exchange-correlation functional does not exist. The Jacob's ladder is a simple way to show the steps we can follow in order to increase the accuracy of each functional form. The exchange-correlation term in a homogeneous electron gas is the first simple procedure used to estimate the XC functional in the Local Density Approximation LDA. The Generalized Gradient Approximation, GGA, is a correction of LDA that takes into account the electron density gradient. An improvement of GGA, which takes into account not only the electron density gradient but also the kinetic energy density, is introduced under the name meta-GGA. Recently, a new generation of XC functionals has appeared, which takes advantage of a linear combination of exchange and correlation functionals. In these functionals, called hybrid functionals, we can use an exact form for the exchange functional mixed with approximate correlation functionals from the old generation.

In the last section, an implementation of DFT has been introduced that includes the calculation methods we used to perform the DFT calculations included in this thesis. We first explained that the plane-wave basis set expansion method of the wave function is our choice in order to simulate periodic metallic systems. Then, for further simplification of the problem, considering that the chemical bonding depends only on the valence electrons, we introduced the pseudopotential concept. A short discussion about the PAW method has been presented as well. A discussion on the k -points used for sampling the first Brillouin zone and on the Monkhorst-Pack method was the last point we mentioned before explaining how to perform calculations in VASP. The most important input files as well as the iterative process inside the code have been briefly discussed.

3

Theory of Gas/Surface Dynamics

Simulation of chemical reactions at surfaces requires a combination of several methodological approaches that deal with different level of theories [1, 75]. At the atomic or molecular level, density functional theory, presented in the previous chapter, is typically used to perform first-principles electronic structure calculations, which unravel the making and breaking of the chemical bond [76]. At the mesoscopic scale, the statistical theories are responsible for the quantitative competition among the different elementary processes involved in the chemical reaction. At the macroscopic scale, continuous theories yield the effect of mass and heat, ultimately scaling up to plant-wide simulations. Therefore, methodological approaches that integrate various level of theories into one multi-dimensional simulation are necessary for a complete theoretical description of catalytic process. The study of adsorption and desorption processes of atoms and molecules at surfaces, as well as surface diffusion and surface reactions is the first important step in an accurate description of the full process. Thus, DFT calculations that treat the electronic degrees of freedom and the quantum-mechanical nature of the chemical bond can be performed for the computation of reaction kinetic parameters, which constitute highly valuable results. However, such a set of kinetic parameters is not sufficient for the description of the surface catalytic function. The second step for a comprehensive study of the catalytic process is the statistical interplay of the individual elementary processes with different occurrence probabilities. The evaluation of the chemical kinetics of the involved elementary steps may face the so called “rare-event-dynamics” problem, due to the highly activated nature of these processes. Instead of the typical picosecond time scales on which the surface diffusion takes place,

3. THEORY OF GAS/SURFACE DYNAMICS

we may need to increase the simulation times up to seconds or longer in order to arrive at a meaningful conclusion concerning the statistical interplay [75]. In conclusion, the central idea for the simulation of a catalytic reaction is that it requires a combination of an accurate description of the elementary processes and their statistical interplay. For the calculation of the individual reaction probabilities, classical dynamics simulations can be very helpful, also because they allow for a detailed comparison between theory and the corresponding experiments.

For the simulations of gas-surface dynamics, the potential energy and forces need to be known at each time step [1]. One may think about performing electronic structure calculations “on the fly”, which need huge computer power. Alternatively, one may use an accurate description of the system interactions, which necessitates a continuous representation of the system potential energy surface. In Sec. 3.1 we will present the numerical methods that have been used in this thesis for the interpolation of first-principles electronic structure calculations, which take into account the molecular degrees of freedom on the surface, to construct a continuous potential energy surface. In Sec. 3.2, a detailed description of the theoretical methods used for performing classical molecular dynamics simulations will be introduced.

3.1 Continuous Potential Energy Surface

Within the Born-Oppenheimer approximation (BOA) [37] presented in the previous chapter, and due to the mass mismatch between fast electrons and slow nuclei, electrons will follow instantaneously the motion of the nuclei. This approximation reliably allows an accurate description of the gas-surface dynamics in most cases. In order to avoid the computational expenses of the ab-initio molecular dynamics (AIMD) to solve the electronic problem for a meaningful number of trajectories that describe the various reactions occurring at surfaces without losing accuracy, classical dynamics simulations performed on precalculated potential energy surfaces provide an important tool. However, for each time step of the calculated trajectories, the potential energy of atoms and molecules and the effective forces have to be well determined. As a first step to build a potential energy surface, the choice of the system relevant configurations to perform first-principles electronic structure calculations has to be carefully made. The

second step is the choice of a suitable method for the energy interpolation. Only after these two steps have been completed, we will be able to perform molecular dynamics simulations that can be used to evaluate the probabilities of the elementary reactive processes at surfaces.

In this section, the methods that have been used during this thesis for the construction of adiabatic potential energy surfaces (PES) are presented. The PESs calculated in this way are the basis for the classical dynamics simulations of the N_2 on Fe(111) system, as well as of the H on H/W(110) and H/W(100) systems. We present two different methods: (i) Local methods based on numerical interpolations for the construction of the global PES; (ii) Global methods based on fitting of analytical functions.

3.1.1 Corrugation Reducing Procedure

After performing a set of density functional theory calculations, and before running molecular dynamics, an intermediate step is the construction of a global PES by the so called ‘corrugation reducing procedure (CRP)’ [77]. CRP is a numerical interpolation method based on the initial set of previously calculated DFT energy points, which combines analytical and numerical techniques. CRP has been shown to provide very accurate results as a numerical interpolation method in the description of the interaction between diatomic gas-molecules and metal surfaces [78–81]. The major problem for interpolating numerically the DFT data arises from the large variation of energy values due to the strong repulsion between the gas-phase atoms and the surface atoms for some configurations at distances close to the surface. The clever idea behind the CRP method is that, for these very repulsive regions, the energy is mainly determined by the interaction between the individual atoms of the molecule and the surface. Then, by subtracting the atom-surface interaction, an auxiliary smoother interpolation function is produced which is much easier to interpolate than the highly corrugated 6D-PES.

Figure 3.1 represents the system coordinates that are used to define the position of the gas-phase molecule and its individual atoms at the surface. The cartesian coordinates of the two atoms are defined as $R_1(X_1, Y_1, Z_1)$ and $R_2(X_2, Y_2, Z_2)$, respectively. The molecular center of mass position is $R_{CM} = (X_{CM}, Y_{CM}, Z_{CM})$. The internal coordinates (r, θ, ϕ) , respectively stand for the internuclear distance, the polar angle relative to the surface normal, and the azimuthal angle on the surface plane and relative to the

3. THEORY OF GAS/SURFACE DYNAMICS

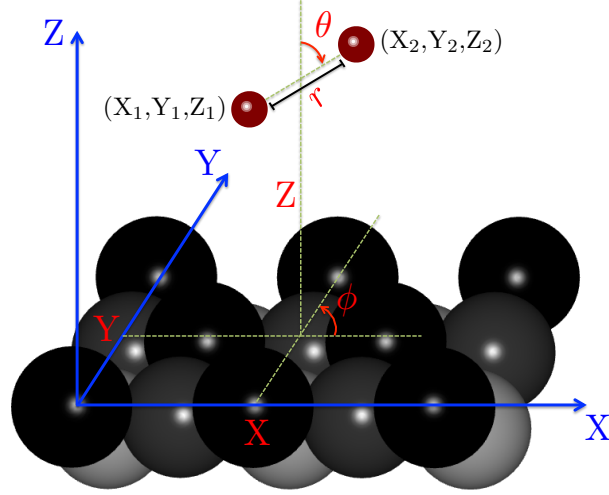


Figure 3.1: Representation of the coordinates system used to define the molecular center of mass and the individual atoms coordinates at the surface.

X-axis.

Hence, the interpolation function over the molecular six-degrees of freedom (i.e. X, Y, Z, r, θ , and ϕ) at the metal surface can be written as:

$$I^{6D}(X, Y, Z, r, \theta, \phi) = V^{6D}(X, Y, Z, r, \theta, \phi) - \sum_{i=1}^2 V_i^{3D}(X_i, Y_i, Z_i), \quad (3.1)$$

where $V^{6D}(X, Y, Z, r, \theta, \phi)$ is the DFT interaction energy between the molecule at $(X, Y, Z, r, \theta, \phi)$ and the surface, and $V_i^{3D}(X_i, Y_i, Z_i)$ is the interaction energy between atom i th of the molecule at (X_i, Y_i, Z_i) and the surface. The calculation of the 3D-PES for the atom-surface interaction should be therefore addressed as well. The 3D-PES is highly corrugated and a similar CRP method can be used. The 3D interpolation function can be written in this case as

$$I^{3D}(X_i, Y_i, Z_i) = V_i^{3D}(X_i, Y_i, Z_i) - \sum_{j=1}^n V^{1D}(|R_i - R_j|), \quad (3.2)$$

where $V^{1D}(|R_i - R_j|)$ is a one-dimensional potential describing the interaction between the atom i th at $R_i(X_i, Y_i, Z_i)$ and the j th surface atom at $R_j(X_j, Y_j, Z_j)$ and $V_i^{3D}(X_i, Y_i, Z_i)$ is the actual DFT calculated set of data for the potential energy. The one-dimensional V^{1D} potential can be approximated by the DFT calculation describing the approach of a gas-phase atom to a given first layer atom of the surface unit cell.

3.1 Continuous Potential Energy Surface

Note that the 3D-PES is highly corrugated but simpler than the 6D-PES.

For the interpolation of the 3D-PES, first, sites on the (X, Y) plane that exploit the surface symmetry and periodicity properties should be carefully selected. A set of electronic structure calculations that describe the potential energy of atoms at a distance Z from the surface and over the (X, Y) sites is performed. Once the 3D grid of data points is built, a smooth 3D interpolation function has to be constructed after removing the high repulsion from DFT-data according to Eq. 3.2. In this way, the atomic 3D PES at any point not included in the original set of data can be computed by evaluating the value of the interpolation function I^{3D} and subsequently adding the surface corrugation.

A similar procedure can be followed to construct the 6D interpolation function I^{6D} in Eq. 3.1. First, we need to perform 6D-DFT calculations for the interaction of gas-phase molecules with the surface. Likewise the atomic case, the 6D-DFT grid of data necessitates a significant number of ab-initio calculations accounting for the molecular degrees of freedom (DOF) on surface sites relevant to the dynamical studies. Once this set of data is calculated and the interpolation function is obtained after removing the corrugation, the interpolation over the molecule DOFs proceeds through four steps as follows:

- **Interpolation over (r, Z)** : Two consecutive spline interpolations performed directly over the previously calculated ab-initio (r, Z) cuts.
- **Interpolation over ϕ** : By using trigonometric functions as basis functions, the interpolation over the azimuthal angle ϕ is carried out.
- **Interpolation over θ** : Again, the interpolation over θ is performed by means of some trigonometric functions used as basis set.
- **Interpolation over (X, Y)** : A low order Fourier expansion is used for the interpolation over the (X, Y) surface coordinates. The Fourier expansion is adapted to the lattice symmetry.

A detailed description of the various techniques used for the interpolation of the 6D PES needed in the particular problem of N_2 on Fe(111) is presented in Appendix A. The CRP provides highly efficient continuous representations of the potential energy and its first and second order derivatives. Usually, the CRP accuracy is tested by

3. THEORY OF GAS/SURFACE DYNAMICS

comparing interpolated energy values with the corresponding ab-initio values, making use of configurations that are not previously included in the DFT original set of data. The typical errors from the CRP interpolations are small (less than 100 meV) and usually arise at distances very close to the surface, where high corrugation does exist. Indeed, the CRP accuracy could be systematically improved by adding more ab-initio calculations for the grid of data points. In practice, dynamical calculations based on a 6D-PES constructed by the CRP method are usually much faster than those based on other interpolation methods. Although there are many advantages of using the CRP method, some limitations are also introduced. For example, the degrees of freedom of the surface atoms are missing, an aspect which is not trivial at all. It is also important to mention the difficulty of developing the analytics of the PES interpolation, as well as programming them into computational codes. Last, but not least, the appropriate selection of the DFT-grid of data points represents a challenge compared to other automatic interpolation methods [1].

3.1.2 Flexible Periodic London-Eyring-Polanyi-Sato

One of the first steps to model the interactions of gas-phase atoms was presented in the early work of London in 1929 [82]. London's model for the determination of the potential energy for a system of three one-electron atoms assumed that the chemical reactions can be considered adiabatic, i.e., that the energy of the system continuously varies with the interatomic distance. Few years after this, Eyring and Polanyi [83] investigated a three hydrogen ($\text{H}+\text{H}_2$) atoms reaction in the gas-phase, based on London expression. Then, Sato [84] introduced an adjustable parameter substituting the overall integrals, called Sato parameter. The London-Eyring-Polanyi-Sato (LEPS) expression, so obtained, was first modified to study the interaction of a diatomic molecule with a rigid surface by McCreery and Wolken [85]. The modification was employed to study the interaction of hydrogen and its isotopes with a surface [86, 87].

According to the LEPS model, the 6D potential energy for a molecule made of two

3.1 Continuous Potential Energy Surface

atoms, as shown in Fig. 3.1, interacting with a periodic solid surface is given as follows:

$$\begin{aligned}
 V(R_A, R_B) = & U_{AS}(R_A) + U_{BS}(R_B) + U_{AB}(\|R_B - R_A\|) \\
 & - \left[Q_{AB}(\|R_B - R_A\|) + \left(Q_{AS}(R_A) + Q_{BS}(R_B) \right)^2 \right. \\
 & \left. - Q_{AB}(\|R_B - R_A\|) \left(Q_{AS}(R_A) + Q_{BS}(R_B) \right) \right]^{\frac{1}{2}}, \quad (3.3)
 \end{aligned}$$

where R_A and R_B define the positions of atoms A and B , respectively, and $\|R_B - R_A\|$ is the internuclear distance. U_{ij} and Q_{ij} respectively represent the Coulomb potential and the exchange integrals terms for atom-surface and atom-atom interactions ($ij = AS, BS, AB$), which have the forms:

$$U_{ij} = \frac{D_{ij}}{4(1 + \Delta_{ij})} \left[(3 + \Delta_{ij})e^{-2\alpha_{ij}(R_{ij} - R_{AB}^{eq})} - (2 + 6\Delta_{ij})e^{-\alpha_{ij}(R_{ij} - R_{AB}^{eq})} \right], \quad (3.4)$$

and

$$Q_{ij} = \frac{D_{ij}}{4(1 + \Delta_{ij})} \left[(1 + 3\Delta_{ij})e^{-2\alpha_{ij}(R_{ij} - R_{AB}^{eq})} - (6 + 2\Delta_{ij})e^{-\alpha_{ij}(R_{ij} - R_{AB}^{eq})} \right]. \quad (3.5)$$

R_{AB}^{eq} , D_{ij} and α_{ij} in Eqs. 3.4 and 3.5, are the well known Morse parameters. R_{AB}^{eq} represents the molecule internuclear equilibrium distance, D_{ij} is the dissociation energy and α_{ij} is the Morse shape parameter. The Sato parameters Δ_{ij} are usually chosen to fix some of the PES properties such as location and height of energy barriers [1].

The periodicity of the solid surface is represented by the periodic LEPS model (PLEPS), for which a Fourier expansion is usually employed to describe the dependence of Morse parameters on surface coordinates (X, Y). The Sato and Morse parameters of the PLEPS model have to be determined by fitting ab-initio or experimental data in three steps. The procedure is usually as follows: First, the 1D molecular potential ($U_{AB} + Q_{AB}$) is built from Eqs. 3.4 and 3.5. Second, the 3D atom-surface interactions ($U_{AS,BS} + Q_{AS,BS}$) are obtained for various surface sites. The 6D potential $V(R_A, R_B)$ is finally constructed by substitution of Eqs. 3.4 and 3.5 in Eqs. 3.3.

Due to the simplicity of the analytical form of the PLEPS model and the small number of ab-initio data required for the fitting procedure, the PLEPS model is a popular choice in constructing continuous PESs for gas-surface dynamics simulations. In particular, the PLEPS model has been shown to provide good results for Eley-Rideal and Hot-Atom reaction processes (e.g., H/H-Cu(111) [88], H/H-Ni(100) [89], H/Cl-Au(111) [90],

3. THEORY OF GAS/SURFACE DYNAMICS

H/H-Ni(100) [91]). However, the PLEPS model is better suited for simple and low-corrugation PESs. Some limitations for the model do exist. The PLEPS model, for instance, is unable to describe the presence of two barriers in the dissociation path. Generally speaking, the PLEPS model may lack flexibility in describing the gas-surface interactions characterized by corrugated PESs and complicated reaction paths.

Due to the failure of the PLEPS model to describe the interaction between the nitrogen molecule and tungsten surfaces, Martin-Gondre and coworkers developed a flexible extension of the PLEPS model to describe the dissociation of N₂ on W(100) [92–94]. In the Flexible Periodic LEPS or FPLEPS model, the Sato parameters dependence on the surface coordinates (X, Y) is introduced. Indeed, one can make the FPLEPS model to reproduce the entrance barrier through the introduction of Gaussian functions. The angular representation (θ, ϕ) is done via the Gaussian and Sato parameters, while the surface corrugation (X, Y) is introduced by a 2D-spline method and Fourier expansion. Thus, the 6D potential energy in Eq. 3.3, with the additional Gaussian functions can be written as:

$$\begin{aligned}
 V(R_A, R_B) = & U_{AS}(R_A) + U_{BS}(R_B) + U_{AB}(\|R_B - R_A\|) \\
 & - \left[Q_{AB}(\|R_B - R_A\|) + \left(Q_{AS}(R_A) + Q_{BS}(R_B) \right)^2 \right. \\
 & \left. - Q_{AB}(\|R_B - R_A\|) \left(Q_{AS}(R_A) + Q_{BS}(R_B) \right) \right]^{\frac{1}{2}} \quad (3.6) \\
 & + A_g \left[- \frac{(Z_{CM} - Z_g^0)^2}{\sigma_g^2} \right],
 \end{aligned}$$

where Z_{CM} is the molecular center of mass distance from the surface, and A_g , Z_g^0 , and σ_g are the parameters of the Gaussian function. In the investigation of N₂/W(100), the performance of classical calculations on the PES constructed from FPLEPS shows a good agreement with those performed on a DFT-based PES, which is a remarkable success of the FPLEPS model[93, 94].

The use of the analytical expression of FPLEPS in order to build a potential energy surface provides an appropriate starting point for performing classical dynamics simulations. The number of ab-initio calculations required is small compared to the local methods (i.e. CRP), for which a large number of points is needed. In addition, the FPLEPS method is flexible enough to be applied to the study of many elementary gas-surface reaction processes for various systems. Still, only semi-quantitative results

should be expected. However, in the study of Eley-Rideal and Hot-Atom recombinations, FPLPES has shown quantitative agreement with the CRP interpolation method (e.g., $\text{N}_2/\text{W}(100)$ [25], $\text{H}/\text{H-W}(100-110)$ [95], $\text{H}/\text{H-W}(110)$ [96]).

3.2 Classical Dynamics Simulations

In the previous chapter, methods for performing electronic structure calculations (i.e., DFT) within the Born-Oppenheimer approximation were presented. In the current chapter, Sec. 3.1 shows various interpolation methods for the continuous representation of the DFT data in order to build a global PESs. The properties of the PES provide highly valuable information about the system under study, such as the possible adsorption states as well as an estimation of the entrance and dissociation barriers. However, these informations are still not sufficient for the detailed description of gas-surface elementary reaction processes. Once the PES for the system has been constructed, statistical calculations have to be performed, either by quantum or classical dynamics. Quantum dynamics treat in principle exactly the motion of the incoming nuclei but they are usually very expensive from the computational point of view. We should remember that due to the mass difference between the atoms of the gas-phase molecules considered and the surface atoms, the electronic motion is independent of the nuclei motion and we can remain at the level of the Born-Oppenheimer Static Surface (BOSS) approximation [97–99], in which the atoms of the surface remain motionless. The BOSS approximation neglects however all the inelastic processes, i.e., neither the electron-hole pair excitations nor the energy exchange and dissipation from the molecule to the lattice are included. However, the surface degrees of freedom should be also involved in a realistic and accurate description. All in all, classical dynamics methods, in which the energy dissipation to the lattice can be introduced in a reasonable way through Langevin dynamics, become a practical choice for the prediction of reaction probabilities.

The total energy of the molecule interacting with the surface is defined by a Hamiltonian, which is given as a sum of the translational energy of the molecule plus the PES

3. THEORY OF GAS/SURFACE DYNAMICS

value,

$$H(X, Y, Z, r, \theta, \phi) = \frac{1}{2}(p_X^2 + p_Y^2 + p_Z^2) + \frac{1}{2\mu}(p_r^2 + \frac{p_\theta^2}{r^2} + \frac{p_\phi^2}{r^2 \sin^2 \theta}) + V^{6D}(X, Y, Z, r, \theta, \phi), \quad (3.7)$$

where μ is the reduced mass of the molecule and p_i are the linear momenta components. According to classical mechanics, the Newton's equation of motion that describe the movement of the atoms has the expression:

$$M_i \frac{\partial^2}{\partial t^2} R_i = - \frac{\partial^2}{\partial R_i} V^{6D}(R_i, R_j), \quad \text{with } i, j = 1, 2 \text{ and } i \neq j. \quad (3.8)$$

In Eq. 3.8 the forces acting on an atom are obtained as the derivative of the PES, where M_i are the atomic masses and V^{6D} is the 6D potential energy when the two atoms are at positions R_1, R_2 . There are several methods to perform the integration of these equations of motion. The predictor-corrector algorithm of Burlisch and Stoer [100] was the one used in the current work.

In the following we will first present the model used to simulate the movement of the surface atoms and the energy exchange between the projectile (atoms and molecules) and the surface lattice. After this, a discussion on the methods used for sampling the initial conditions of the dynamics, followed by an explanation of the reactions final channels, will be addressed.

3.2.1 Generalized Langevin Oscillator

The Generalized Langevin Oscillator (GLO) model [101–103] is a general theoretical framework for the introduction of lattice effects into the gas-solid dynamics. In the dynamical study of the elementary processes, the GLO model accounts for the representation of the energy exchange and dissipation between the gas-phase species and the surface lattice. The GLO model permits further simplification of the system, by reducing the many-body equations of motion associated with all atoms in the solid and focusing only into the local surface region in which the interaction with the gas-phase atoms-molecules takes place. The remaining surface atoms are represented by a thermal bath.

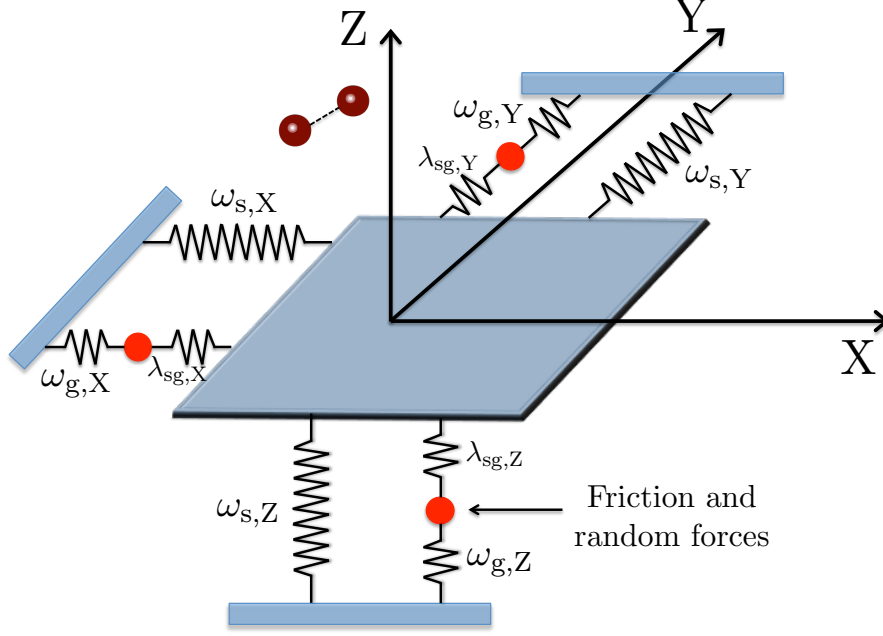


Figure 3.2: Schematic representation of the Generalized Langevin Oscillator (GLO) model. The figure is taken from Ref. [104].

In the case of a gas-phase molecule colliding with a metal surface, the dynamical process is represented as a four-body problem consisting of the two-atoms of the molecule, and two 3D harmonic oscillators. The first harmonic oscillator represents the surface, and the second harmonic oscillator (ghost oscillator) provides the thermal bath. Then, the classical equations of motions of the four-body problem are

$$\frac{d^2 R_{A,B}}{dt^2} = - \frac{1}{m_{A,B}} \nabla_{R_{A,B}} V^{6D}(R_A - R_s, R_B - R_s), \quad (3.9)$$

$$\frac{d^2 R_s}{dt^2} = - \frac{1}{m_s} \nabla_{R_s} V^{6D}(R_A - R_s, R_B - R_s) - \hat{\omega}_s^2 R_s + \hat{\lambda}_{sg} R_g, \quad (3.10)$$

$$\frac{d^2 R_g}{dt^2} = - \hat{\omega}_g^2 R_g + \hat{\lambda}_{sg} R_s - \hat{\gamma}_g \frac{dR_g}{dt} + \frac{1}{m_s} F_r(t), \quad (3.11)$$

where $R_{s,g}$ and $\omega_{s,g}$ respectively represent the coordinates of the 3D harmonic oscillators of the surface and the ghost atoms and the associated 3×3 frequency matrices. Equation 3.9 represents the motion of the gas-molecule due to the adiabatic force obtained from the 6D-PES. The only difference with respect to Eq. 3.8 is that the surface is now allowed to move and the reference system of coordinates is accordingly shifted.

3. THEORY OF GAS/SURFACE DYNAMICS

Equations 3.10, 3.11 represent the motion of the surface and ghost atoms. The energy-exchange of the surface with the bulk is included in the coupling matrix $\hat{\lambda}_{sg}$, between the surface and ghost oscillators. The ghost oscillator is associated with a friction force through a damping matrix $\hat{\gamma}_g$ and a random force $F_r(t)$ which relate to each other through:

$$F_r(t) = \frac{2 k_B T_s \gamma_g}{m_s \Delta t}, \quad (3.12)$$

where k_B is the Boltzmann constant, T_s is the surface temperature, and Δt is the integration time step used in the simulation. We can summarize the function of the ghost oscillator as a thermal bath that keeps the surface temperature at T_s . The friction force represents the energy dissipation from the surface into the bulk, while the random forces represent the energy transfer from the bulk to the surface due to the thermal vibrations of the lattice. Finally, according to Ref. [103], the frequency matrices ω_s and ω_g are taken equal, so that the oscillator frequency values can be easily obtained either experimentally or by the calculations of the surface phonons frequencies close to the Brillouin zone edges of the metal surface [1]. Furthermore, the damping matrix $\hat{\gamma}_g$ can be obtained from the Debye frequency ω_D [102]:

$$\hat{\gamma}_g = \frac{\pi}{6} \omega_D \hat{I}, \quad (3.13)$$

with \hat{I} being the unit matrix.

In case that the electron-hole pair excitations are included in the dynamics as an additional term in the dissipative force [105], Eq. 3.9 will be replaced by:

$$\frac{d^2 R_{A,B}}{dt^2} = - \frac{1}{m_{A,B}} \nabla_{R_{A,B}} V^{6D}(R_A - R_s, R_B - R_s) - \frac{1}{m_{A,B}} \eta(R_{A,B} - R_s) \frac{dR_{A,B}}{dt}, \quad (3.14)$$

where η is the friction coefficient due to electronic excitations in the surface. A practical way to calculate the friction coefficient is to use the local density friction approximation (LDFA), in which η is approximated as the friction coefficient of an atom moving in a homogeneous free electron gas with an electron density equal to that of the surface position in which the atom is placed [105].

3.2.2 Sampling the Initial Conditions

So far, we have described the methods used for launching the dynamics of a single molecule interacting with the surface. In classical calculations, the probability for each individual process is evaluated as an average over all possible initial conditions. A conventional Monte Carlo procedure is used in this work to sample the initial molecular coordinates (X, Y) and the molecular orientation $(\theta$ and $\phi)$. Usually the initial conditions fix the coordinates and conjugate momenta of the system under study.

In performing classical dynamics we can distinguish between pure classical and quasi-classical dynamics. In the latter, the zero point energy (ZPE) of the molecule is included in the calculation, whereas in the former the ZPE is assumed to be zero [106]. For sampling the initial positions of the center of mass coordinates, it is not possible to consider all the volume of the phase space. Instead, a finite number of points is used for the representation of the surface sampling area. Hence, a random number generator is used for the generation of the molecular coordinates (X_{CM}, Y_{CM}) , the angular orientation of the molecule (θ, ϕ) , as well as the surface atoms coordinates at $t = 0$. The initial distance from the surface Z_{CM} is usually taken sufficiently far so that the interaction can be considered as negligible. The internuclear distance r , in most cases, is fixed to that of equilibrium in the vacuum. The initial rotational and vibrational states of the projectile and the temperature are inserted as external data.

Once all the initial conditions are defined, the classical equations of motion are solved according to Eqs. 3.9, 3.10, and 3.11 for the four body problem until the integration time limit is reached. The forces acting on the particles are calculated at each time step from Eq. 3.9.

3.2.3 Final Channels of the Dynamics

As a consequence of the interactions between atoms and molecules and the surface, the final states of the trajectory can be classified into several possible exit channels:

- **Reflection:** When the atom or the molecular center of mass reaches for a second time the initial height from the surface, with positive velocity pointing towards the vacuum.

3. THEORY OF GAS/SURFACE DYNAMICS

- **Dissociative adsorption:** When the molecule bond length reaches the value of twice the equilibrium bond length (i.e., $r = 2r_{eq}$).
- **Molecular trapping:** When the molecule is neither reflected nor dissociated after the integration time limit is reached. When the total energy of the molecule is negative, this process can be labeled as molecular adsorption.
- **Eley-Rideal abstraction:** For atomic incidence, it occurs when the projectile atom combines with a target atom with only one rebound of the center of mass of the newly formed molecule happening after the first collision between projectile and surface.
- **Hot-Atom abstraction:** For atomic incidence, it occurs when the projectile atom combines with a target atom with many rebounds of the center of mass of the newly formed molecule happening after the collision between projectile and surface.
- **One-atom adsorption:** When only one atom has a negative energy and it is not reflected after the integration time limit is reached.
- **One-atom absorption:** When only one atom has a Z -height value below the minimum value defined by the PES (Z_{min}).
- **Two-atoms absorption:** When two atoms have a Z -height value below the minimum value defined by the PES (Z_{min}).

3.3 Summary

Classical dynamics simulations are an effective tool for understanding the elementary reactions at surfaces. Besides the low calculation cost, more realistic simulations can be extracted, due to the insertion of additional degrees of freedom of the system under study. However, in the classical trajectory calculations, both the potential energy and forces should be defined for all the points in space. Therefore, we have presented in the first section of this chapter the numerical tools used for the interpolation of data obtained from electronic structure calculations. First, the CRP was discussed in detail as a local method based on numerical interpolations. In the CRP, the surface corrugation

is reduced by subtracting the high repulsion from the DFT-data, and a smooth interpolation function is constructed, which is much easier to interpolate than the highly corrugated original 6D-PES. The accuracy of the CRP procedure is usually tested by comparing the interpolated data with additional ab-initio electronic structure calculations for various sets of off-grid molecular configurations. The CRP provides highly accurate and efficient PESs, although small errors may exist at distances very close to the surface. The CRP accuracy can be systematically improved by adding more points to the grid of data. In addition, the flexible periodic LEPS model is also introduced as a global interpolation method based on analytical functions. The FPLEPS model is flexible enough to study the gas-metal interactions for large systems that include complicated reaction paths. The FPLEPS form requires the introduction of some analytical parameters and a lower number of DFT-data as compared to CRP. The FPLEPS accuracy is still just semi-quantitative when compared to CRP, but the FPLEPS has shown to be an effective and accurate method in ER and HA abstraction dynamics.

A general overview concerning classical dynamics simulations is presented in the second section. Classical trajectory calculations are usually performed through the integration of Newton's equation of motion. The forces acting on atoms and molecules in the trajectory path are obtained as the derivatives of the PES. Surface temperature effects as well as energy exchange and dissipation between the molecule and the surface lattice are included through the GLO model. In the GLO model, the surface motion is represented in terms of a three-dimensional harmonic oscillator. In order to consider the coupling and energy-exchange of the surface with the bulk, an additional three-dimensional ghost oscillator is coupled to the surface oscillator. The ghost-oscillator is subject to friction and random forces related to each other through the second fluctuation-dissipation theorem. The ghost oscillator allows us to represent the bulk of the solid as a thermal bath at the chosen surface temperature. An adequate choice of the initial conditions is crucial to ensure good representation of the final statistics. The results from classical dynamics calculations may end up in different final states, depending on the system. We have defined the main final channels that are the outcome of our calculations and that will be used for comparison with experimental information.

3. THEORY OF GAS/SURFACE DYNAMICS

4

Fe(111) Surface Slab Relaxations

Iron is one of the most abundant elements in Earth. Its cheap price, together with its physical and chemical properties, have made of iron one of the most attractive metals for both technological and research purposes. Pure iron can crystallize into different structures, but the most common Fe stable structure is the α -phase of the bcc-structure. Figure 4.1 illustrates the Fe-bcc crystal. The planes defined by red lines show the low-index iron surfaces [i.e. (100), (110), and (111)].

In surface science, it is known that the surface properties are different to the bulk ones, due to the removal of chemical bonds in one direction, which may result in relaxations or in some cases reconstructions of the surface topmost layers. In other words, the surface atoms may move trying to minimize the surface energy. In particular, Fe surfaces are known to exhibit only relaxation and the surface reconstruction does not exist [107–109]. Focusing in the main interest of this thesis, the relaxation of the surface atoms should be addressed in any study of the reactions between gases and Fe surfaces. There are several experimental and theoretical works on the surface expansions or contractions. The general accepted conclusion is that the more open the surface, the more important the relaxation is [110]. Results from previous studies predict that the relaxation parameters increase almost linearly with the openness or roughness of the surface [111].

One of the difficulties when treating with the (111) face of Fe is that contradictory experimental and theoretical results have been obtained on the relaxation suffered by the first surface layers [112–117]. The disagreement, as will be shown later, can be not only quantitative but also qualitative. The absolute value of these differences is

4. FE(111) SURFACE SLAB RELAXATIONS

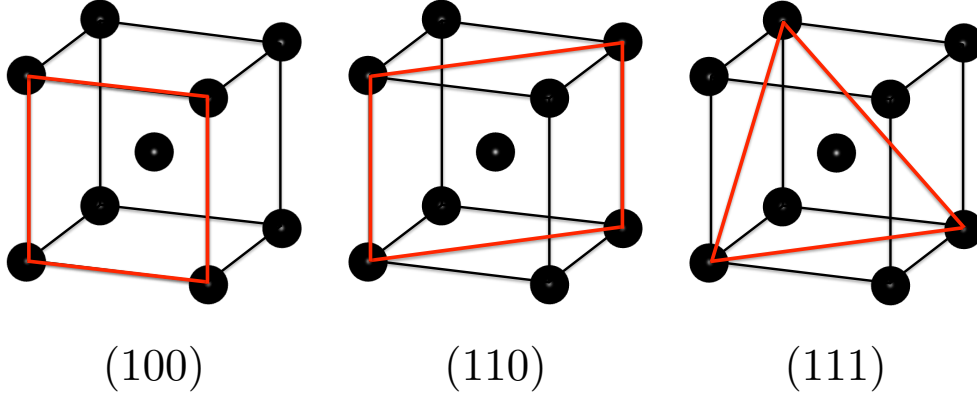


Figure 4.1: Schematic illustration of the low-index Fe surfaces $\{(100), (110), \text{ and } (111)\}$. The red lines show the respective planes

not particularly large, however, due to the small interlayer distance in the Fe(111) surface. We start this work with a theoretical study of the relaxation of the Fe(111) surface based on DFT calculations. With this analysis we intend to offer new insight into the difficult puzzle of Fe(111) relaxation in order to set the necessary basis for the subsequent study of the N atom and N₂ adsorption processes.

4.1 Methodology

We perform first-principles spin polarized DFT [44, 45] calculations, as implemented in the VASP package [69–72]. In our calculations, the exchange correlation energy is obtained from the spin-polarized version of the GGA [118], with the PW91 exchange-correlation functional. The PW91-GGA usually provides reasonable accuracy about structural information and binding energy [50]. The electron-ion core interactions are represented by the PAW pseudopotentials [61, 62]. A 400 eV cut-off energy is used for the expansion of the plane-waves basis set.

The Fe(111) surface is modeled by a periodic (2×2) unit cell as shown in Fig. 4.2.a. The surface layers are represented by a slab supercell approach, separated by a vacuum region of 15 Å, which is large enough to make the interaction between neighboring slabs negligible. The two-dimensional Brillouin zone integrations are performed through different samplings of k -points in Monkhorst-Pack grids [64]: We use $(21 \times 21 \times 21)$

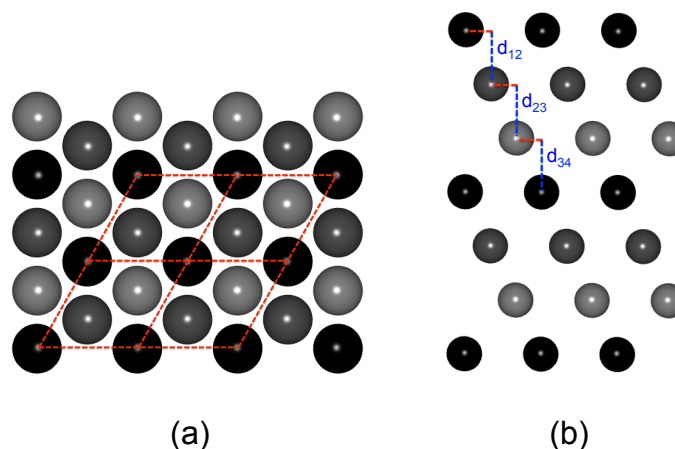


Figure 4.2: Representation of the Fe(111) surface; (a) Top view with illustration of a (2×2) unit cell. (b) Side view with the indication of the interlayer spacing d_{12} , d_{23} and d_{34} .

for the optimization of the bulk lattice constant, and $(8 \times 8 \times 1)$ for the surface slab relaxations. The mentioned choices provide the adequate balance between numerical accuracy and computational cost. Further computational details will be introduced in the subsequent sections.

4.2 Relaxation of the Fe(111) Surface Slab

The optimized bulk lattice constant is found to be $a=2.855 \text{ \AA}$ in this work, in good agreement with the experimental value of 2.867 \AA [119]. The bulk modulus B_0 is calculated by a second-order polynomial fitting of the total energy curve versus the lattice parameter. The obtained value, $B_0 = 184 \text{ GPa}$, is higher than the observed value, $B_0 = 168 \text{ GPa}$ [120], by about 10 %, and similar to other theoretical results, $B_0 = 188 \text{ GPa}$ [121]. Table 4.1 presents the optimized values from previous studies on the Fe-bulk parameters (a , B_0). Generally speaking, our results show a good agreement with previous theoretical and experimental studies.

The Fe(111) surface is modeled using a Fe slab with the thickness ranging between 7 and 19 layers. The atoms in the slab are allowed to move freely in the three directions of space (X , Y , and Z) during the structural relaxation. Only the central layer in the slab is kept fixed during the relaxation. In our calculations, we observe that the Fe

4. FE(111) SURFACE SLAB RELAXATIONS

	PBE [114]	PW91 [121]	Experimental	This work
Lattice constant a (Å)	2.844	2.830	2.867 [119]	2.855
bulk modulus B_0 (GPa)	165	188	168 [120]	184

Table 4.1: Previous calculations of the lattice constant a in Å and the bulk modulus B_0 in GPa for bulk Fe, from different exchange-correlation functionals, PW91 [121] and PBE [114]. Experimental values are also shown [119, 120].

atoms only move in the Z -direction (perpendicular to the surface) whereas no movement in the XY - plane takes place. Hence, the Fe(111) surface exhibits only relaxation in the perpendicular direction and no surface reconstruction, as was already found before [109].

We define the relaxation of the inter-planar distance between surface layers as the variation of the surface interlayer distance relative to the bulk interlayer spacing, as shown in Fig. 4.2.b: $\Delta_{ij} = (d_{ij} - d)/d \times 100$, where d_{ij} is the distance between the i th layer and the j th layer and $d = 0.82$ Å is the bulk interlayer spacing. In Fig. 4.3, the variations of the first three interlayer distances (Δ_{12} , Δ_{23} , and Δ_{34}) are represented as a function of the number of layers in the slab.

Figure 4.3 shows our calculations for the structural relaxation of different Fe(111) slabs. The relaxation values in Fig. 4.3 show the convergence of our results with the number of layers in the slab. For a slab consisting of 9-layers, we obtain $\Delta_{12} = -7.8\%$ ($d_{12} = 0.74$ Å), $\Delta_{23} = -21.7\%$ ($d_{23} = 0.64$ Å) and $\Delta_{34} = 9.7\%$ ($d_{34} = 0.90$ Å), where the negative sign means a contraction inwards and the positive sign means an expansion outwards. The overall contraction of the first three interlayer spacing is of $-17,43\%$. Looking at these numbers, one can say that the Fe(111) surface exhibits strong relaxation as compared with the other two low-index iron surfaces Fe(110) and Fe(100) [112, 114, 122]. This is not particularly surprising because Fe(111) is the most open iron surface among the three low-index surfaces and, according to Finnis-Heine [123] theory, the openness of the surface is related to the magnitude of the relaxation.

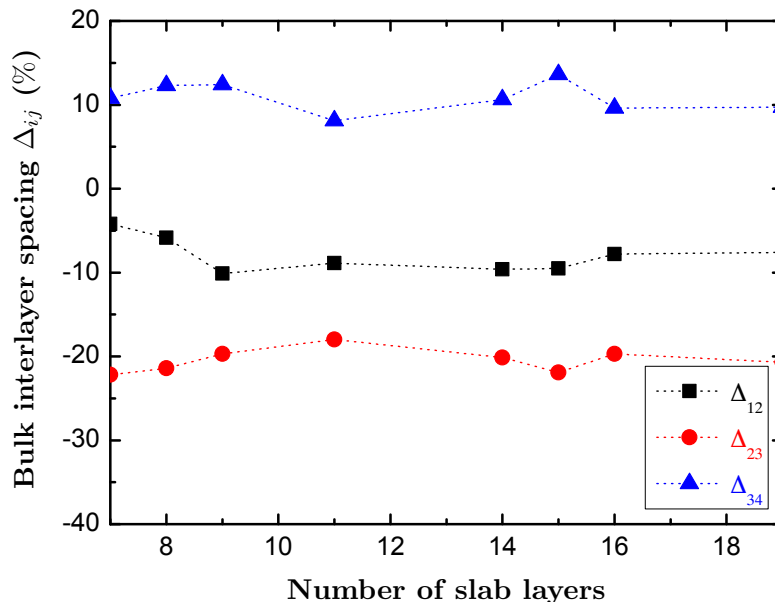


Figure 4.3: Variation of interlayer spacing Δ_{ij} as a percentage of the bulk interlayer spacing for a Fe(111) surface with the number of layers in the slab and up to 19-layers.

Table 4.2 summarizes previous studies of the Fe(111) surface relaxation, including both experimental measurements and theoretical calculations. Table 4.2 also shows that different experimental techniques offer contradictory results with respect to the relaxation. Low Energy Electron Diffraction (LEED) measurements [115] show that the first two interlayer spacings are contracted and the third one expanded. However, Medium Energy Ion Scattering (MEIS) results [116, 117] show that only the first layer contracts and the second layer expands. Similar discrepancies are found among previous theoretical calculations for the magnitudes of the topmost three slab layers relaxations [112–114]. Our results are in qualitative agreement with the LEED measurements as well as with the most recent theoretical calculations. Quantitative differences are however found.

The ultimate goal of our work is to study the interaction of nitrogen atoms and molecules with the Fe(111) surface. Therefore, it is necessary to test whether the substitution of the semi-infinite Fe surface for a finite relaxed slab in our calculations affects the interaction energy between nitrogen and iron. In order to verify this point, we have performed individual calculations for the interaction of nitrogen molecules with Fe slabs with a different number of layers. Within the frozen surface approximation, Fig. 4.4 illustrates the interaction energy of N_2 on Fe(111) as a function of the distance

4. FE(111) SURFACE SLAB RELAXATIONS

Surface	Δ_{12}	Δ_{23}	Δ_{34}	Δ_{45}	Δ_{56}	Δ_{67}	Δ_{78}	Reference
Fe(111)	-13.3	-3.6	13.3	-1.2	0.35			Theory [112]
	-6.74	-16.89	12.4					Theory [113]
	-17.7	-8.4	11.0	-1.0	-0.5	0.1	-1.2	Theory [114]
	-16.9 ± 3	-9.8 ± 3	4.2 ± 3.6	-2.2 ± 3.6				LEED [115]
	-29.0 ± 7	6 ± 5						MEIS [116]
	-27.0 ± 5	5 ± 4						MEIS [117]
	-7.8	-21.7	9.7	-1.1				This work

Table 4.2: Previous calculated and experimental results for the relaxation of the Fe(111) surface. Δ_{ij} is the interlayer spacing between layers i and j (in % of the bulk spacing d), extracted from references [112–117].

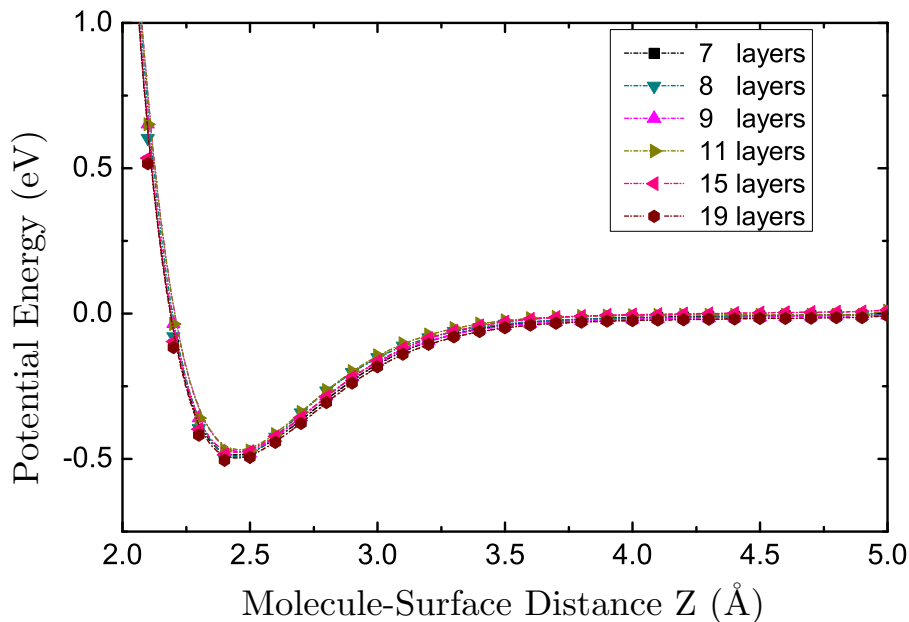


Figure 4.4: Dependence of the N_2 adsorption energy on the number of slab layers. The N_2 potential energy is plotted as a function of the vertical distance from the surface (Z). The molecule is located on top of a first-layer atom, with its axis oriented perpendicular to the surface plane ($\theta = 0^\circ$). The internuclear distance is fixed to the equilibrium bond length in vacuum, $r_{eq} = 1.1125 \text{ \AA}$.

between the molecular center of mass and the surface Z . All the configurations shown in the plot correspond to the N_2 molecule oriented perpendicular to the surface first layer atoms ($\theta = 0^\circ$, top configuration). The reference energy is taken to be that of the N_2 molecule at 5 \AA from the surface and at the equilibrium bond length ($r_{eq} = 1.1125 \text{ \AA}$). For a sufficient number of slab layers, our DFT calculations show that the magnitude of the N_2 adsorption energy is independent of the number of layers in the slab. Such conclusion ensures the convergence of our results in the next sections with the number of layers in the slab.

4.3 Summary

We have performed a large set of DFT calculations to understand different aspects of the Fe(111) surfaces. We first study the relaxation of the topmost surface layers of

4. FE(111) SURFACE SLAB RELAXATIONS

Fe(111) as a function of the number of slab layers. The first two interlayer distances are shown to be shortened with respect to the bulk value (contraction), while the third one is shown to be enlarged (expansion). Our results show a qualitative agreement with LEED measurements as well as with other recent DFT studies, although some quantitative differences have been found. Furthermore we have tested the adequacy of the slab representation for the calculation of adsorption energies by calculating the potential energy of N_2 approaching the surface in a perpendicular orientation, on top of the Fe(111) first layer atoms. We have checked that the adsorption energy of N_2 on Fe(111) does not depend on the number of slab layers.

5

Potential Energy Surfaces of Nitrogen on Iron

Detailed studies of the dynamics of elementary reactions at surfaces may require the construction of continuous potential energy surfaces (PESs), based on electronic structure calculations. The static analysis of the system energy landscape can give us a general idea about the surface activity in chemical reactions. Before going into a deeper analysis of the dynamics, the PES can provide us with a first estimate of atoms and molecules favorable adsorption sites as well as adsorption energies and trace the activated and non-activated paths for the dissociation process, from a purely static point of view.

In this chapter, we studied the interaction energy of atomic and molecular nitrogen with a clean Fe(111) surface, within the frozen surface approximation. Based on our previous findings for the surface structural relaxations, we performed our DFT calculations on a slab consisting of a fixed number of layers. This chapter is arranged as follows: In Sec. 5.1 we present the details of the methods used to perform the electronic structure calculations. Section 5.2 provides the atomic potential energy surface (3D-PES) for the N/Fe(111) system. Section 5.3 includes the construction of the full six dimensional potential energy surface (6D-PES) for the N₂/Fe(111) system. In Sec. 5.4 we present a summary of the chapter.

5.1 Electronic Structure Calculations

All the ab-initio data are obtained using the DFT [44, 45] VASP code [69–72]. The exchange-correlation energy is calculated with the GGA [118] and the PW91 energy functional [50]. The (valence) electron-core interaction is described with PAW pseudopotentials [61, 62]. Due to the magnetic nature of the Fe(111) surface, spin-polarized DFT calculations are performed. The energy cutoff in the plane-wave expansion is 400 eV; the fractional occupancies are determined through the broadening approach of Methfessel and Paxton with $N=1$ and $\sigma = 0.2$.

A 2×2 unit cell is used to model the periodicity of the Fe(111) surface in the (X, Y) plane. In the previous chapter we have investigated some features of the structural relaxation of the Fe(111) surface layers. The results showed an independence between the interlayer relaxation and the number of layers in the slab, provided a minimum number of layers was used. We perform the present DFT calculations within the frozen surface approximation and using a slab consisting of 9-layers and separated by a vacuum layer of 15 Å width, which is tested to be large enough to avoid the interaction between neighbouring slabs. The two-dimensional Brillouin-zone integrations are performed by sampling the k -points with $6 \times 6 \times 1$ Monkhorst-Pack grids [64], which provide an adequate balance between numerical accuracy and computational burden.

The obtained theoretical lattice constant is $a = 2.855$ Å, which leads to an interlayer spacing of $d = a/2\sqrt{3} \approx 0.824$ Å in bulk. We observed that, due to its small interlayer distance, a slab of at least 9 layers was necessary to appropriately model the relaxation of the Fe(111) surface. For a slab consisting of 9 layers, the net interlayer spacing values are $d_{12} \approx 0.74$ Å, $d_{23} \approx 0.64$ Å and $d_{34} \approx 0.90$ Å, where d_{ij} is the distance between the i - and j - layers. No further relaxation due to the interaction of the surface with the nitrogen species is considered. It should be noted, however, that Refs. [124, 125] reported that the (111) surface of Fe may exhibit reconstruction after interaction with abundant nitrogen, in the form of “surface nitrides”. Therefore, our calculations are representative only of the low-coverage regime of nitrogen on Fe(111).

Here, we first investigate the interaction of N atoms with the surface at positions that are representative of the surface symmetry. After this, we obtain the full set of DFT calculations for the six degrees of freedom of the nitrogen molecule on Fe(111).

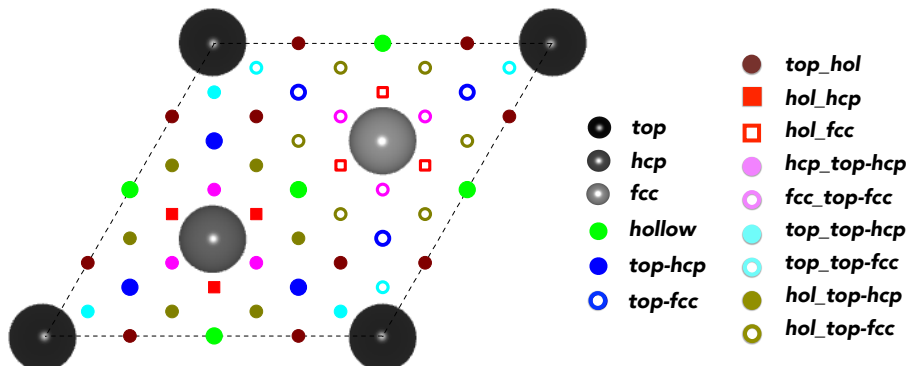


Figure 5.1: Representation of the Fe(111) unit cell designed to fulfill the surface symmetry. Each site is indicated by an individual color, as shown in the right panel.

5.2 N/Fe(111) Potential Energy Surface

For the investigation of the interaction of nitrogen atoms approaching a clean Fe(111) surface by means of DFT calculations, we have considered 15 representative XY -sites of the surface, as shown in Fig. 5.1. We show in Fig. 5.2 the potential energy of N on Fe(111) as a function of the distance between the N atom and the Fe(111) surface for several representative sites at the surface. The asymptotic energy is taken as the energy of a nitrogen atom at a distance relatively far from the surface. Figure 5.2 shows that, among the 6 high symmetry sites (i.e. *top*, *hcp*, *fcc*, *hollow*, *top-hcp* and *top-fcc*) of the surface, the most energetically favorable configuration for atomic adsorption is the *hollow* site, with the nitrogen atom adsorbed very close to the surface, at $Z \approx 0.5$ Å. The calculated adsorption energy is $E_{ads} \approx -5.82$ eV. This value is in reasonable agreement with the energy range (-6.6 eV to -5.7 eV) obtained in previous theoretical calculations [126–131], as well as within the measured energy range (-6.1 eV, -5.9 eV) in experimental observations [124, 132, 133] for atomic nitrogen adsorbed on low-index Fe surfaces. Let us also remark here that we are calculating all these values in the frozen surface approximation, without allowing for surface relaxation when the atom approaches the surface. The reason is that we are building the 3D-PES of the system. Surface relaxation would slightly increase the absolute value of the adsorption energy and make it even more accurate.

The theoretical study of the dynamics of N atoms on Fe(111) requires the knowledge of not only some representative configurations but of the full energy landscape. A

5. POTENTIAL ENERGY SURFACES OF NITROGEN ON IRON

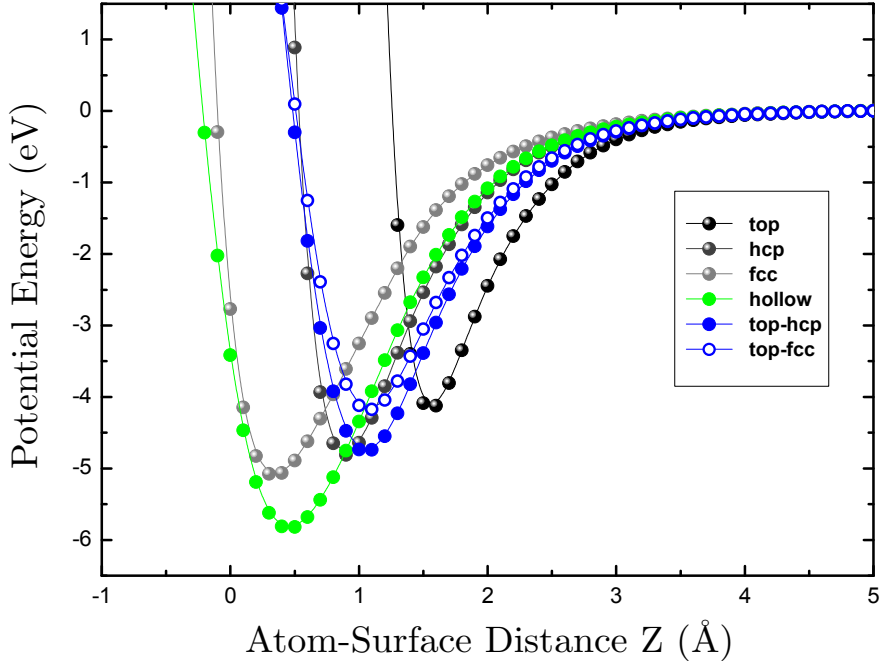


Figure 5.2: Dependence of the ab-initio potential energy for the system N/Fe(111) on the distance of the atom from the surface Z , for fixed X and Y .

three-dimensional (3D) Potential Energy Surface (PES) can be constructed from our 3D grid of ab-initio energies by exploiting the symmetry properties of the surface and interpolating over the energy grid by means of the corrugation reducing procedure (CRP) [77], as in Eq. 3.2. Details of the construction of a 3D-PES by using the CRP interpolation method have been presented in Sec. 3.1.

In order to test the accuracy of the CRP interpolation method for the N/Fe(111) system, we perform additional electronic structure calculations for different atomic locations at the Fe(111) surface that are not included in the CRP construction procedure. We compare these DFT results with the interpolated energy values. Figure 5.3 shows an example of the accuracy when interpolating over the surface cartesian coordinates (X , and Y). In Fig. 5.3, the symbols indicate the DFT calculations, while the lines refer to the CRP interpolation results. For the construction of the 3D atomic PES, the CRP interpolation method proves to have a high accuracy.

In Fig. 5.4 we show a contour plot representing a two dimensional (2D) cut of the 3D-PES for the system N/Fe(111). The 2D cut corresponds to a distance of the N atom of $Z = 0.5 \text{ \AA}$ above the surface. Figure 5.4 shows regions of higher energy (weaker

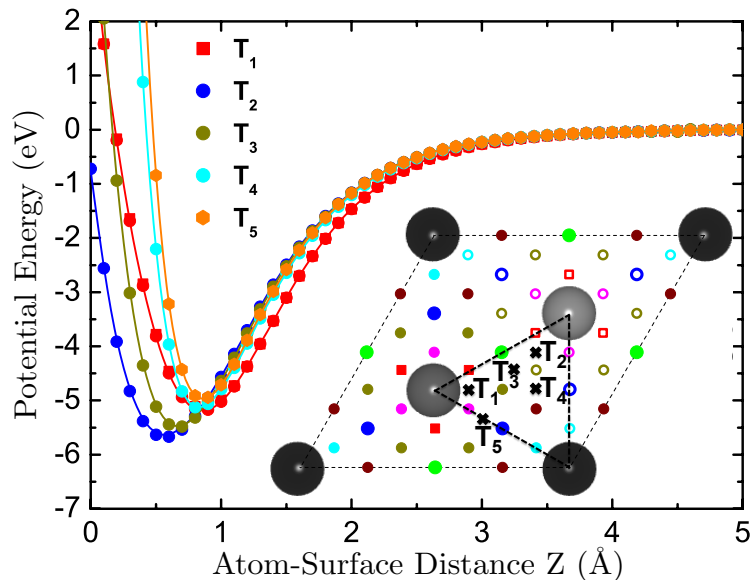


Figure 5.3: Dependence of the potential energy for the system N/Fe(111) on the distance Z of the atom from the surface, for fixed values of X and Y . The positions considered are shown in the inset. The points are DFT calculations. The lines correspond to the CRP numerical interpolation.

Coulomb attraction) due to the close interaction with the first and second layer atoms, illustrated by the blue color. The red color shows the preferred adsorption sites for the atomic nitrogen (*hollow* sites, with calculated adsorption energy $E_{ads} \approx -5.82$ eV, as mentioned above). Figure 5.5 shows a schematic representation of the top and side views for the final adsorption state (β -state) of the nitrogen atom into the *hollow* site of the unit cell. There are three equivalent *hollow* points in the same unit cell. In a simplified picture of the diffusion of N from one *hollow* site towards another adjacent one, there are two different energy paths that can be previewed. Which of them will have higher rate depends, among other features, on the different energy barriers, that were estimated to be 0.71 and 0.88 eV in Ref. [134].

5.3 N₂/Fe(111) Potential Energy Surface

Now we turn our attention to the investigation of the interaction between N₂ and the clean Fe(111) surface. We start with the illustration of the system coordinates used to perform DFT calculations. Based on the the DFT grid of energy points we will discuss

5. POTENTIAL ENERGY SURFACES OF NITROGEN ON IRON

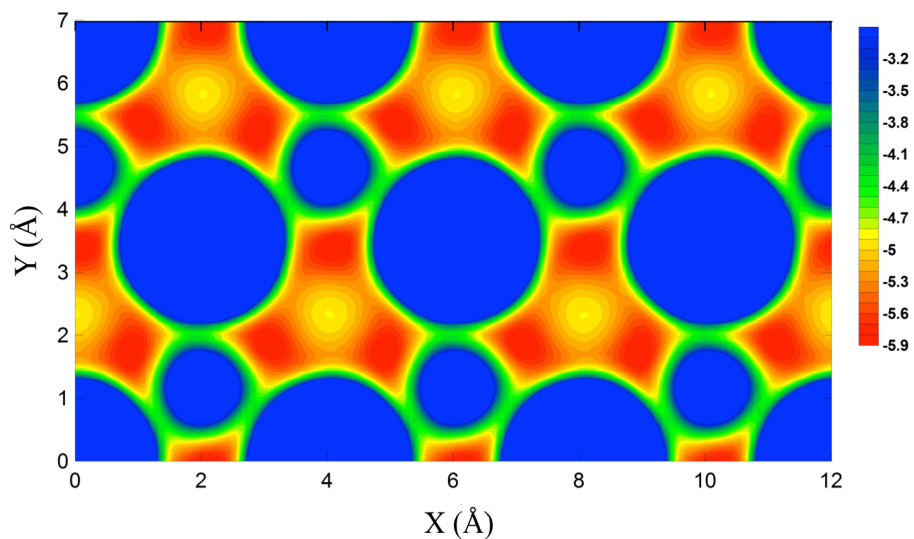


Figure 5.4: Contour plot representing a 2D cut of the three-dimensional potential energy surface (3D-PES) for the system N/Fe(111) with fixed $Z = 0.5 \text{ \AA}$.

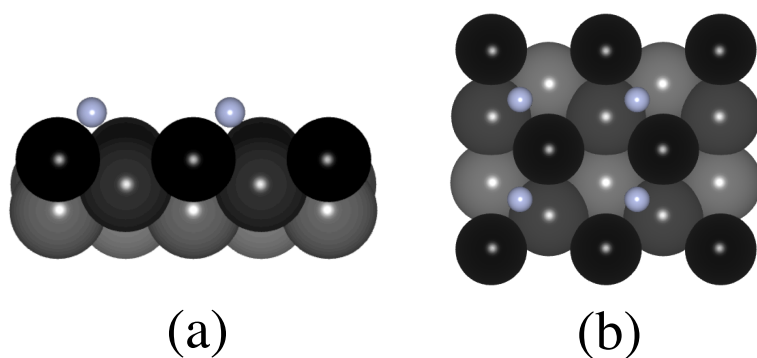


Figure 5.5: Schematic representation of (a) top and (b) side views of the nitrogen atom adsorption on the *hollow* side of the unit cell, at $Z = 0.5 \text{ \AA}$.

the data interpolation by using the CRP. We will also show the accuracy tests for the CRP as compared to DFT calculations. Finally, we will present the static analysis arising from the 6D-PES, which includes the prediction of the possible adsorption states for the N₂/Fe(111) system.

5.3.1 System Geometry

The interaction energy of the N₂ molecule with the Fe(111) surface is described with a 6D-PES that depends on the molecular center of mass position $R_{\text{CM}} = (X_{\text{CM}}, Y_{\text{CM}}, Z_{\text{CM}})$ and the internal coordinates (r, θ, ϕ) , which respectively stand for the internuclear N-N distance, the polar angle of the molecular axis relative to the surface normal, and the azimuthal angle, on the surface plane and relative to the X-axis (shown in Fig. 5.6.b). The PES is constructed from a grid of ab-initio energies, built out of 51 equidistant Z_{CM} positions in the range $0 \text{ \AA} \leq Z_{\text{CM}} \leq 5 \text{ \AA}$ ($Z = 0 \text{ \AA}$ is the topmost surface plane), 10 non-equidistant interatomic distances in the $0.7125 \text{ \AA} \leq r \leq 2.125 \text{ \AA}$ range, and 42 $(X_{\text{CM}}, Y_{\text{CM}}, \theta, \text{ and } \phi)$ configurations chosen following symmetry arguments. Thus, a total amount of 21420 DFT calculations were performed.

The Fe(111) surface geometry is illustrated in Fig. 5.6.a. *Top*, *hcp* and *fcc* sites correspond respectively to Fe atoms at the first, second and third plane, while *hollow*, *top-hcp*, and *top-fcc* sites are respectively located at mid-distance between adjacent *top* sites, between *top* and *hcp* sites, and between *top* and *fcc* sites. Before continuing to the angular grid it is important to observe that, for example, a molecule with a given $\theta - \phi$ orientation does not necessarily find equivalent environments when positioned on different *hollow* sites. An additional $+120^\circ$ or -120° rotation may be required. This is also the case for *top-hcp* and *top-fcc* sites. Therefore it is important, for each *XY*-site, to define a reference position on which ϕ values are defined. These reference $(X_{\text{CM}}, Y_{\text{CM}})$ positions are

- (i) *top*: $(0,0)$
- (ii) *hcp*: $(a\frac{\sqrt{2}}{2}, a\frac{1}{\sqrt{6}})$
- (iii) *fcc*: $(a\sqrt{2}, a\frac{2}{\sqrt{6}})$
- (iv) *hollow*: $(a\frac{\sqrt{2}}{2}, 0)$

5. POTENTIAL ENERGY SURFACES OF NITROGEN ON IRON

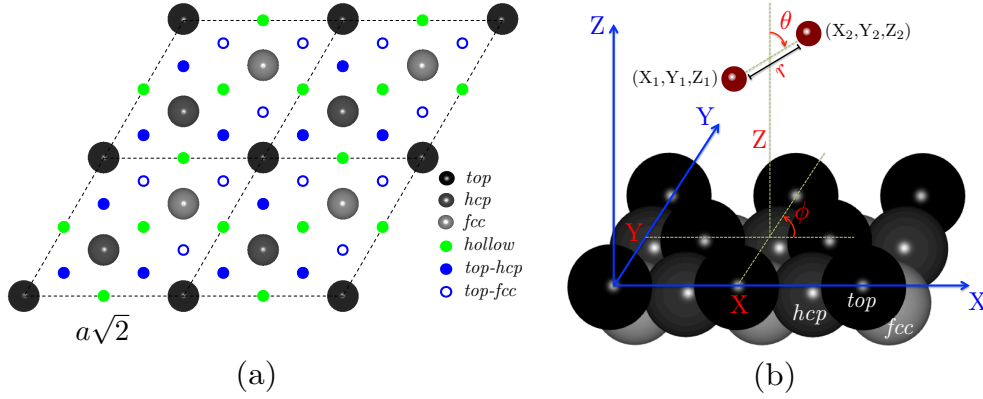


Figure 5.6: (a) Top view of the 2×2 unit cell of Fe(111) and (b) representation of the coordinates system used to describe the $\text{N}_2/\text{Fe}(111)$ interaction.

(v) *top-hcp*: $(a\frac{\sqrt{2}}{2}, a\frac{2}{\sqrt{6}})$

(vi) *top-fcc*: $(a\sqrt{2}, a\frac{1}{\sqrt{6}})$

with a the lattice constant defined in Fig. 5.6.a.

Regarding the 2D angular grid, it is made of

- **Vertical $\theta = 0^\circ$ configurations** for all six XY -sites.
- **Horizontal $\theta = 90^\circ$ configurations** with azimuthal orientations $\phi = 0^\circ - 90^\circ$ with equivalent periodic symmetry of 60° (i.e. 0° is equivalent to 60° and 90° equal to 30°) for *top*, *hcp* and *fcc* sites, and $\phi = 0^\circ - 30^\circ - 60^\circ - 90^\circ$ for *hollow*, *top-hcp* and *top-fcc* sites.
- **Tilted $\theta = 45^\circ$ configurations** with azimuthal orientations $\phi = 0^\circ - 30^\circ - 60^\circ$ for *top*, *hcp* and *fcc* sites, and $\phi = 0^\circ - 90^\circ - 270^\circ$ for *hollow*, *top-hcp* and *top-fcc* sites.

In order to test the accuracy of the CRP interpolation method over the six-degrees of freedom of the $\text{N}_2/\text{Fe}(111)$ system, we perform electronic structure calculations for different molecule configurations that are not included in the CRP construction procedure and compare these DFT results with the interpolated energy values. Figure 5.7 shows an example of the accuracy when interpolating over the molecular cartesian coordinates (Z , X , and Y). The left panel in Fig. 5.7 shows the dependence of the potential energy on the vertical distance from the surface, Z , for the equilibrium internuclear

5.3 N₂/Fe(111) Potential Energy Surface

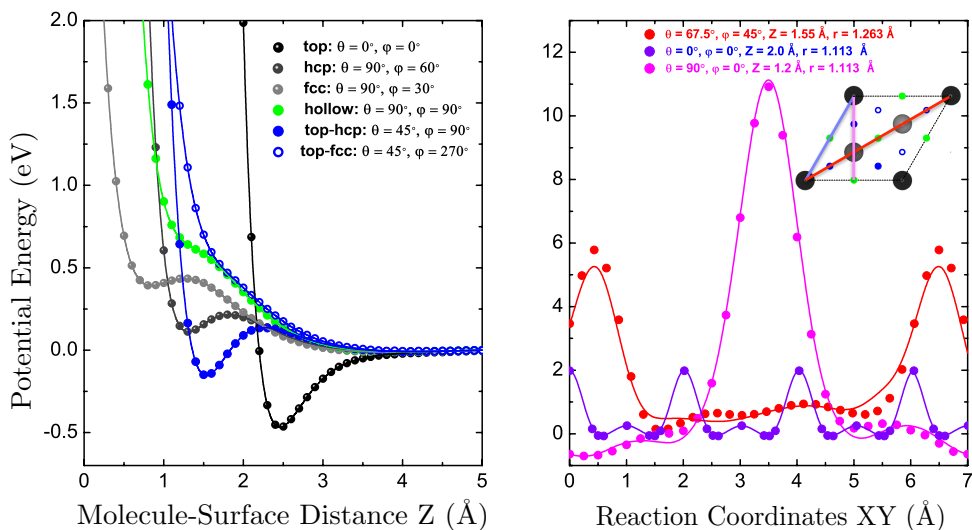


Figure 5.7: Comparison between the interpolated (solid lines) and DFT (symbols) energy values for N₂/Fe(111). The left side illustrates the dependence of the energy on the distance of the molecular center of mass from the surface Z , for fixed values of X, Y, θ , and ϕ (shown in the legend). The internuclear distance is set at the equilibrium distance $r_{eq} = 1.1125$ Å. The right side shows the dependence of the potential energy on the surface (X, Y) coordinates along different paths, as illustrated in the inset of the Figure for various Z, r, θ and ϕ values.

distance in the gas-phase (r_{eq}), and for different molecular configurations that have been included in the interpolation procedure. In the right panel of Fig. 5.7, we present a test of the interpolation over the surface coordinates X and Y , for various values of the remaining coordinates Z, r, θ , and ϕ . Another example of the accuracy obtained in the interpolation procedure for the polar angle θ and the azimuthal angle ϕ is shown in the left and right sides of Fig. 5.8, respectively. The DFT data shown in Fig. 5.8 are again, out of the grid used to build the 6D-PES. The internuclear distance is fixed to the equilibrium distance in the gas-phase (namely, $r_{eq} = 1.1125$ Å in our calculations). Results are shown for several high symmetry sites. In general, at distances relatively far from the surface, our interpolated values compare well with the ab-initio calculations. Nevertheless, due to the large increase in the corrugation at distances close to the surface, some errors in the interpolation do exist. Fortunately, for the configurations of relevance for the adsorption dynamics, the errors are well controlled and lower than 100 meV in most cases.

5. POTENTIAL ENERGY SURFACES OF NITROGEN ON IRON

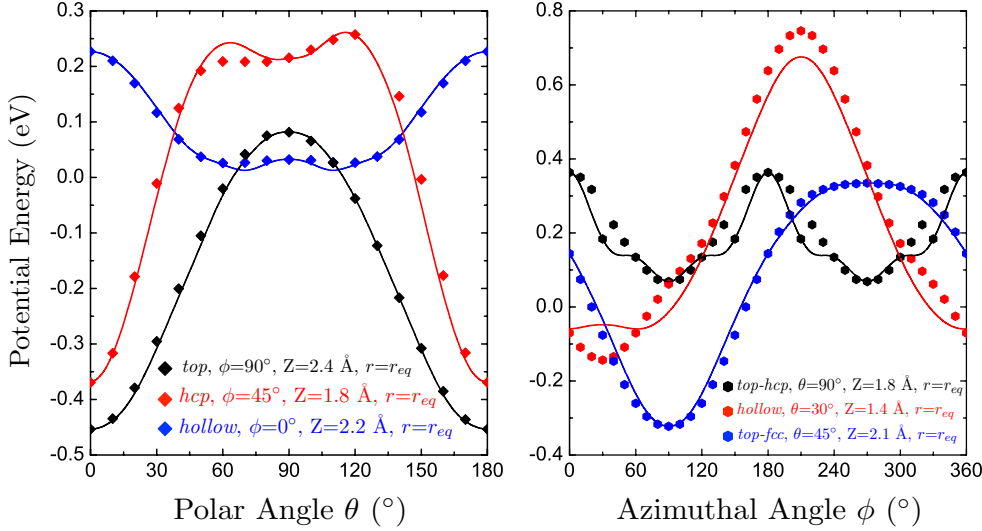


Figure 5.8: Comparison between the interpolated (solid lines) and DFT (symbols) energy values, for fixed X, Y, Z and equilibrium internuclear distance $r_{eq} = 1.1125 \text{ \AA}$. The left side illustrates the dependence on the polar angle θ , while the left side shows the dependence on the azimuthal angle ϕ .

5.3.2 Potential Energy Surface Properties

Let us discuss in this section the interaction of a nitrogen molecule with a clean Fe(111) surface from a purely static point of view. First, let us present the DFT results for the energy of the $\text{N}_2/\text{Fe}(111)$ system. We start with results obtained for nitrogen molecules at the equilibrium distance in the gas-phase, namely r_{eq} [128]. Later on, we will show results in which the N_2 six degrees of freedom are considered. DFT results will be shown for different molecular positions and orientations.

Figure 5.9 illustrates the interaction energy of N_2 on Fe(111) as a function of the distance between the molecular center of mass and the surface Z . The reference energy is taken to be that of the N_2 molecule at 5 \AA from the surface and at the equilibrium bond length. Most of the configurations in the plot correspond to the molecule oriented perpendicular to the surface ($\theta = 0^\circ$). The high-symmetry sites considered are those of Fig. 5.6. An additional configuration of the molecule is shown, with an orientation parallel to the surface ($\theta = 90^\circ, \phi = 0^\circ$). From Fig. 5.9 we can conclude that there are at least three possible molecular adsorption states. Two of them, on ‘top’ and ‘hcp’ positions, correspond to molecules with orientation perpendicular to the surface. The third one, with a lower binding energy, corresponds to a molecule on ‘hollow’ site with

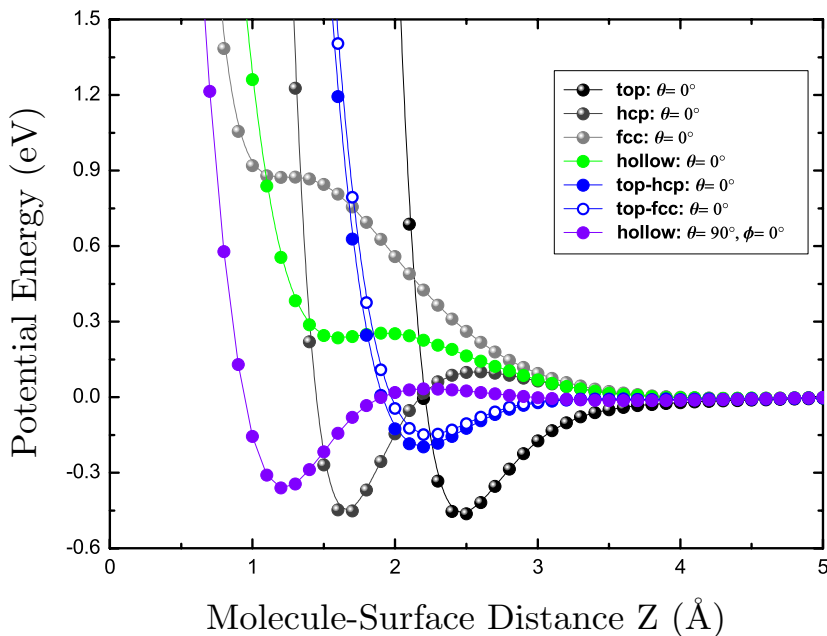


Figure 5.9: Dependence of the ab-initio potential energy for N₂/Fe(111) on the distance of the molecular center of mass from the surface Z for fixed X, Y, θ and ϕ . In all the cases the internuclear distance is also fixed to the equilibrium bond length in the gas-phase, $r_{eq} = 1.1125 \text{ \AA}$.

its axis parallel to the surface. We discuss them in further detail in the next paragraph.

Our extension of the analysis to internuclear distances other than the equilibrium one yields new possible adsorption states, with stretched internuclear distance. Figure 5.10 illustrates the interaction between the N₂ molecule and the Fe(111) surface as a function of the perpendicular molecule-surface distance Z . The reference energy, again, is taken to be that of the N₂ molecule at 5 Å from the surface and at the equilibrium bond length ($r_{eq} = 1.1125 \text{ \AA}$). All in all, our DFT calculations show four possible adsorption states for N₂ on the Fe(111) surface. On one hand, there are two molecular adsorption states with the molecular axis perpendicular to the surface plane and with internuclear distance equal to the equilibrium distance in the gas-phase, r_{eq} , on top of the first (*‘top’* site) and second (*‘hcp’* site) layer atoms. These states are usually called the γ - and δ -state, respectively. Molecules adsorbed into the γ -state (black symbols) are associated with an adsorption energy well of $E_{ads} \approx 0.46 \text{ eV}$, at $Z \approx 2.5 \text{ \AA}$ from the surface. Molecular adsorption into the γ -state is detected experimentally in all the previous

5. POTENTIAL ENERGY SURFACES OF NITROGEN ON IRON

studies [124, 125, 133, 135–138], as well as found theoretically in Refs.[134, 139–141]. The molecular nitrogen adsorption into the δ -state (dark-grey symbols) is characterized by an adsorption energy of $E_{ads} \approx 0.45$ eV, slightly weaker than the γ -state and with molecular center of mass distance to the surface of $Z \approx 1.7$ Å. Regarding the δ -state it is worth mentioning that the distance between the lowest N atom in the molecule and its Fe first neighbors (the three first layer Fe atoms around the molecule) is 1.88 Å, very close to the 1.94 Å value obtained for the γ -state. Likewise, the perpendicular N₂ center of mass distance to the second layer Fe atom right below the N₂ molecule is 2.46 Å, also close to the γ -state. The δ -state has been observed experimentally at low surface temperature and when the surface is saturated with γ -N₂ [125]. It was found to be less stable than the γ -state. Our findings for the γ and δ adsorption states, normal to the surface, are also consistent with previous theoretical work in this system [134]. Ref. [134], however, reports a slightly larger energy difference between the two states, the γ -state being about 0.14 eV deeper in energy than the δ -state. We find that both the γ and δ states have similar adsorption energies and the difference in the adsorption rate should be explained in terms of the energy barriers as well as of the dynamics of the process.

On the other hand, in Fig. 5.10, there are two other adsorption states, with molecular axis parallel to the surface plane ($\theta = 90^\circ$), and with stretched molecular bond length (r). The α -state, which is denoted by green symbols in Fig. 5.10, represents the deepest adsorption well of our DFT calculations. The adsorption energy is $E_{ads} \approx 0.64$ eV and the molecular center of mass is located at $Z = 1.2$ Å, on the *hollow* site and with an internuclear distance increased by about 0.1 Å ($r = 1.2$ Å). The α -state is well known experimentally [124, 125, 133, 135–138] and theoretically [134, 139]. Finally, the ε -state is an additional adsorption state found in our calculations, which has been reported before only in Refs.[134, 138, 139]. It is denoted by light-grey symbols in Fig. 5.10. Characterized by an adsorption energy of $E_{ads} \approx 0.45$ eV, the ε -state is identified close to the surface at $Z \approx 0.6$ Å, on top of the third (*fcc* site) layer atoms, with an internuclear distance increased from the equilibrium distance by about 0.2 Å ($r = 1.3$ Å). In the ε -state, the two N atoms in the molecule are oriented in the azimuthal plane in such a way that they avoid the strong repulsion due to the first layer atoms ($\phi = 60^\circ$) and are placed close to the atomic adsorption site (*hollow* site). Both the α - and the ε -states are potential candidates to be intermediate states for dissociative adsorption at

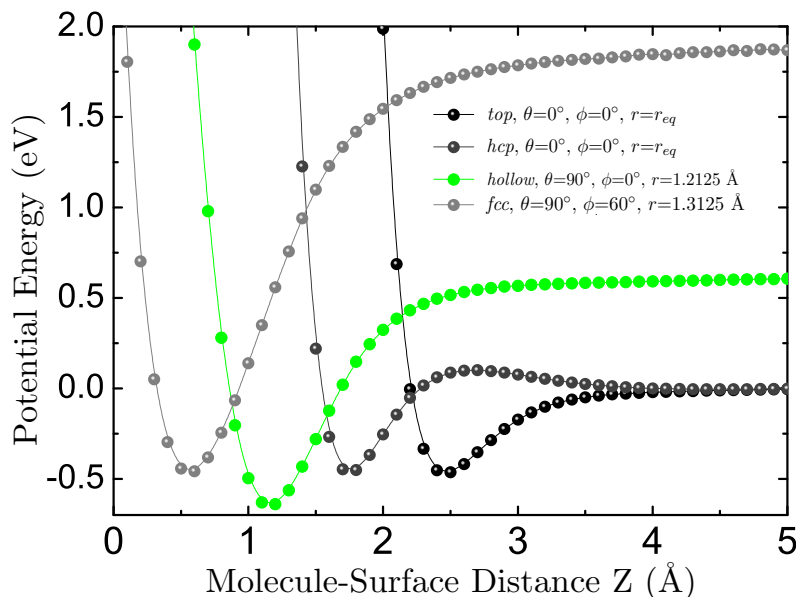


Figure 5.10: Representation of the four local minima for N₂/Fe(111) system. The figure shows the dependence of the ab-initio potential energy on the distance of the molecular center of mass from the surface Z for fixed X, Y, r, θ , and ϕ . The values of r, θ , and ϕ are shown in the inset.

very low impact energy. In Fig. 5.11, a selection of two-dimensional (r, Z) cuts for the four local minima of the 6D-PES, as identified before, are introduced. The molecular orientation and the surface coordinates are shown in the inset of each contour plot. An energy scale ranging from -0.7 eV (red color) to 2.5 eV (blue color) is used to show the different attractive and repulsive regions of the potential for each elbow plot, with the zero energy value indicated by dashed lines. The upper panel in Fig. 5.11 represents the adsorption states γ and δ , for which the molecules are adsorbed vertically on top of the first and second layer atoms of the surface, respectively. The lower panel shows the adsorption states α and ε , for which the molecules are adsorbed parallel to the surface. Except the molecular adsorption path toward the γ -state, Fig. 5.11 shows an entrance barrier into all other adsorption states, namely δ (≈ 200 meV), α (≈ 100 meV), and ε (≈ 400 meV). Figure 5.11 corresponds, however, to two-dimensional contour plots, i.e., to molecules that are forced to reach a particular site with fixed configuration. Due to the interaction with the surface, the initial configurations of the molecule may be changed continuously through the molecule dynamical pathway for adsorption. Therefore, a conclusion based only on the static analysis of the PES for

5. POTENTIAL ENERGY SURFACES OF NITROGEN ON IRON

different but fixed configurations can be misleading [28, 142, 143]. The four local N_2 molecularly adsorption (γ , δ , α , and ε) states and the atomic preferred atomic (β) state, on top of the Fe(111) surface, are schematically illustrated in Fig. 5.12.

5.4 Summary

We have presented a large set of ab-initio density functional theory calculations for N and N_2 at Fe(111) systems. We first study the interaction of nitrogen atoms with a clean Fe(111) surface. The results show that the only possible adsorption site is the hollow site. We numerically interpolate our DFT data using the corrugation reducing procedure method and build a three-dimensional potential energy surface.

Furthermore, we have investigated the interaction of N_2 with clean Fe(111) surfaces. First we performed ab-initio DFT, taking into account the six-degrees of freedom (X, Y, Z, r, θ, ϕ) of the molecular system. The CRP is used as a numerical interpolation method of the DFT data. The interpolation of the 6D-PES shows a high accuracy. Four local adsorption minima have been obtained from our DFT calculations. Two adsorption states with the molecule perpendicularly oriented to the surface plane and on top of the first and the second layer atoms have been found. Two additional states are reported, with the molecular axis oriented parallel to the surface plane, with a stretched bond length, and with the molecule located on the *hollow* site and on top of the third layer atoms.

The study of the dynamics of the non-dissociative and dissociative molecular adsorption processes requires a complete description of the energy landscape as well as a detailed analysis of the possible reaction paths and rates. The dynamics of several reaction processes will be introduced in the next chapters.

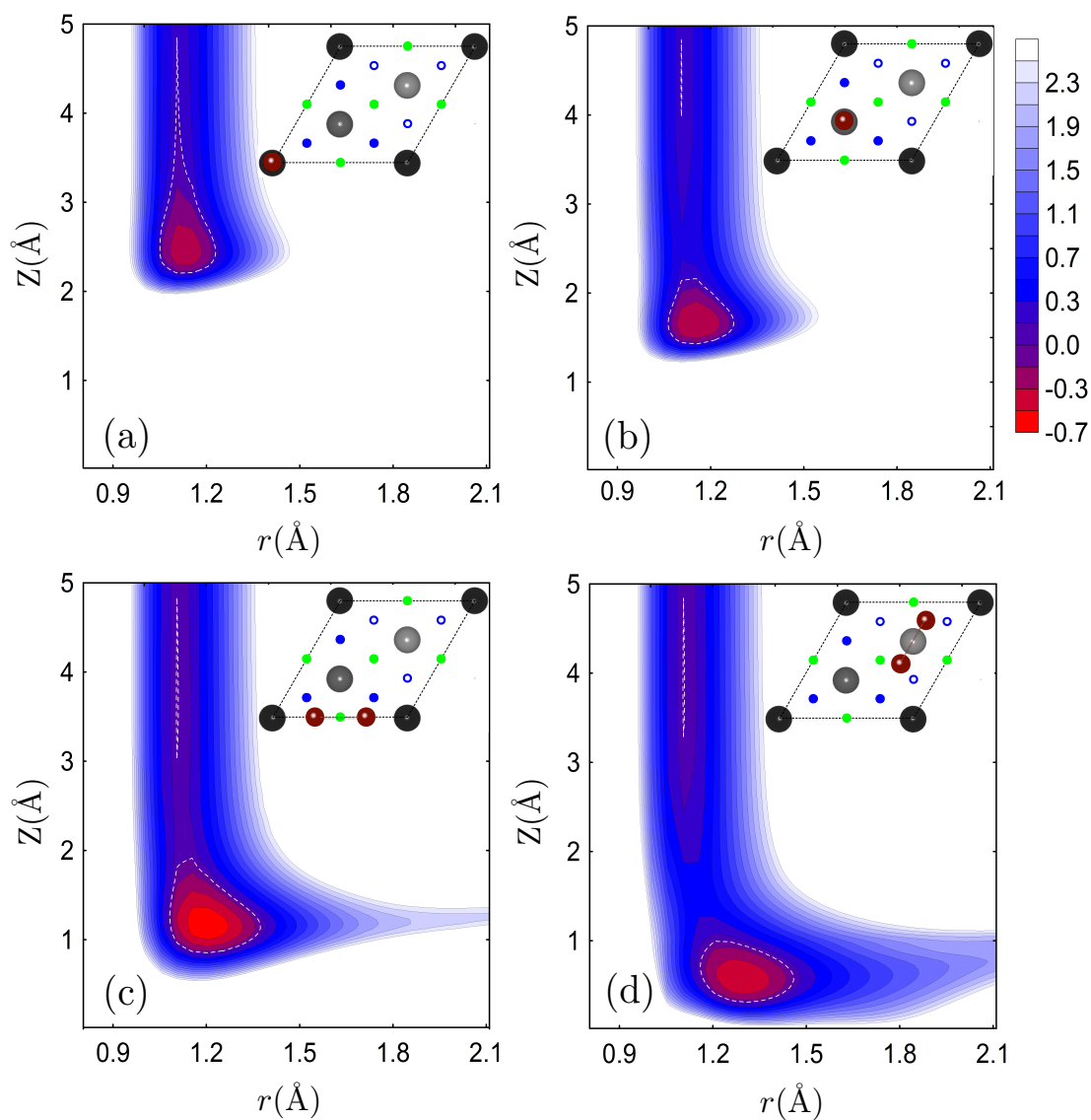


Figure 5.11: Contour plots for interpolated 2D (r, Z) cuts of the possible adsorption states (γ , δ , α , and ε). The molecular orientation and position over the unit cell is depicted in each contour plot. The energy scale on the right side is given in eV, ranging from -0.7 eV (red) to 2.5 eV (blue). The white regions show potential energy values higher than 2.5 eV. The dashed white lines correspond to the zero potential energy values.

5. POTENTIAL ENERGY SURFACES OF NITROGEN ON IRON

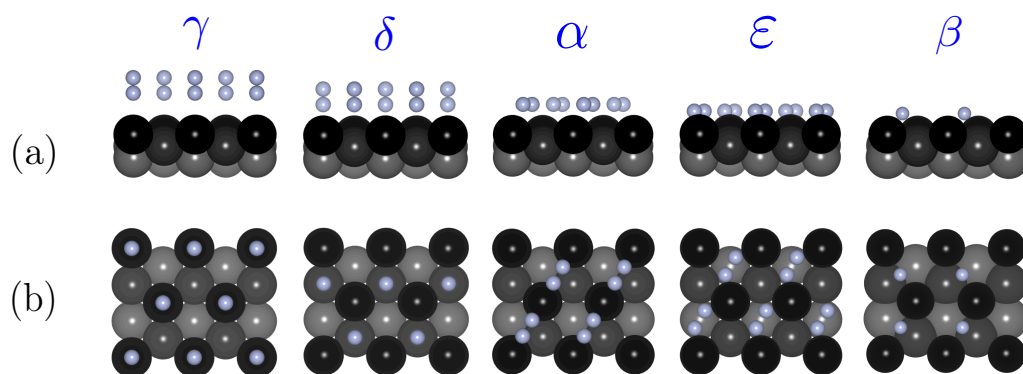


Figure 5.12: (a) Top view and (b) side view of the five nitrogen adsorption states on a clean Fe(111) surface. From left to the right, the molecular adsorption states γ , δ , α , and ϵ , and the atomically adsorption state called β .

6

Adsorption Dynamics of Molecular Nitrogen at a Fe(111) Surface

In the previous chapter, we have identified four molecular adsorption states (γ , δ , α , and ε) states, plus the atomic adsorption β -state. However, the identification of these states is set for molecules forced to approach the surface in a particular configuration. The interaction of the molecule with the surface results in a continuous variation of the initial configuration of the molecule through the molecule dynamical pathway for adsorption. Therefore, a study of the relevance of the different adsorption states based only on the static analysis of the PES can be misleading [28, 142, 143]. Hence, in this chapter we present a detailed study of the dynamics of the adsorption process using the DFT-based potential energy surface that we have presented in the previous chapter. In the literature, there are no full-dynamical studies for the adsorption dynamics of N_2 on the Fe(111) surface, in spite of this being the most reactive face. The general purpose of this chapter is to fill, at least partially, this gap.

Existing measurements provide a general picture of the nitrogen adsorption dynamical process on Fe(111). For a wide range of substrate temperatures and for thermal energies of the incoming N_2 molecules, two molecular adsorption states have been identified, namely, a weakly bound state $\gamma\text{-N}_2$, with the molecular axis perpendicular to the surface plane, and a more strongly bound adsorption state $\alpha\text{-N}_2$, with stretched internuclear distance, with the molecule adsorbed on the *hollow* site and parallel to

6. ADSORPTION DYNAMICS OF MOLECULAR NITROGEN AT A FE(111) SURFACE

the surface plane [124, 125, 133, 135–138]. At low surface temperatures and when the surface is already saturated with γ -N₂, an additional adsorption state, δ -N₂, has been observed with the molecule on top of a second layer atom and perpendicular to the surface [125]. Available theoretical studies predict similar adsorption states, in agreement with the experimental measurements [134].

This chapter is arranged as follows: Sec. 6.1 describes the computational details of the methods that have been used to perform classical trajectory calculations. In Sec. 6.2, the results for the dynamical study of the molecular adsorption of N₂ on Fe(111) are presented. Conclusions extracted from our results will be included in Sec. 6.3.

6.1 Quasi-Classical Trajectory Calculations

Quasi-classical trajectory (QCT) calculations are performed on the continuous 6D-PES, in order to study the N₂ molecular adsorption dynamics on the clean Fe(111) surface. We include the initial zero point energy (ZPE) of the molecule in the calculations and set it to be $ZPE = 142$ meV. The path for all trajectories starts with the molecule at its internuclear equilibrium distance in the gas-phase ($r_{eq} = 1.1125$ Å) and with an initial distance from the surface of $Z_{cm} = 5.0$ Å. For such initial conditions, the 6D-PES values are zero. A conventional Monte Carlo procedure is used for sampling the initial molecular coordinates (X, Y) and the molecular orientation (θ and ϕ). For surface motion, the generalized Langevin oscillator (GLO) [101–103] model is applied to include temperature effects. The GLO model has been explained in 3.2. In this model, the surface motion is represented in terms of a three-dimensional harmonic oscillator. In order to consider the coupling and energy-exchange of the surface with the bulk, an additional three-dimensional ghost oscillator is coupled to the surface oscillator. The latter is subjected to friction and random forces related to each other through the second fluctuation-dissipation theorem. The ghost particles allow us to represent the bulk of the solid as a thermal bath at the chosen temperature [144]. In our calculations, we distinguish among three different events:

- **Reflection**, when the molecule center of mass reaches for a second time the initial starting distance of 5.0 Å, with positive velocity pointing towards the vacuum;

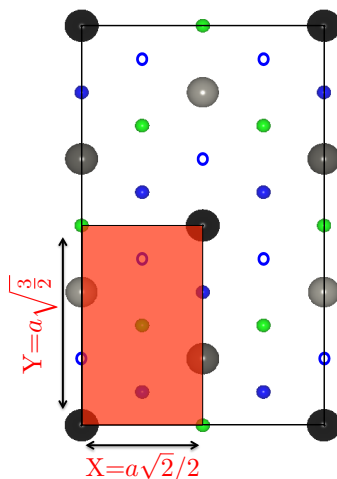


Figure 6.1: Representation of the Fe(111) surface used in the quasi-classical trajectory calculations. Shaded area illustrates the sampling area of initial (X, Y) positions, where ‘ $a = 2.855 \text{ \AA}$ ’ is the lattice parameter.

- **Dissociation**, when the molecule bond length reaches the value of $r_{diss} = 2.1125 \text{ \AA}$;
- **Molecular trapping**, when the molecule is neither reflected nor dissociated after 10 ps.

The calculations are performed within a wide interval of initial kinetic energies for the molecule, ranging between 50 meV and 5.0 eV for normal incidence. For each value of the initial kinetic energy (E_i), a large number of trajectories (100 000) is used to obtain sufficiently good statistics, with a maximum trajectory integration time of 10 ps. The surface sampling area used for representing the initial impact (X, Y) positions on the surface is shown as the shaded area in Fig. 6.1.

6.2 Adsorption Dynamics

In the following we present the results for the six-dimensional quasi-classical trajectory calculations of the N_2 adsorption dynamics on the clean Fe(111) surface. Figure 6.2 shows the molecular adsorption probabilities as a function of the initial kinetic energy of the molecule. Results are shown for normal incidence and for surface temperature, T_s , varying from 0 to 520 K. The adsorption probability decreases with increasing T_s , in accordance with experimental observations [23, 133]. In fact, for the molecule to be

6. ADSORPTION DYNAMICS OF MOLECULAR NITROGEN AT A FE(111) SURFACE

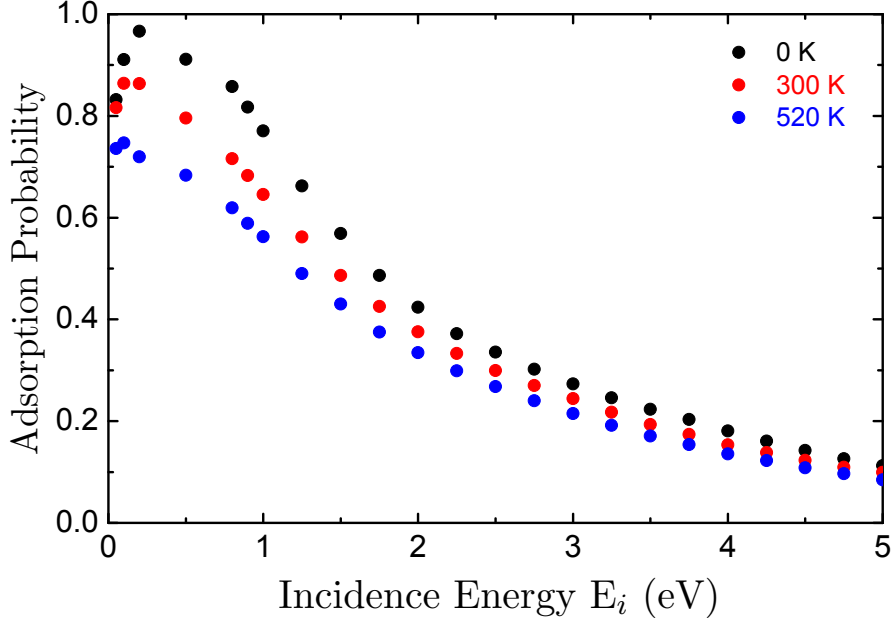


Figure 6.2: Molecular adsorption probability as a function of the molecular initial incidence energy, for surface temperatures 0, 300, and 520 K and normal incidence.

accommodated on the surface, it has to dissipate energy into the lattice. The energy difference between the incoming molecule and the substrate plays a crucial role in the adsorption process. In most of the energy range shown in Fig. 6.2, the molecules are hot compared to the surface (i.e. $E_i > k_B T_s$). As T_s increases, less energy is usually dissipated into the lattice in average, and, consequently, the possibility of trapping into the adsorption well is decreased [103]. If we focus on the dependence on the initial molecular kinetic energy, E_i , the adsorption probability tends to increase with decreasing E_i . Later in this section we will show that the reason for that is the increasing contribution of different adsorption channels. However, due to the complex energy landscape for some particular configurations, the adsorption probability starts to decrease when decreasing E_i below 200 meV.

Focusing on the low energy regime for N_2 adsorption on Fe(111) with $T_s = 300$ K, Fig. 6.3 shows the final (XY) adsorption sites, orientations, heights, and internuclear distances of the adsorbed molecules, for normal incidence and low initial kinetic energies, $E_i = 50$ meV (Fig. 6.3.a) and 200 meV (Fig. 6.3.b). From the right panel of Fig. 6.3.a, we can notice that most of the molecules are adsorbed close to the first layer

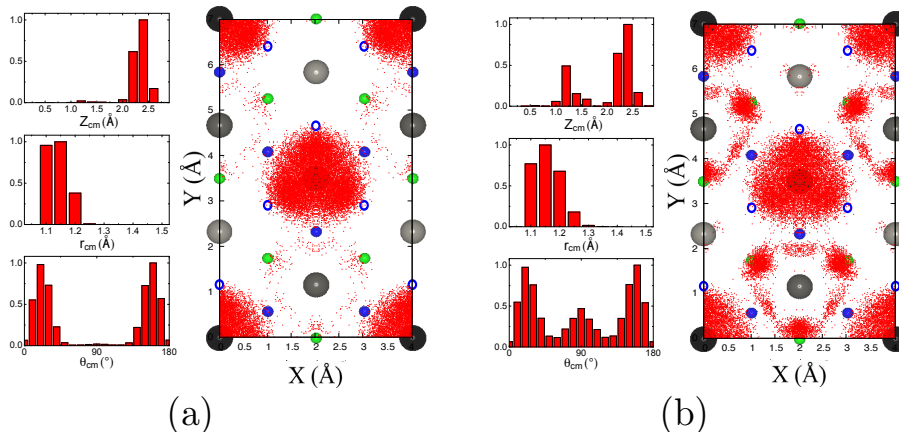


Figure 6.3: Representation of the final adsorption states with $T_s = 300$ K, for (a) $E_i = 50$ meV, with total molecular adsorption probability is $P=0.81$ (b) $E_i = 200$ meV, with $P=0.86$. The final XY positions of the adsorbed molecules are represented in the right panel. The left panel shows the distribution of heights (Z), internuclear distances (r), and polar angles (θ) for the adsorbed molecules.

atoms. However, for $E_i = 200$ meV in Fig. 6.3.b there are some molecules that are able to reach the *hollow* site of the unit cell. Few molecules are finally adsorbed close to the third layer atoms (*fcc* site). The difference in the adsorption probability as well as in the adsorption sites between the two initial incidence energies 50 and 200 meV, is related to the different energy barriers that the molecules have to overcome in order to be finally adsorbed in one or another of the adsorption states.

Details of the adsorption dynamics process for N_2 on Fe(111) with $T_s = 300$ K, are shown in Figs. 6.4 and 6.5, for normal incidence and low initial kinetic energies, $E_i = 50$ and 200 meV. Snapshots of the molecular center of mass coordinates on the surface plane, as well as of the orientation of the adsorbed molecules for various Z values, are represented in the figures. Only those trajectories that correspond to molecules eventually adsorbed are shown. For $E_i = 50$ meV (Fig. 6.4), all adsorbed molecules are spread over the unit cell at $Z=2.6$ Å. For lower distances to the surface, all trajectories tend to change their direction and the molecules feel a strong attraction to the first layer atoms at $Z=2.2$ Å. On their way further toward the surface, more than 40 % of the molecules are attracted to the adsorption well of the first layer atoms, i.e., the γ -state. Repulsion due in part to the interaction with the first layer atoms will force some molecules to escape toward other (X, Y) positions in the unit cell. However, the kinetic energy of

6. ADSORPTION DYNAMICS OF MOLECULAR NITROGEN AT A FE(111) SURFACE

most of these molecules is insufficient to overcome the barrier to approach further the surface. Therefore, only few trajectories can approach as close as $Z = 1.8 \text{ \AA}$ from the surface and most of them have an orientation parallel to the surface. This dynamical evolution can explain the final position of the adsorbed molecules (Fig. 6.3.a): the majority of the molecules are adsorbed on the *top* site of the first layer atoms and very few molecules are finally adsorbed on the *hollow* site. This conclusion is consistent with the histograms in the left panel of the lower graph, where most of the trajectories will be adsorbed above 2.0 \AA from the surface, with molecular orientations close to the perpendicular adsorption state and with internuclear distances similar to that of the γ -state. These results reflect also the fact that there is no barrier for the molecules to reach the adsorption well of the first layer atoms from the gas-phase, which agrees with the experimental studies [133, 135, 138].

Figure 6.2 shows that the maximum value of the adsorption probability is found at $E_i = 200 \text{ meV}$, for which the molecules can reach deeper positions toward the surface and have access to potential wells other than the γ -state. Similarly as in Fig. 6.4, we follow the dynamics of the adsorption molecules with an initial kinetic energy of $E_i = 200 \text{ meV}$ in Fig. 6.5. In this case, approximately 17 % of the molecules fall in the adsorption well of the *top* site (γ -state) before reaching $Z \approx 2.0 \text{ \AA}$. Most of the remaining trajectories start to point toward the *hollow* site of the unit cell. In addition, the number of trajectories is roughly preserved from $Z \approx 1.6 \text{ \AA}$ up to $Z \approx 1.2 \text{ \AA}$. Further movement toward the surface is restricted by a large potential barrier, and only few molecules can reach distances below 1.0 \AA . The positions of the center of mass for these molecules will be located on top of the third layer atoms, the *fcc* site of the unit cell, and they will be oriented parallel to the surface. In addition, we can notice the difference between the final adsorption states for the two initial incidence kinetic energies. In the right panel of Fig. 6.3.b, there are more adsorbed molecules in the so-called α -state, and even a few number of trajectories will end up adsorbed into the ε -state. Comparison between Fig. 6.4 and Fig. 6.5 shows that the molecules cross through the γ -state before being adsorbed into the α -state. Indeed, there is a separation barrier of 200 meV between γ and α states. A similar conclusion was derived from previous experimental studies [135–138].

Figure 6.6 shows the variation of the $\text{N}_2/\text{Fe}(111)$ relative adsorption probability into *top*, *hcp*, *fcc* and *hollow* sites of the unit cell, corresponding to the possible adsorption

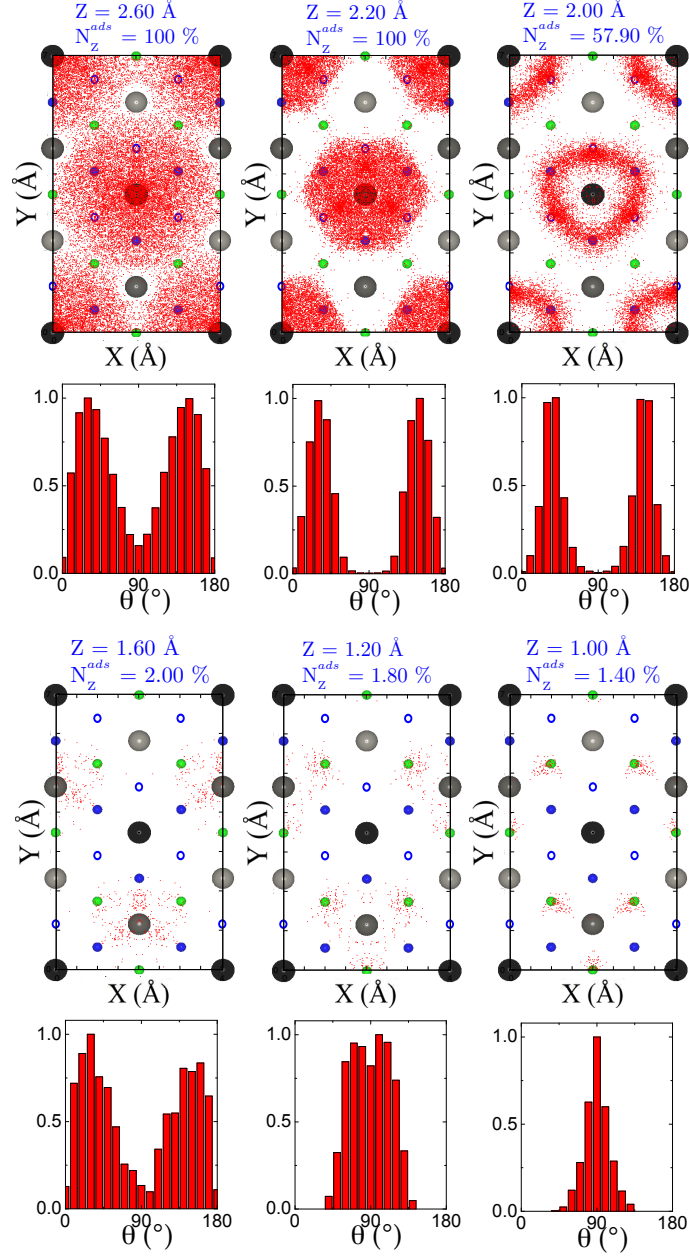


Figure 6.4: Evolution of the coordinates of the N_2 molecules that become eventually adsorbed. 100 000 trajectories, with initial impact energy $E_i = 50$ meV and with surface temperature $T_s = 300$ K, are considered. The upper panels illustrate the XY distribution of the center of mass for different values of the distance from the surface Z . Above each sampling area, the percentage of adsorbed molecules that reach this particular Z distance, N_z^{ads} , is written. The lower panels show the polar angle θ -distribution.

6. ADSORPTION DYNAMICS OF MOLECULAR NITROGEN AT A FE(111) SURFACE

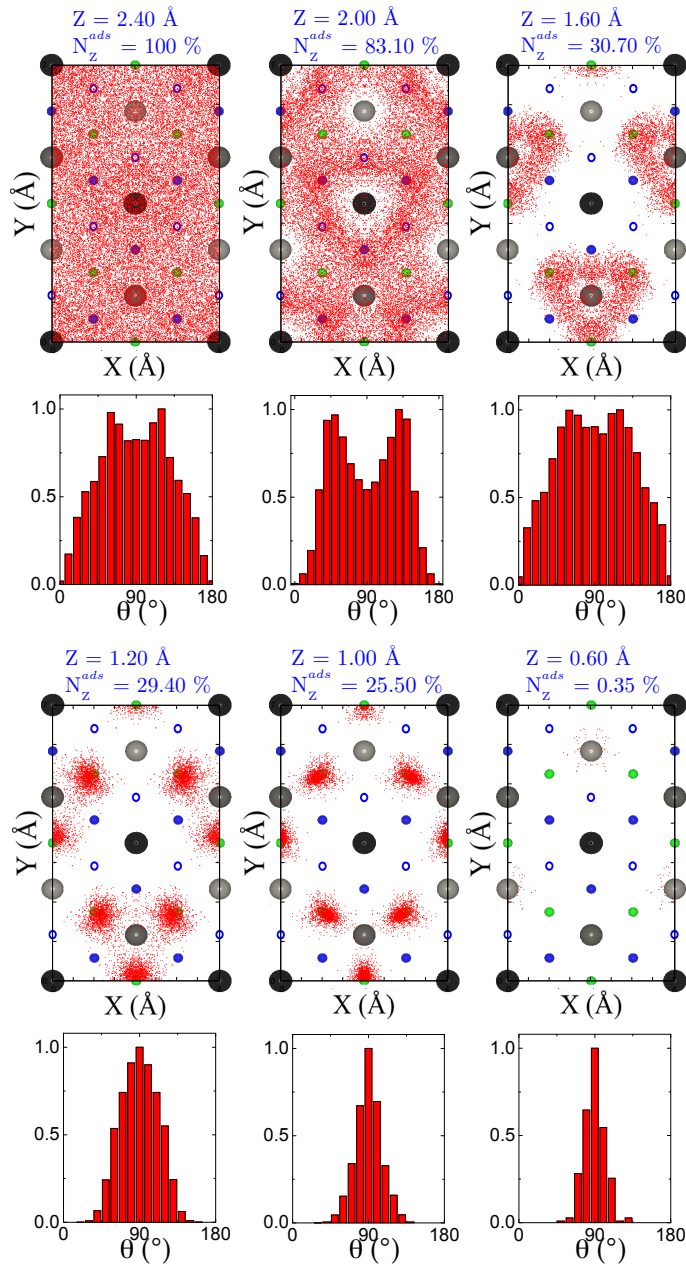


Figure 6.5: Same as Fig. 6.4 with an initial incidence energy $E_i = 200 \text{ meV}$.

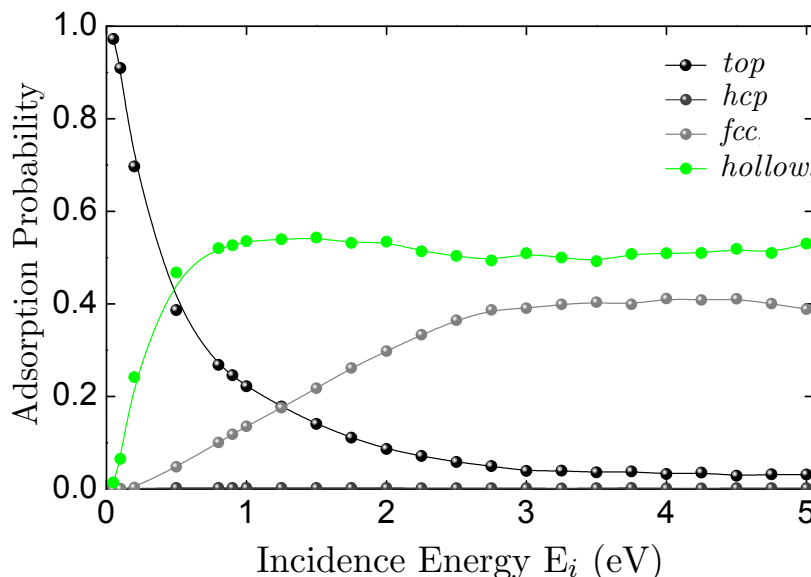


Figure 6.6: Relative molecular adsorption probability to *top*, *hcp*, *fcc* and *hollow* sites of the unit cell (γ , δ , ε , and α states, respectively) as a function of the initial incidence energy, E_i , of the molecule, with surface temperature $T_s = 300$ K.

states γ , δ , α , and ε , respectively, with the initial molecular incidence energy, at $T_s = 300$ K. At very low energy, in agreement with experimental observations [124, 133], adsorption into the γ -state has a relative adsorption probability close to one ($\sigma_\gamma \approx 1$). Adsorption into the α -state has a relative adsorption probability of $\sigma_\alpha \approx 10^{-2}$ for the same range of energies. As the initial molecular kinetic energy increases, a sharp decrease is observed for the adsorption into the γ -state, which eventually vanishes at high initial impact energy. Nevertheless, σ_α will increase with increasing molecule initial energy, until reaching a saturation value of $\sigma_\alpha \approx 0.55$ at $E_i = 0.8$ eV. The adsorption into the δ -state is negligible over the full energy range. Such behaviour was previously extracted from experiments and static DFT calculations in Ref [125, 134, 139]. According to the PES characteristics, direct adsorption into the ε -state is associated with an entrance barrier larger than roughly 400 meV. An increase in σ_ε with increasing initial molecular impact energy is therefore observed, starting at 500 meV until reaching a saturation value of $\sigma_\varepsilon \approx 0.40$ at $E_i = 2.25$ eV.

6. ADSORPTION DYNAMICS OF MOLECULAR NITROGEN AT A FE(111) SURFACE

6.3 Summary

We studied the molecular adsorption dynamics in a DFT-based 6D-PES by performing quasi-classical trajectory calculations. The QCT calculations were performed for a wide range of initial impact energies, and using different surface temperatures. The molecule adsorption probability in our results is quite dependent on the surface temperature as well as on the initial impact energy. At very low energy, details of the dynamics indicate no entrance barrier for the molecules to reach the surface. Most of the molecules will be adsorbed on top of the first layer atoms. However, the adsorption probability into the molecular states, which are parallel to the surface and that are associated with an activation barrier, will be much higher for increasing initial impact energy. Indeed, our QCT calculations confirm that there are activated and nonactivated paths for the approach of N_2 to the Fe(111) surface. Our results show good agreement with previous experimental studies of N_2 on Fe(111), help to understand the complex dynamics of the N_2 molecular adsorption on the Fe(111) surface, and pave the way to further analyze the dissociation dynamics in this system, which will be presented in the next chapter.

7

Dissociative Adsorption Dynamics of Nitrogen at a Fe(111) Surface

In this chapter we present our results for the dissociative adsorption dynamics of N_2 on a clean Fe(111) surface. Based on the 6D-PESs constructed in Chapter 5, we performed quasi-classical trajectory calculations in order to compute the initial sticking probability and to simulate the dissociation dynamics. The dissociation rate of N_2 molecules on iron surfaces depends on the Fe crystal orientation. For this reason, a comparison between the nitrogen reaction properties on Fe(111) and Fe(110) will be also presented. The scientific and technological interest behind the interaction of N_2 with the Fe(111) surface makes a good case for a detailed study of the dynamical processes associated with this system. Several experimental techniques in early works by Ertl *et al.* [124, 133] were used to study the nitrogen dissociation process. They reported a very small initial sticking coefficient for $N_2/Fe(111)$ at thermal energies ($S_0 \approx 10^{-7}$ - 10^{-6}). Grunze *et al.*, arrived to the same conclusion and suggested that the nitrogen dissociation proceeds via a precursor state [135]. All subsequent experimental observations [125, 136–138, 145] reached the same conclusion. Theoretically, Goikoetxea *et al.* presented the first full dynamical study of N_2 on the less reactive crystal face of iron, namely Fe(110) [128]. They performed the calculation on a 6D-PES. They reported the effect of surface temperature as well as that of the N_2 beam initial conditions on the dissociative sticking probability. Despite the higher reactivity of Fe(111) and to the best of our knowledge,

7. DISSOCIATIVE ADSORPTION DYNAMICS OF NITROGEN AT A FE(111) SURFACE

there are no full dynamical studies for the dissociation dynamics of N₂ on the Fe(111) surface.

The chapter is arranged as follows: Section 7.1 presents the adsorption molecular states that may relate to the indirect dissociation processes. In Sec. 7.2, we will present our results for the initial sticking probability as well as the details of the dynamical process. A comparison between the reaction characteristics of nitrogen on Fe(111) and Fe(110) is shown in Sec. 7.3. The conclusion and outlook will be included in Sec. 7.4.

7.1 Molecular Trapping

In the previous chapter, the N₂ molecular adsorption probability was shown to be highly dependent on the initial molecule impact energy, being much higher (close to 1) for low initial energies of the incoming molecule. Most of the molecules in this low energy regime are adsorbed into the γ -state. Surface temperature also affects the adsorption probability. For relatively high surface temperature (520 K), a large number of molecules were recorded as dynamically trapped after reaching the calculation time of 10 ps. When increasing the impact energy, molecules are able to overcome existing energy barriers and can reach the other parallel adsorption states (α and ε). Previous studies on the dissociation process of N₂ on Fe(111) discussed the dissociation process via a precursor state. The intermediate precursor state suggested was a molecule adsorbed parallel to the surface, with a geometry in which the two N atoms are strongly interacting with the surface. The characteristics of the adsorption into the α and ε -states are therefore important to understand the molecular dissociation. For this reason, we present in Fig. 7.1 the 2D (X, Y) contour plots of the surface energy landscape for the α (Fig. 7.1.a) and ε (Fig. 7.1.b) states.

7.2 Dissociative Dynamics of N₂ on Fe(111)

In the following we present our results for the QCT calculations of the N₂ dissociative adsorption dynamics on the clean Fe(111) surface. In Fig. 7.2, the initial sticking probability S_0 is shown as a function of the initial kinetic energy of the molecule, for a surface temperature of $T_s = 520$ K. Results are shown for normal ($\Theta_i = 0^\circ$) and

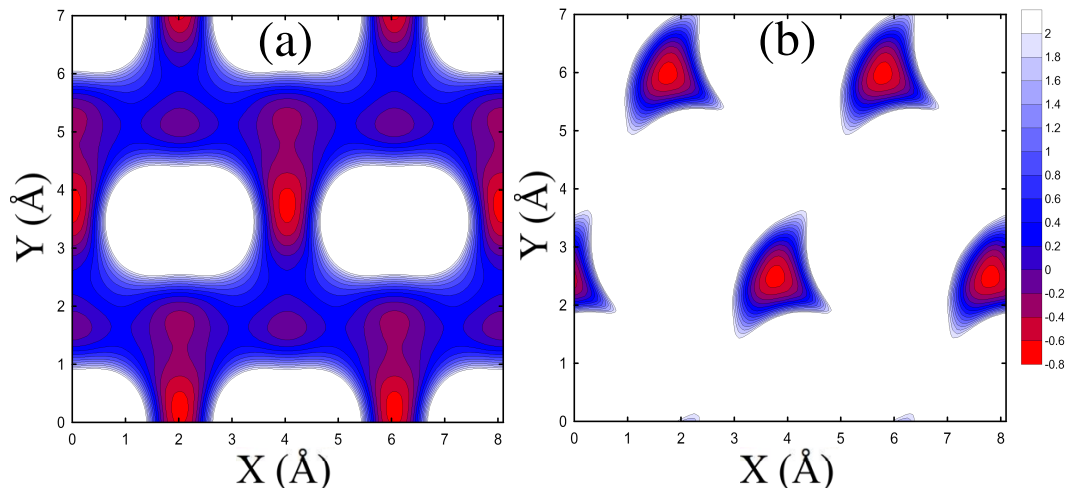


Figure 7.1: 2D contour plots for an interpolated surface energy landscape (X_{CM}, Y_{CM}) cut of the α and ε adsorption states. (a) α -state with $Z_{CM} = 1.2 \text{ \AA}$, $r = 1.213 \text{ \AA}$, $\theta = 90^\circ$ and $\phi = 0^\circ$. (b) ε -state with $Z_{CM} = 0.6 \text{ \AA}$, $r = 1.313 \text{ \AA}$, $\theta = 90^\circ$ and $\phi = 60^\circ$. The energy scale to the right is given in eV, ranging from -0.8 eV (red) to 2.0 eV (blue). The white regions show potential energy values higher than 2.0 eV . The contour lines are separated by an interval of 0.2 .

off-normal incidence angles ($\Theta_i = 30^\circ, 60^\circ$). In general, for the amount of trajectories considered, no dissociation events were found below $E_i = 800 \text{ meV}$. S_0 increases when increasing the molecule initial impact energy. In Fig. 7.2.a, the sticking probability is plotted as a function of the total energy and it is observed that S_0 decreases as the initial impact angle deviates from the normal incidence. In Fig. 7.2.b, the sticking probability is plotted as a function of the normal energy ($E_i \cos^2 \Theta_i$) and we verify that normal energy scaling does not apply in this case.

In general, molecular beam experiments are widely used as a standard technique to study the interactions between gases and metal surfaces. In Ref.[32], Auger-electron spectroscopy (AES) was additionally used to evaluate the initial sticking probability at the Fe(111) surface, with $T_s = 520 \text{ K}$ and for normal incidence. The measured initial sticking probabilities were determined from the initial slopes of coverage versus exposure curves in the AES spectra. Figure 7.3 illustrates the variation of the initial sticking probability S_0 with the initial impact energy for normal incidence. A comparison between our theoretical work and the experimental observation is shown. The two different curves appearing in Fig. 7.3 for the theoretical results correspond to surface

7. DISSOCIATIVE ADSORPTION DYNAMICS OF NITROGEN AT A FE(111) SURFACE

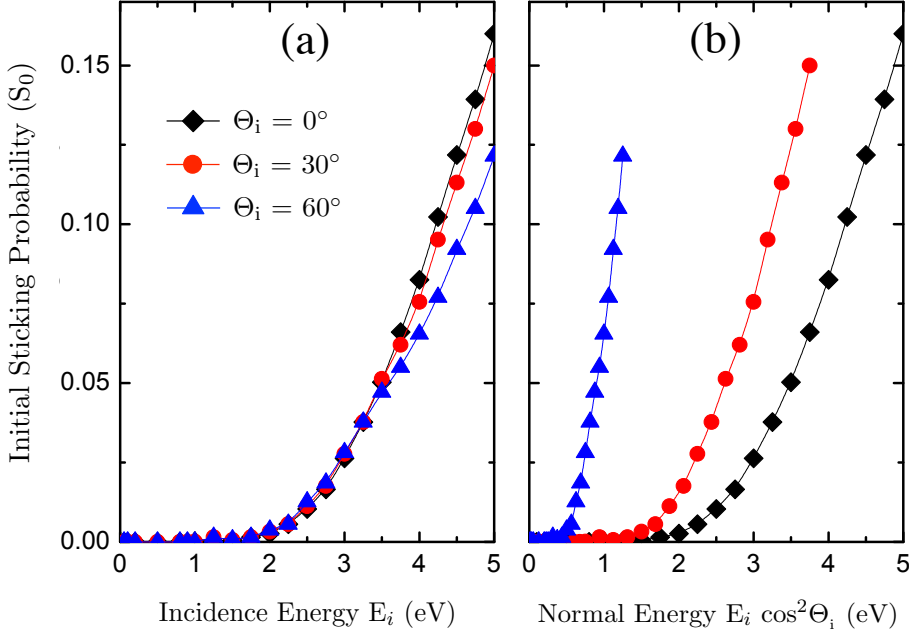


Figure 7.2: Dependence of the initial sticking probability S_0 on the initial incidence kinetic energy E_i for different incident angles Θ_i (a) as a function of the initial impact energy and (b) as a function of the normal energy.

temperatures of 520 K and 2000 K. Let us first focus on the N_2 dissociative adsorption curve for $T_s = 520$ K. Within the statistical error, the sticking probability is zero for kinetic energies below 0.80 eV. In the intermediate energy range, the sticking probability monotonously increases with the initial kinetic energy. At high energies S_0 matches the experimental measurements. The calculated sticking probabilities in Fig. 7.3 are slightly lower than the experimental ones. One possible reason for this difference is that the upper limit of our calculation time (10 ps) could be insufficient to simulate the full dynamics of the process and, hence, the probability of the final reactive and non-reactive channels. After 10 ps, some of the molecules remain dynamically trapped in the vicinity of the ε adsorption well. The trapped molecules are localized in this region until they gain enough energy to become either dissociated or reflected to the gas phase. Such process may require much longer simulation times. We have tried to estimate the final outcome of these dynamically trapped molecules by artificially increasing the surface temperature. An increase in surface temperature results in a large decrease in dynamically trapped molecules because energy exchange with the surface

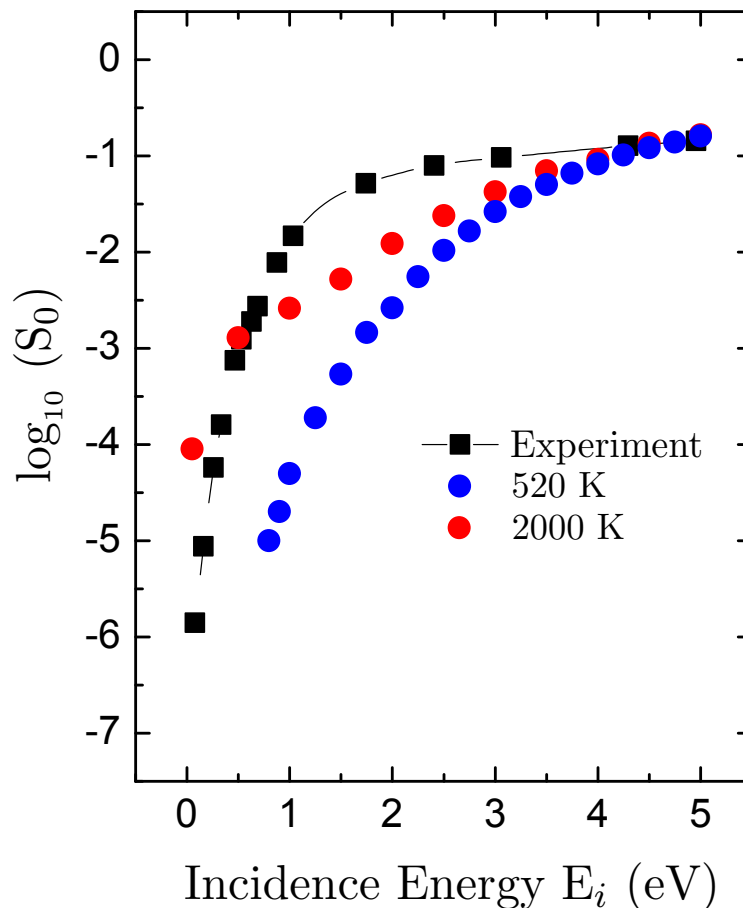


Figure 7.3: Initial sticking probability S_0 as a function of the initial impact energy E_i for normal incidence. Black squares are experimental data [32]. Blue and red circles are our theoretical results for surface temperatures $T_s = 520$ and 2000 K, respectively.

phonons is favored and the lifetime of the dynamically trapped state is shortened [103]. Therefore, we have performed QCT calculations at a surface temperature of $T_s = 2000$ K. Such value of the surface temperature implies that no trapped molecules remain at the surface within our calculation time limit of 10 ps. As shown in Fig. 7.3, the 2000 K results are close to the experimental data in the intermediate kinetic energy regime. The reason is that, for a higher surface temperature, some of the trajectories that were before dynamically trapped are now eventually dissociated. The translation of this conclusion to the dynamics at $T_s = 520$ K has to be made with some caution, however. An increase in the surface temperature is not only a way of accelerating the dynamics but can also modify them.

7. DISSOCIATIVE ADSORPTION DYNAMICS OF NITROGEN AT A FE(111) SURFACE

In our calculations we have verified that most of the dissociation events proceed via a direct mechanism in the high energy range. In the low energy regime, however, the study of the dissociative adsorption process requires to include the indirect mechanism, in which dynamic trapping plays a role. Let us analyze in detail the different dynamics involved in the two regimes. In order to get enough statistics, we will be using different surface temperatures. According to Fig. 7.3, the results, for instance, for $E_i = 1.00$ eV at $T_s = 2000$ K and for $E_i = 2.00$ eV at $T_s = 520$ K, give rise to roughly the same sticking probability. Hence, in Fig. 7.4, we show the positions of the dissociated molecules for the two incidence kinetic energies at the two different surface temperatures (i.e. $E_i = 1.00$ and 2.00 eV at $T_s = 2000$ and 520 K, respectively) just at the time at which the trajectory is identified as leading to dissociation (i.e., when $r_{\text{diss}} > 2.1125$ Å). For both kinetic energies, the positions of the center of mass ($X_{\text{cm}}, Y_{\text{cm}}$) of the dissociated molecules over the unit cell show that the dissociation occurs close to the position of the third layer atoms. The molecules are dissociated at heights below 1.0 Å from the surface and with an orientation parallel to the surface. Although the final positions of the dissociated molecules are very similar, the histogram of the number of rebounds before they eventually dissociate is different for the two kinetic energies. At $T_s = 520$ K and $E_i = 2.00$ eV (Fig. 7.4.a), the majority of molecules are dissociated after a small number of surface rebounds (i.e. direct mechanism). At $T_s = 2000$ K and $E_i = 1.00$ eV (Fig. 7.4.b), however, the dissociation process is characterized by a high number of rebounds at the surface. We have verified that these rebounds are produced in the vicinity of the ϵ adsorption well. In the latter case, the majority of the molecules are first accommodated at the surface and exchange energy with the surface phonons before becoming dissociated. Previous work on the dissociation process of N_2 on Fe(111) suggested that, at low kinetic energy, the N_2 molecules are dissociated through an intermediate state. Our dynamical calculations confirm that this is indeed the case.

The experimentally [125, 133, 135–138, 145] accepted general picture for the dissociation dynamics of N_2 on Fe(111) in the thermal regime assumes that the N_2 molecules are first attracted to the surface and accommodated perpendicularly on top of the first layer atoms (γ -state), without any entrance barrier. From this position, the N_2 molecules start rotating their axis from the surface normal and move further toward the surface overcoming a potential barrier (from γ - to α -state). In the last step, the molecules dissociate from the molecularly adsorbed α -state into the atomically adsorbed β -state.

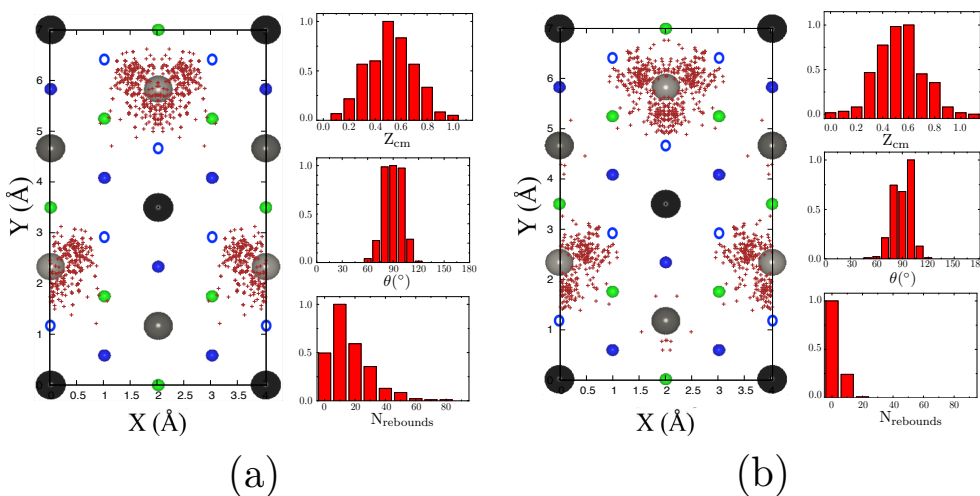


Figure 7.4: Left panel: position (X, Y) of the center of mass of the dissociated molecules at the time of dissociation. Right panel: height (Z_{CM}), polar angle (θ), and number of rebounds $N_{rebounds}$. (a) $E_i = 1.0$ eV with $T_s = 2000$ K, while (b) $E_i = 2.0$ eV with $T_s = 520$ K.

Moreover, direct adsorption into the α -state is known to be important at higher impact energies [125]. In Ref. [124, 133], it was experimentally estimated that the dissociation probability from the α -state to the β -state is of the order of 10^{-3} , and the rest of the molecules desorb to the vacuum when increasing the temperature. In our work, we can follow the dissociative adsorption dynamics for N₂ on Fe(111). However, we cannot compare our findings with this scenario because the molecular energies for which we can obtain significant statistics are much higher than the thermal energy regime in which the experimental information was obtained.

Figures 7.5, 7.6 explain the details of the dynamics for the dissociative adsorption process, for normal incidence. Two different cases are considered: $E_i = 1.00$ at $T_s = 2000$ K and 2.00 eV at $T_s = 520$ K. The first of these cases, even if the temperature is unrealistic as mentioned before, is chosen to be representative of some indirect dynamics. The upper panel represents snapshots of the center of mass coordinates of the dissociated molecules, as well as that of the reflected ones, over the surface unit cell, when reaching for the first time a distance Z from the surface. Supplementary information on top of each graph indicates the relative number of dissociated molecules that reach this distance Z , together with the number of molecules that are eventually reflected. The polar distribution of the dissociated molecules is shown in the lower panel.

7. DISSOCIATIVE ADSORPTION DYNAMICS OF NITROGEN AT A FE(111) SURFACE

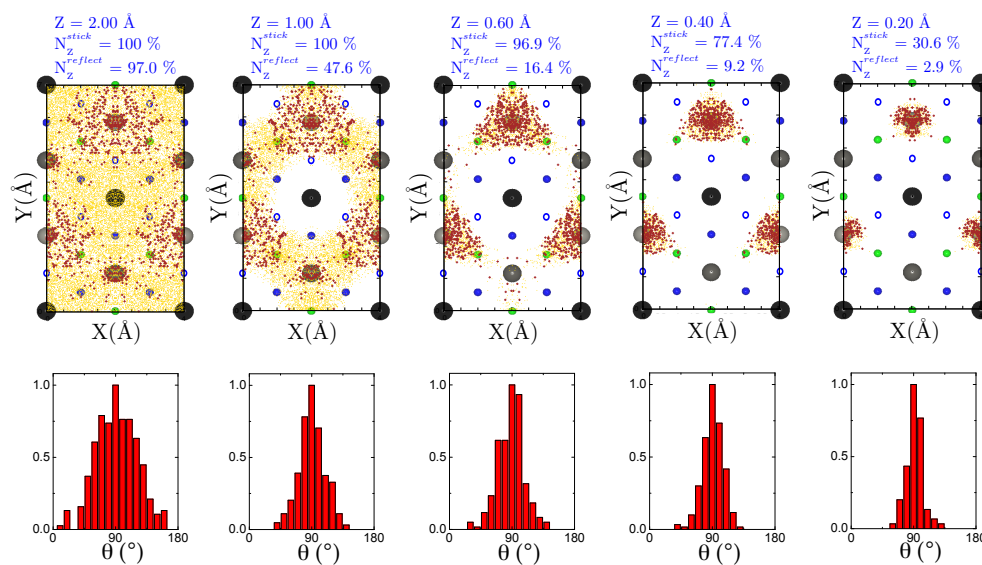


Figure 7.5: Analysis of the dissociation dynamics for normal incidence. 100 000 trajectories, with initial impact energy $E_i = 1.0$ eV and with surface temperature $T_s = 2000$ K. The upper panel shows the evolution of the (X, Y) coordinates of the N_2 molecules, when they reach a distance Z from the surface for the first time. The red and yellow symbols indicate, respectively, the dissociating and reflected molecules. Above each sampling area, a relative number of both the dissociated N_z^{stick} and reflected $N_z^{reflect}$ molecules that reach the indicated Z -value, is written. The polar angle θ -distribution is presented in the lower panel.

7.2 Dissociative Dynamics of N₂ on Fe(111)

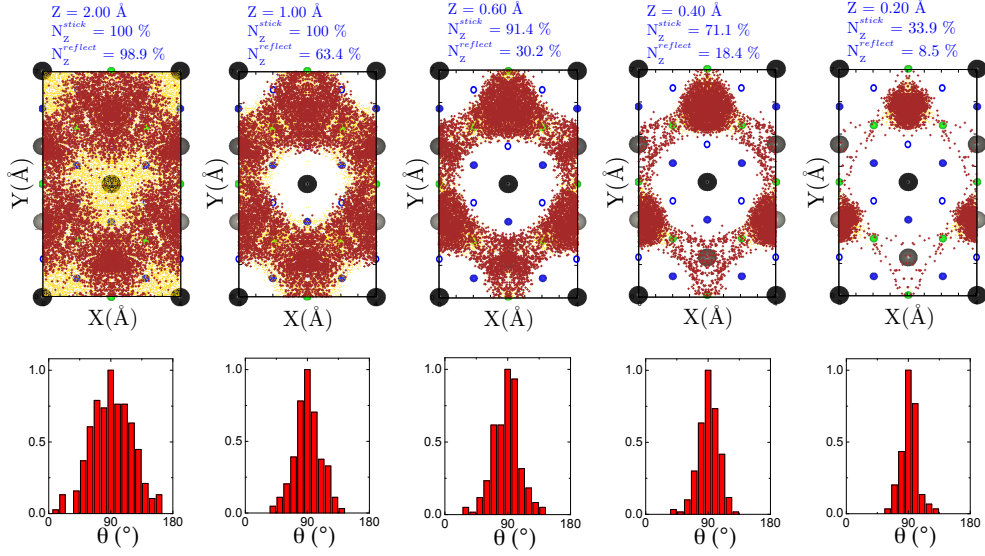


Figure 7.6: Same as Fig. 7.5 with an initial incidence energy $E_i = 2.0$ eV and $T_s = 2000$ K.

It is shown in Fig. 7.5 that all dissociated molecules reach the distance $Z = 2.0$ Å from the surface, keeping the positions of the center of mass (X, Y) and the molecular orientations (θ) very similar to the initial ones (not shown here). The same number of trajectories is recorded at $Z = 1.0$ Å, with a modified arrangement of the molecular positions and orientations over the surface. Molecules are placed now close to the *hollow* site as well as close to the third layer atoms. Further movement toward the surface gives rise to molecular dissociation events below $Z = 1.0$ Å. We conclude that, for this energy range, the molecules are dissociated in the vicinity of the third layer atoms with their axis oriented parallel to the surface, with an azimuthal orientation such that one of the atoms is located nearby the atomic adsorption well at the *hollow* site and the other atom is oriented toward the next atomic adsorption site. Figure 7.6 shows that the dynamics and the final position for dissociation are similar for $E_i = 2.0$ eV, with some additional opened channel for dissociation (close to the second layer atoms, and around the *hollow* site).

7. DISSOCIATIVE ADSORPTION DYNAMICS OF NITROGEN AT A Fe(111) SURFACE

7.3 Fe(111) versus Fe(110)

As mentioned in the introduction, the reactivity of N_2 on Fe surfaces much depends on the crystal face, with Fe(111) being the most reactive one and Fe(110) the least reactive one. In this context, we introduce a comparison between the nitrogen adsorption mechanisms on Fe(111) and Fe(110) from a theoretical side. Goikoetxea *et al.* studied both static and dynamic features of the N_2 /Fe(110) system [128]. They found two favorable molecular adsorption states over the surface. The deepest adsorption well lies parallel to the surface, at the bridge site, at $Z \approx 1.4 \text{ \AA}$, and with an adsorption energy of 298 meV (α -state). The other adsorption state is for a molecule perpendicularly adsorbed on top of the first layer, at $Z \approx 2.4 \text{ \AA}$, and with an adsorption energy of 184 meV (γ -state). For the two adsorption states, they obtained a large entrance barrier from the gas-phase toward the surface. This is already a qualitative difference between the two surfaces, because molecular adsorption is non activated in the Fe(111) case. There are four preferential molecular adsorption states of N_2 at the Fe(111) surface (i.e. γ , δ , α and ε). Besides the adsorption into the *hollow* site (α -state) there are adsorption states on the first, second and third layer atoms of the surface, characterized by large adsorption energy wells (450-640 meV).

Concerning reactive processes, for normal incidence, molecular dynamics simulations show that the dissociation on Fe(110) occurs mainly when the molecules are oriented parallel to the surface and close to the *hollow* site. They reported a dissociation barrier of $\approx 1.6 \text{ eV}$. The dissociation on both surfaces takes place when the molecules are placed parallel to the surface with one atom pointing toward the minimum adsorption site of the 3D-PES. The dissociation dynamics is ruled in both cases by narrow paths leading to the dissociated state. In the case of Fe(111), however, we report dissociative events at 800 meV, an energy which is half of that of the Fe(110) surface.

In general, the difference in the reactivity between the two surfaces is due to the different activation barriers. The openness of the Fe(111) surface makes the second and third layer atoms exposed to the N_2 molecules, which results in more available molecular adsorption sites on the surface (α and ε states), and hence in a higher dissociation probability compared to the close-packed Fe(110) surface. Experimentally, it was explained that the high reactivity of Fe(111) is attributed to the presence of C_7 coordination sites (number of nearest neighbours) of the N_2 for the second and third layer atoms

[31, 124, 146, 147], which is in turn associated with low surface work function and high surface free energy. The experimental picture is consistent with our conclusion for the low entrance and dissociation barriers as well as with the calculated properties of nitrogen adsorption and dissociation dynamics in $\text{N}_2/\text{Fe}(111)$.

7.4 Summary

In this chapter, we have presented a full dynamical study for the dissociative adsorption dynamics of N_2 on clean $\text{Fe}(111)$ surfaces. First, we performed quasi-classical trajectory calculations on a DFT-based 6D-PES to obtain the initial dissociative sticking probability S_0 . The QCT were performed for normal and off-normal incidence of N_2 molecules on the surface. The initial sticking probability shows a high dependence on the incidence angle. A comparison with experimental observations was introduced. Our results show sticking probabilities in general lower than the measured ones. A possible reason for that is that a large percentage of the incoming molecules remain trapped in an adsorption well. We have performed additional calculations for very high surface temperature in order to roughly estimate the ratio of the trapped molecules that will eventually dissociate. The theoretical results for molecular dissociation at high surface temperature show better agreement with the available experiments. Details of the dynamics indicate that most of the dissociated molecules approach parallel to the surface. The molecules are dissociated close to the third layer atoms with one of the atoms very close to the *hollow* site and the other one pointing towards the next possible atomic adsorption state. We also introduced a comparison between our current work and previous work on $\text{Fe}(110)$ for understanding the difference in reactivity for the two surfaces. $\text{Fe}(111)$ is higher in reactivity than $\text{Fe}(110)$, mainly due to the low entrance and activation barriers for the chemistry with N_2 , a conclusion which is consistent with the experimental studies.

7. DISSOCIATIVE ADSORPTION DYNAMICS OF NITROGEN AT A FE(111) SURFACE

Isotope Effects in Eley-Rideal Abstraction Dynamics of Hydrogen from Tungsten W(100) and W(110) Surfaces

The Eley-Rideal (ER) abstraction mechanism represents another interesting example of elementary reactions occurring at surfaces. In an ER process, an atom coming from the gas phase reacts with an atom already adsorbed at the surface to form a molecule that desorbs from the surface. One of the key points of the ER abstraction process is that this is a direct process, in which the incoming atom does not diffuse on the surface before the reaction. In our particular case, we will study the ER processes of hydrogen isotopes on W surfaces. Hydrogen abstraction on W is exothermic (≈ 1.5 eV for H+H/W) and results in a highly excited product. Moreover, investigations of hydrogen H and its isotopes (deuterium D and tritium T) recombinations on tungsten surfaces, have recently become highly attractive because of the construction of the International Thermonuclear Experimental Reactor (ITER). Tungsten is the main candidate for the diverters of the fusion reactor, a role in which it will be facing plasmas made of hydrogen isotope mixtures at energies of 1-10 eV [148–151].

Some of the first experimental studies of the ER abstraction mechanism were performed in the early 90's of the last century by Rettner and Auerbach [152, 153]. They observed a fast HD molecule in the reaction of a beam of H(D) atoms with D(H) atoms

8. ISOTOPE EFFECTS IN ELEY-RIDEAL ABSTRACTION DYNAMICS OF HYDROGEN FROM TUNGSTEN W(100) AND W(110) SURFACES

chemisorbed on a Cu(111) surface. Theoretical studies on the same system show, however, that in this case the molecular recombination proceeds mainly via the Hot-Atom process, in which the incidon (projectile) diffuses at thermal energy above the surface before interacting with the targon (target), giving a hot product [88, 154–156]. Motivated by the relatively high ER cross-sections, nitrogen interactions on metal surfaces have been recently studied [157, 158] on W surfaces [159–161], our target of interest. Although hydrogen is considered as the most popular example for the study of ER processes, there are only few studies that investigate in detail the effect of isotopic substitutions in the dynamics [152, 156, 162–165].

In this work we are mainly interested in the theoretical study of the ER abstraction dynamics for H and its isotopes, D and T, on tungsten W(100) and W(110) surfaces. To the best of our knowledge, there is no previous theoretical simulation done for these systems. This chapter is arranged as follows: Section 8.1 presents the theoretical tools that have been used to perform the simulations. Section 8.2 includes the ER dynamics results for different isotopic combinations, as well as a detailed study of the reaction dynamics. In Sec. 8.3, a comparison between the current work and the available experimental measurements is introduced. Finally, the conclusion of this chapter will be presented in Sec. 8.4

8.1 Methodology

We theoretically studied the ER recombination dynamics of hydrogen atoms and its isotopes on tungsten W(100) and W(110) surfaces by performing QCT calculations. Within the Born-Oppenheimer approximation, the continuous 6D-PESs for both surfaces were previously built by Pétuya *et al.* [95, 166], by using the FPLEPS [92–94] model. Due to the large mass mismatch between hydrogen and the surface atoms, the energy transfer to the phonons is expected to be small in the picosecond time scale [149, 167]. Moreover, the electron-hole pair excitations are neglected, as the time scale of the ER reaction is below the picosecond [144]. Our current work is based on a previous study for the H projectiles incident on H-covered W(100) and W(110) surfaces by Pétuya *et al.* [95]. Here we are only summarizing the methodology used to study the influence of the isotope effect on the ER abstraction dynamics, in the zero coverage

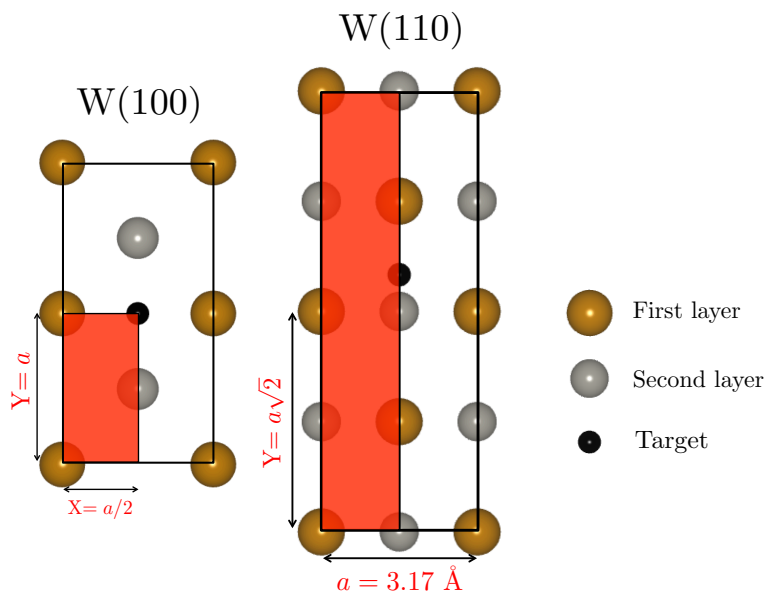


Figure 8.1: Representation of (a) W(100) and (b) W(110) surface atoms positions (X,Y) . Shaded areas refer to the sampling area of the initial positions of the projectile (X_p, Y_p) used in quasi-classical trajectory calculations. The first and the second surface layers atoms, as well as the target atom adsorption position, are indicated with gold, grey, and black symbols respectively. The W lattice parameter $a=3.17 \text{ \AA}$.

limit.

Figure 8.1 illustrates the geometrical structure of the W(100) and W(110) surfaces. The atomic target is initially located at its equilibrium adsorption position. The shaded area in Fig. 8.1 shows the surface representative sampling area used in the calculations. The (X,Y) positions are shown as a function of the tungsten lattice constant $a=3.17 \text{ \AA}$.

The zero point energy (ZPE) of the target atom was calculated in the previous work for the H pre-covered surface [95], within an X Y, and Z mode decomposition. Table 8.1 shows the ZPE values for the different target atoms (i.e., H, D, and T) in meV, for the three spatial coordinates X, Y, and Z. It is worth mentioning that we have performed additional calculations by changing the target ZPEs by a factor of 2 and the final results were not affected. This suggests that the results presented here are only modulated by mass effects and not by differences in the ZPEs, as previously noticed [156]. Surface temperature effects were included by applying the generalized Langevin oscillator (GLO) model [101–103]. The initial height of the projectile is chosen to be in the asymptotic region of the potential, at 7.0 \AA from the surface, with an initial

8. ISOTOPE EFFECTS IN ELEY-RIDEAL ABSTRACTION DYNAMICS OF HYDROGEN FROM TUNGSTEN W(100) AND W(110) SURFACES

perpendicular impact energy in the range of $E_p = 0.1\text{-}5.0$ eV. Taking advantage of the symmetry of each system, the (X_p, Y_p) initial position of the projectile is randomly sampled in the red areas (Fig. 8.1). To ensure sufficient statistics, a large number of trajectories is considered, namely, 320 000 and 640 000 for each E_p , for W(100) and W(110) respectively.

System	X	Y	Z
H/W(100)	55	33	67
H/W(110)	55	55	68
D/W(100)	39	23	47
D/W(110)	39	39	48
T/W(100)	32	19	39
T/W(110)	32	32	39

Table 8.1: Zero point energy in meV, for H, D, and T targets on W(100) and W(110) surfaces.

In our calculations, and after 2 ps, we can distinguish several exit channels. In particular, a new ER abstraction event is counted when projectile and target recombine with only one rebound of the center of mass of the molecule after the collision between projectile and surface [96]. The cross-section for each channel is calculated by the formula:

$$\sigma = A \int \int_D P(X_p, Y_p) dX_p dY_p, \quad (8.1)$$

where the integration is performed over D , the sampling area in Fig. 8.1. $P(X_p, Y_p)$, the two-dimensional opacity function, is the probability of one mechanism for a given set of initial coordinates (X_p, Y_p) of the projectile. The geometrical factor A appearing in Eq. 8.1 is taken as 2 and 4, respectively, for the sampling of the W(110) and W(100) surfaces.

8.2 Results and Discussion

Let us start this section with the study of the surface temperature effects on the ER abstraction dynamics. Figure 8.2 illustrates the dependence of the ER cross-sections on the initial impact energy of D-projectiles on D-covered W(100) and W(110) surfaces.

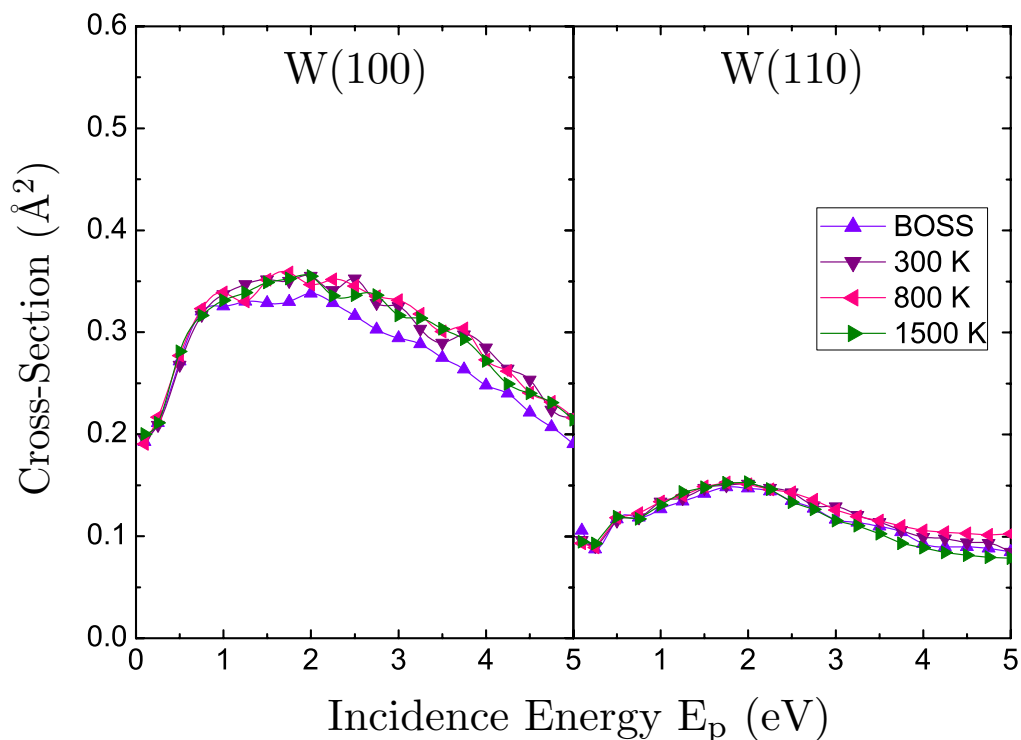


Figure 8.2: ER cross-section in \AA^2 for D on D-covered W(100) and W(110) surfaces, as a function of the initial incidence projectile energy in eV, within the BOSS model, as well as for surface temperatures 300, 800, and 1500 K.

Several surface temperatures (300K, 800K, and 1500K) are considered, as well as the BOSS approximation. As can be seen, the ER cross-sections of deuterium do not depend on the surface temperature, a behavior which is consistent with the one found in the study of hydrogen on the same surfaces [95]. Figure 8.2 shows that the qualitative behavior of ER cross-sections on W(100) is quite similar to that on W(110). The ER cross-sections are very small in the whole energy range, with values about 0.35 \AA^2 and 0.15 \AA^2 for W(100), and W(110) respectively. These results are similar to those found in previous studies of deuterium on other metal surfaces [88, 156, 168, 169].

Figure 8.3 shows the ER cross-section as a function of the projectile initial incidence energy E_p for different combinations of the hydrogen atom and its isotopes (H,D, and T) on W(100) and W(110), within the BOSS model. Over the full energy range and for different combinations, the cross-section values for W(100) are larger than the corresponding ones for the W(110) surface. In addition, the ER cross-sections seem to be

8. ISOTOPE EFFECTS IN ELEY-RIDEAL ABSTRACTION DYNAMICS OF HYDROGEN FROM TUNGSTEN W(100) AND W(110) SURFACES

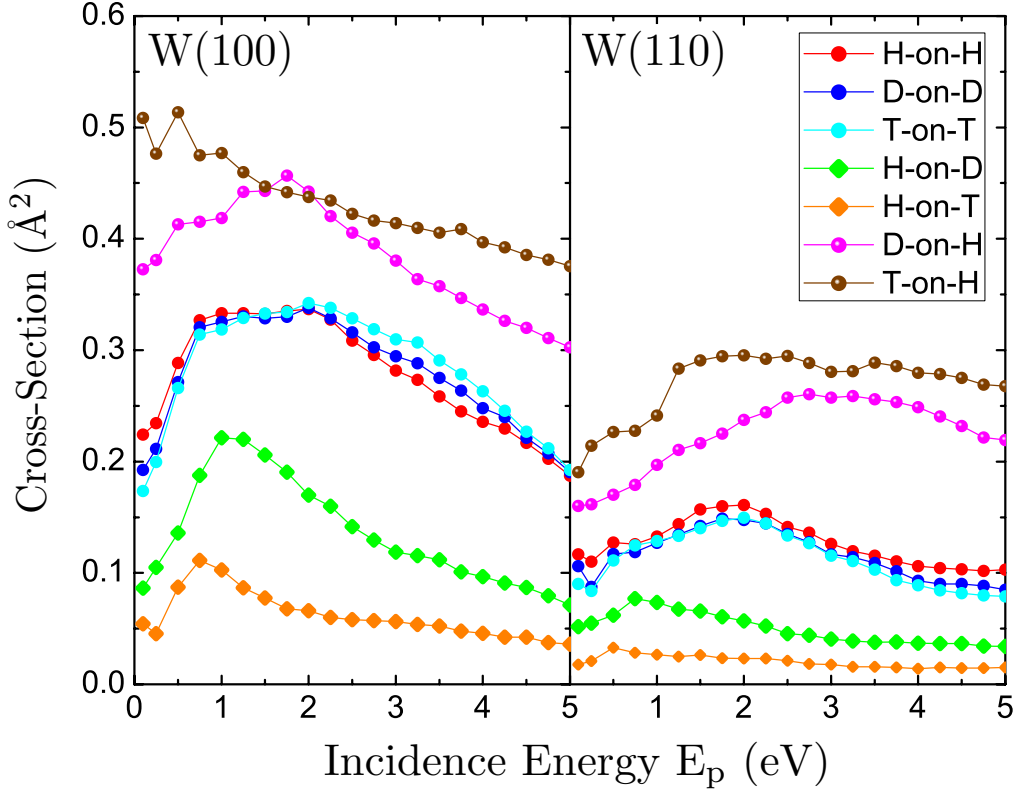


Figure 8.3: ER cross-sections in \AA^2 for collisions of H(D,T) on H(D,T)-precovered surfaces of W(100) (left panel) and W(110) (right panel), as a function of the projectile initial incidence energy, E_p , in eV. Calculations are performed within the BOSS model.

highly dependent on the mass ratio (m_p/m_t), where m_p is the projectile mass and m_t is the target mass. In the case of $m_p/m_t = 1$, ER cross-sections are nearly the same for H_2 , D_2 , and T_2 . Higher cross-sections are obtained when $m_p/m_t > 1$ and lower values are found for $m_p/m_t < 1$. The color maps used to illustrate different combinations in Fig 8.3 will be kept in the following analysis.

Next, we will restrict our analysis on the ER recombination dynamics to the systems: **H**-on-**H**, **D**-on-**D**, **H**-on-**D**, and **D**-on-**H**. A detailed analysis of the ER dynamical mechanisms for different hydrogen isotopes combinations on W(100) will be presented first. It will be followed by the same analysis for the recombination mechanisms on the W(110) surface. In Fig. 8.4, the opacity maps of the projectile rebound (first turning point) positions (X,Y) on the surface plane for the ER abstraction trajectories are represented for the W(100) surface with $E_p = 1.0$ eV. For all the systems, the trajectories leading

to ER abstraction involve in general projectile rebounds at roughly the same areas of the unit cell, close to the first and second layer atoms. ER abstraction is low at small impact parameters (close to the target atom) and mainly proceeds through the collision of the projectile with a W surface atom prior to recombination. In general, the same conclusion for the ER recombination pathways, interacting first with the surface atoms, was observed before for nitrogen recombination on tungsten surfaces [159]. The lower reactivity for H-on-D results mainly from a decrease of the reactivity in the symmetric rebound areas close to the W atoms centered at $Y = 0 \text{ \AA}$.

The corresponding distributions of heights (Z) for both projectile and target are presented in Fig. 8.5. In all cases, the maximum number of counts for target heights (black symbols) is around its initial distance from the surface ($Z_t = 1.2 \text{ \AA}$). However, there are two different mechanisms for the ER recombinations over the W(100) surface, characterized by two peaks for the projectile heights (colored symbols). One peak is close to the initial height of the target atom, and the other one is lower than this value. The former one refers to sideway collisions between the projectile and surface atoms that take place at the same height at which the target is (sideway mechanism). The latter one refers to collisions between the projectile and surface atoms that take place below the height at which the target is (push-up mechanism). In both cases, the projectile reacts with the target atom after the collision, in a trajectory that leads the so-formed molecule to the gas phase, to desorption.

From Fig. 8.5, the low ER cross-section for the light projectile (H) on the heavy target (D) does not arise from a significant decrease in the mechanism in which the projectile picks up the target from below via a *push-up* mechanism. It is rather that the efficiency of sideway collisions is strongly affected by the mass ratio between projectile and target. In the case in which $m_p/m_t < 1$, most of the trajectories rebounding at the height of the target atom are unreactive and end up in the reflection channel, as observed in reduced dimensional models [154, 162, 165, 170]. However, for other mass ratios, there is a larger probability for the projectile to capture the target atom when they are at the same height.

In a similar way, the ER abstraction dynamics for the W(110) surface are presented with the help of Fig. 8.6, Fig. 8.7, and Fig. 8.8. The rebound opacity maps presented in Fig. 8.6 for ER recombinations support our previous conclusion of the reactive areas close to the tungsten surface atoms and in the direction toward the target atom. The

8. ISOTOPE EFFECTS IN ELEY-RIDEAL ABSTRACTION
DYNAMICS OF HYDROGEN FROM TUNGSTEN W(100) AND
W(110) SURFACES

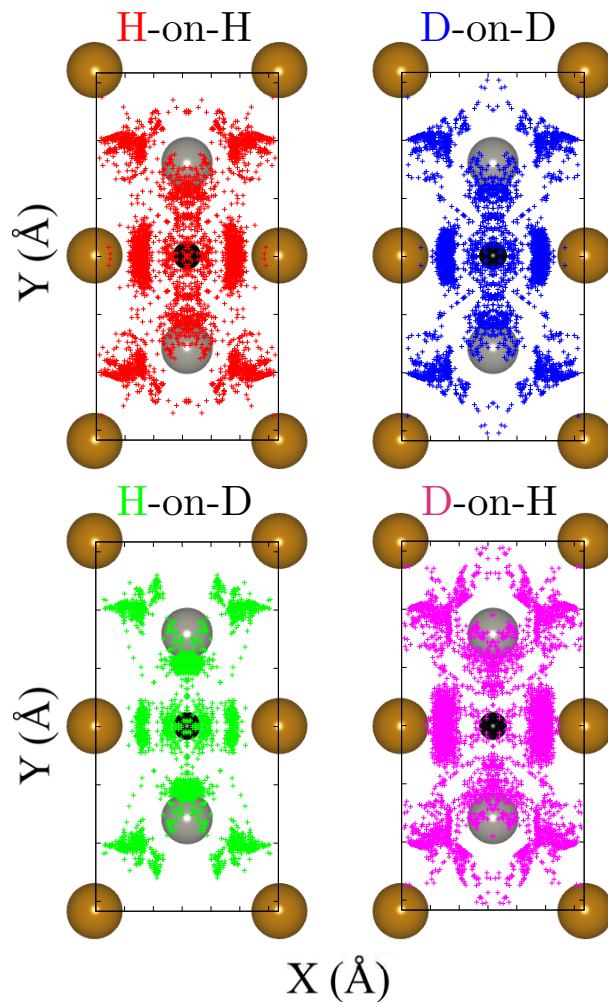


Figure 8.4: Rebound opacity maps for the W(100) reticular plane: (X_p, Y_p) rebound positions of the projectiles for the trajectories leading to ER recombination at initial impact energy of $E_p = 1.0$ eV.

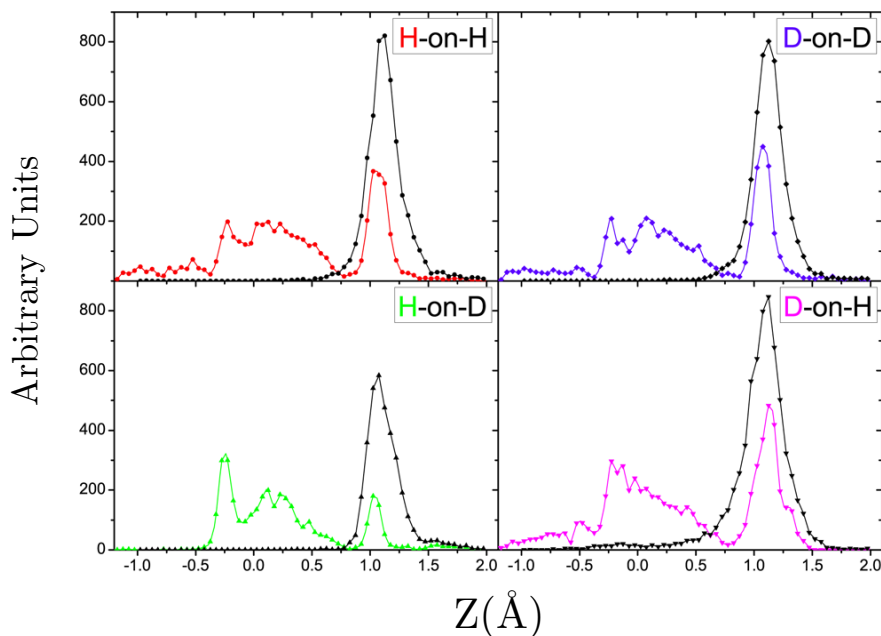


Figure 8.5: Distributions of projectile (color code described in the text) and target (black) heights at the first rebound of the projectile for ER abstraction trajectories on W(100) at initial energy of the projectile $E_p = 1.0$ eV.

main difference in the reactivity for different combinations can be understood if we focus on the density of reactive trajectories in the upper half of the unit cell, in the area above the target position. The density of rebound trajectories for the homonuclear case (H-on-H and D-on-D) is identical, while it almost disappears for the light projectile on heavy target (H-on-D), and is significantly increased for the heavy projectile on light target case (D-on-H). This can be confirmed by the distribution of rebound trajectories as a function of the Y coordinate shown in Fig. 8.7.

The peaks that account for the number of trajectories that make a rebound for $Y > 0$ almost vanish in the case of H-on-D. The corresponding heights for the different combinations leading to ER abstraction are shown in Fig. 8.8. Comparison between Fig. 8.5 and Fig. 8.8 reveals that the ER recombination mechanisms are similar in both surfaces. A light projectile must push out the heavy target from below in order to eject it, while a heavy projectile has an additional possibility to pick up a light target from its equilibrium height. We performed an additional analysis that confirmed that the previous rationalization of the recombination mechanisms also applies to isotopic

8. ISOTOPE EFFECTS IN ELEY-RIDEAL ABSTRACTION DYNAMICS OF HYDROGEN FROM TUNGSTEN W(100) AND W(110) SURFACES

combinations involving hydrogen and tritium atoms.

The final states for different isotopic combinations of ER abstraction molecules are displayed in Fig 8.9, which includes the final average vibrational, rotational, and translational energies as a function of the initial perpendicular incidence energy E_p , on tungsten W(100) and W(110) surfaces. The energy is varied between 50 meV and 5.0 eV. It can be seen from Fig. 8.9 that the isotopic influence not only affects the cross-sections of the ER probabilities, but also extends to the final states of the desorbed molecules. The internal and external energies of the molecules desorbed due to the ER reaction are different depending on the isotopic combination. At very low impact energy, half of the excitation energy goes to the product internal motion (vibrational and rotational excitation). When E_p increases, most of the available energy is transferred to the translation motion of the product molecule. This evidence agrees with the experimental results from Rettner *et al.* for studies of hydrogen and its isotopes on Cu(111) at low collision energy [152, 153, 163]. For W(100) and W(110), within all the initial collision energy range, the translational energy for the isotopic combination **D-on-H**, is higher than that of the homonuclear case, **H-on-H** and **D-on-D**, and the light/heavy substitution **H-on-D**. The final product rotational energy, however, seems to be not affected by different isotopic combinations. The vibrational excitation shows an effect contrary to the translational one. However, such subtle observables might be rather sensitive to the details of the PES [156].

8.3 Comparison with Experiments

Markelj *et al.* have measured the vibrational population of D_2 molecules emerging from a tungsten sample using vibrational spectroscopy [171]. The D_2 molecules are first dissociated at a hot tungsten filament at 2000 K and the D atoms then recombine on a W sample cooled at 286 K in medium vacuum conditions (10^{-3} mbar). Figure 8.10 illustrates the comparison between our simulations for the relative vibrational population of the excited D_2 from W(100) and W(110) at a surface temperature of $T_s = 300K$, and the corresponding available experimental data [171]. In our calculations, we performed a thermal averaging over the vibrational population using the same procedure presented in detail in previous studies [96, 172]. Neither in the experiments nor in our

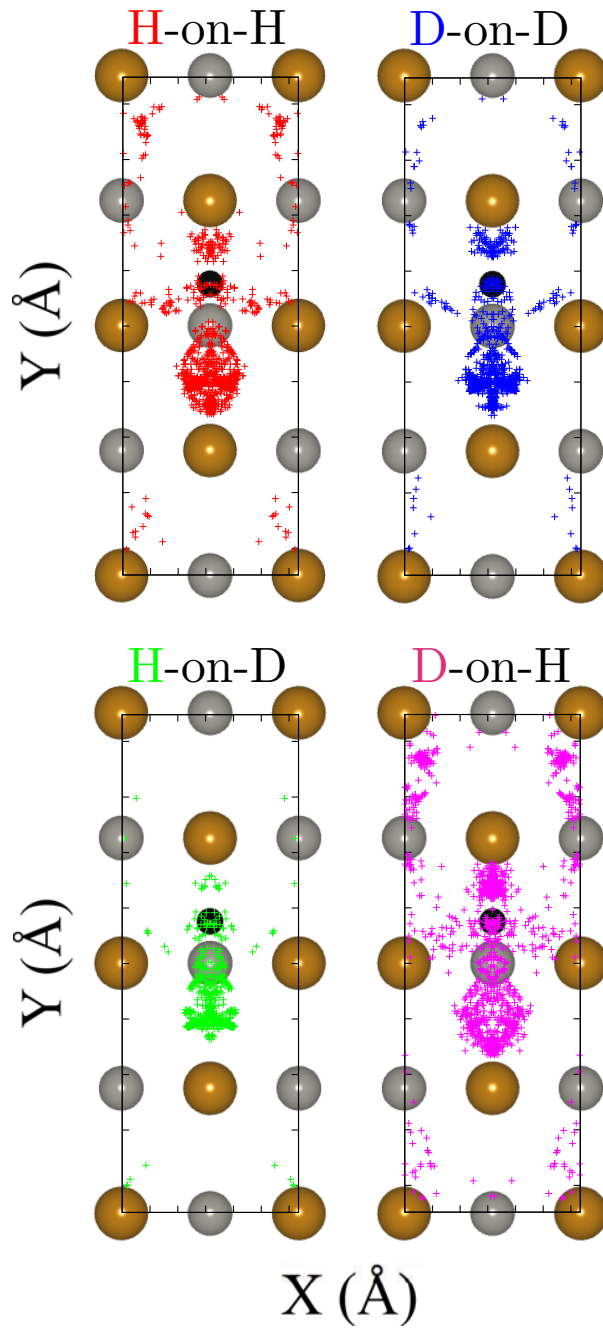


Figure 8.6: The same as Fig. 8.4 for the W(110) reticular plane.

8. ISOTOPE EFFECTS IN ELEY-RIDEAL ABSTRACTION DYNAMICS OF HYDROGEN FROM TUNGSTEN W(100) AND W(110) SURFACES

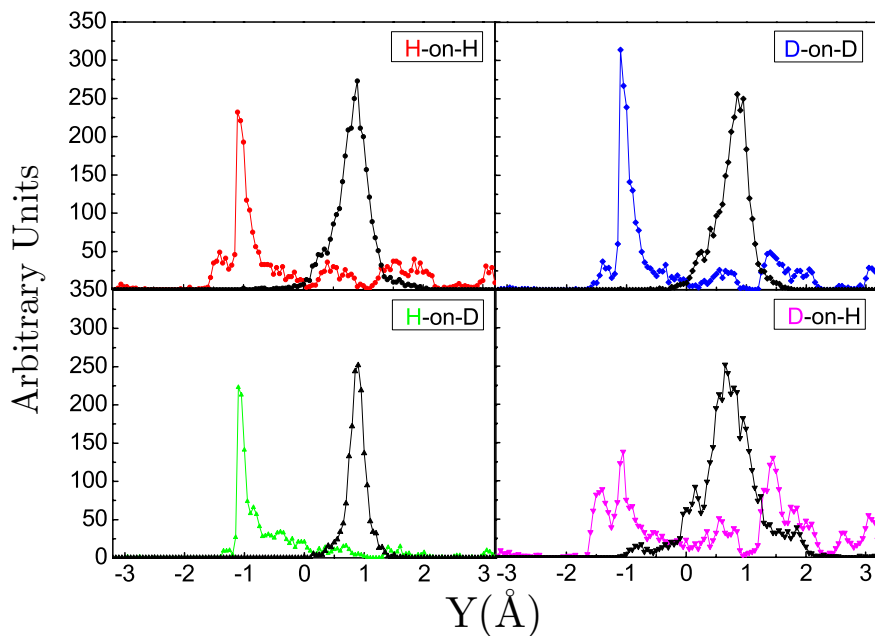


Figure 8.7: Distributions of the projectile Y coordinates at the first rebound of the projectile for ER abstraction trajectories on W(110), at initial energy of the projectile $E_p=1.0$ eV.

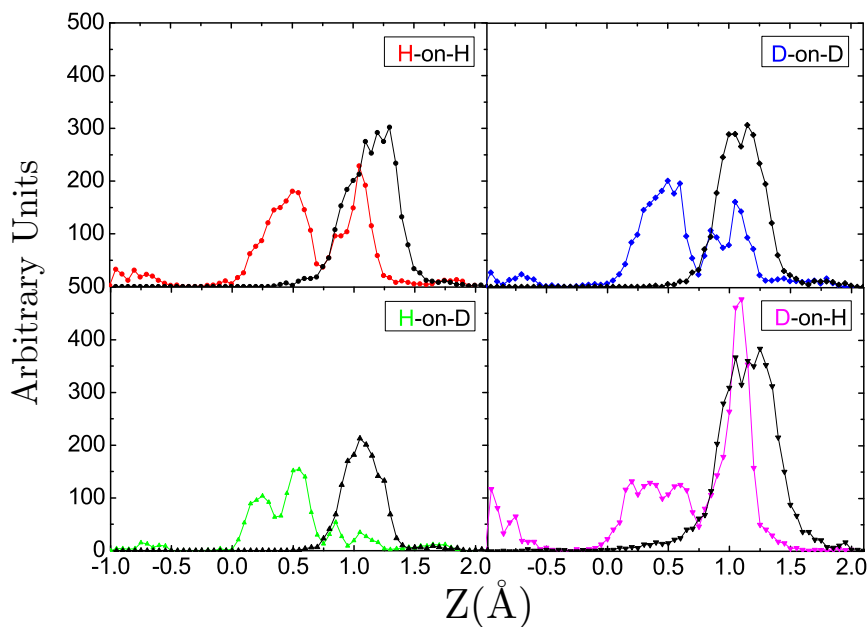


Figure 8.8: Distributions of the projectile Z coordinates at the first rebound of the projectile for ER abstraction trajectories on W(110) at initial energy of the projectile $E_p=1.0$ eV.

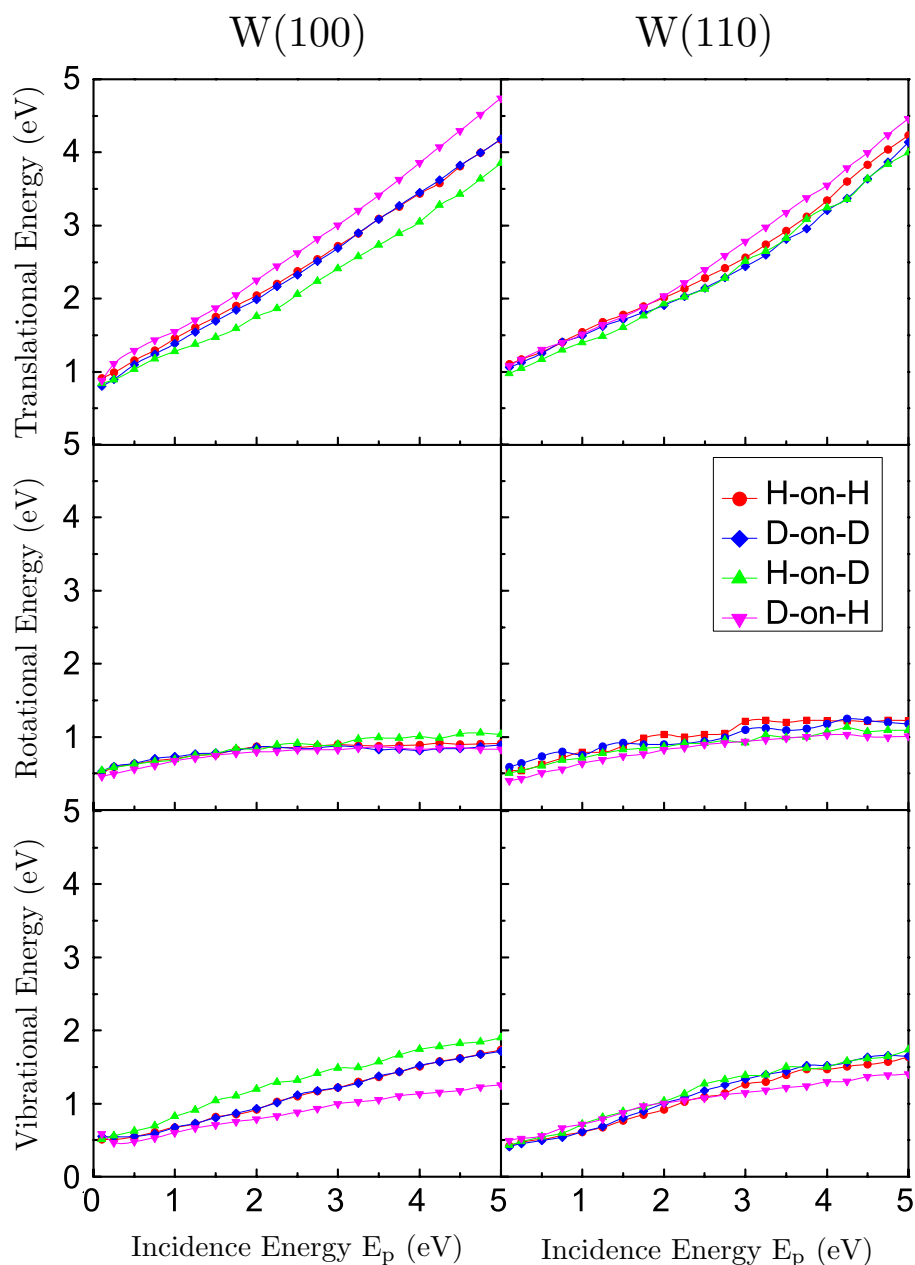


Figure 8.9: The product molecule final average translational (upper panel), rotational (middle panel), and vibrational (lower panel) energies in eV, as a function of the initial energy of the projectile, E_p (eV). Different isotopic substitutions in W(100) and W(110) surfaces are considered.

8. ISOTOPE EFFECTS IN ELEY-RIDEAL ABSTRACTION DYNAMICS OF HYDROGEN FROM TUNGSTEN W(100) AND W(110) SURFACES

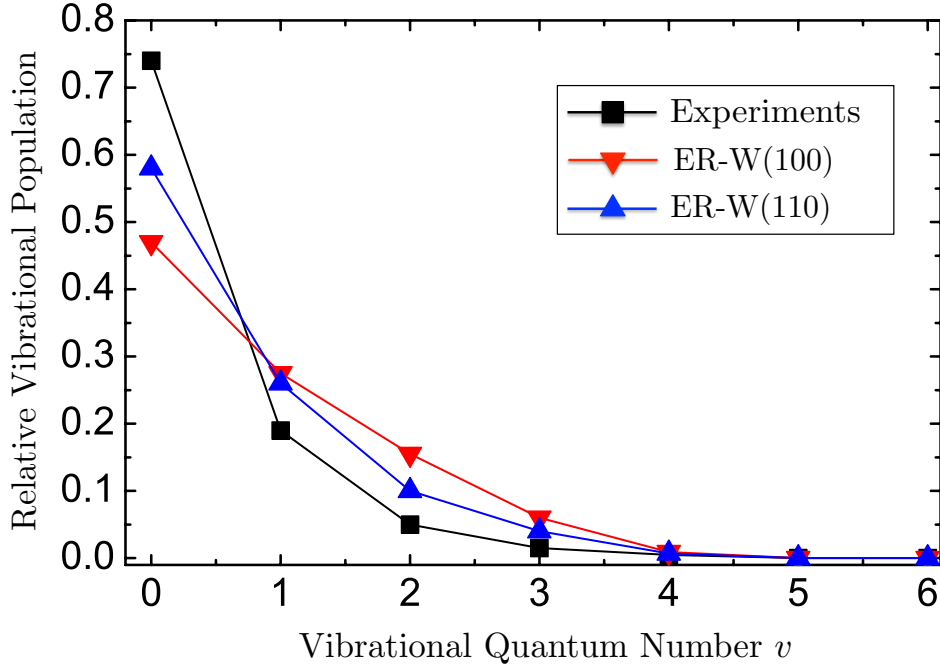


Figure 8.10: Relative vibrational populations of the recombined molecules. Red and blue triangles represent the ER single adsorbate results at a surface temperature of 300 K, respectively, on W(100) and W(110). Black squares represent the experimental results [171]. Lines are drawn to guide the eye. Results for excitation higher than $v = 6$ (population about 10^{-4} and lower) are not displayed.

simulations there is any significant population of vibrational levels higher than $v = 5$. We may conclude that our results show a good agreement with the experimental measurements, in particular in the W(110) case. However, small differences do exist. The experimental distributions are slightly colder than the theoretical ones. The difference may stem from energy dissipation to e-h pairs upon abstraction.

8.4 Summary

In this chapter, we have presented a theoretical study for the effect of different isotopic combinations of hydrogen in the ER abstraction dynamics on tungsten W(100) and W(110) surfaces. We remain at the limit of single adsorbates and use quasi-classical trajectory calculations performed on 6D-PESs constructed using the FPLPES model. For a wide range of initial perpendicular projectile energies, our QCT calculation show

a rough invariance of the ER cross-sections with changes in the surface temperature. In general, in all the energy range considered, the ER cross-sections for different isotope combinations are higher on W(100) than the corresponding ones on W(110). In addition, the ER cross-sections over the two different reticular plans are ordered by the (m_p/m_t) ratios. This effect is connected to the higher (lower) reflection probability of a light (heavy) projectile from a heavy (light) target. In general, ER abstraction is preceded by a collision of the projectile with a tungsten surface atom first. After this collision, the projectile captures the target atom and forms a molecule that is desorbed towards the gas-phase, regardless of the isotopic combination and surface symmetry. Two mechanisms are identified in the ER abstraction dynamics, namely a sideways mechanism and a push-up mechanism. The dependence of the former on the m_p/m_t ratio is the main responsible of the isotope effect. Moreover, the isotope effects also appear in the final states of the formed molecules. Most of the released energy goes into the translational motion of the molecule. Our results show a good agreement with experimental measurements for the molecular vibrational distributions at room temperature.

**8. ISOTOPE EFFECTS IN ELEY-RIDEAL ABSTRACTION
DYNAMICS OF HYDROGEN FROM TUNGSTEN W(100) AND
W(110) SURFACES**

9

Conclusions

In this thesis, I have presented a theoretical study of the interaction between N_2 and Fe(111) surfaces. In addition, I have also studied the isotope effects in the reaction dynamics of the hydrogen atom and its isotopes with the tungsten surfaces W(100) and W(110). The elementary reactive processes have been studied by applying different methodologies. Density functional theory (DFT) was employed to obtain a quantitative description of the geometry and energetics of the reactants. The DFT microscopic insight was combined with thermodynamics and statistical mechanics in order to calculate the reaction rates of the elementary processes.

I have presented an introduction into the standard time-independent DFT, as well as a practical implementation of the theory for electronic structure calculations. After that, I have introduced in detail the interpolation methods that have been applied to build potential energy surfaces (PESs) that describe the systems under study. Then, a general overview of the method that has been utilized for performing classical dynamics simulations was added.

For the investigation of the Fe(111) structural properties, we have performed DFT calculations to study the bulk properties and the topmost surface layers relaxations. Our results for the bulk modulus and the lattice parameters show a good agreement with the experimental measurements. The surface layers exhibit only displacements perpendicular to the surface plan and no reconstruction was observed. The first two interlayer relaxation distances tend to contract, while the third interlayer spacing expands. Our results demonstrate the independence of the surface relaxations on the number of layers in the slab. The Fe(111) surface multi-layers relaxations show a qualitative agreement,

9. CONCLUSIONS

but with some quantitative differences, with the experimental measurements. The interaction energy for the nitrogen molecule on top of several slabs with different number of layers does not depend on the number of slab layers.

The frozen surface approximation was applied to a slab consisting of 9-layers for the representation of the Fe(111) surface during the calculations of the reaction dynamics of nitrogen atoms and molecules with the surface. First, we performed DFT calculations for atomic nitrogen approaching perpendicular to several sites of the clean Fe(111) surface. The hollow site is the preferred adsorption site of nitrogen atoms on the surface, with an atomic adsorption energy that is within the range of previous studies of the nitrogen atoms on Fe surfaces. Then, a grid of DFT data points for the interaction of N_2 with the surface was made, taken into account the molecule six degrees of freedom. The 3D and 6D continuous potential energy surfaces were constructed by interpolation of the DFT points through the corrugation reducing procedure (CRP). A comparison of the CRP interpolated data with the corresponding DFT energies shows the high efficiency of CRP as a numerical interpolation method. A systematic analysis of the 6D-PES demonstrates that there are four local adsorption minima for N_2 on the Fe(111) surface. At the molecular equilibrium distance, there are two adsorption states with the molecular axis oriented in a direction perpendicular to the Fe surface, located on top of the first and second layer atoms. Two additional adsorption states are found, with a stretched internuclear distance, with the molecular axis parallel to the surface, and located on the hollow site and on top of the third layer atoms. The adsorption states on the first, second, and third layer atoms are characterized by slightly different values of the adsorption energies. Adsorption into the hollow site represents the deepest adsorption energy well of the 6D-PES.

The adsorption dynamics of N_2 at a clean Fe(111) surface was studied by means of quasi-classical trajectory (QCT) calculations, for a wide range of initial impact energies and with several surface temperatures. Our QCT results trace the dependence of the molecular adsorption dynamics and of the adsorption probability on the surface temperature. Details of the adsorption dynamics show that molecular adsorption is governed by the molecule initial kinetic energy and the magnitude of the entrance barrier. At very low energy, adsorption into the state on top of the first layer atoms is dominant. Access to this state is not hindered by any energy barrier and the relative adsorption probability is close to unity. As the molecule initial energy increases,

molecular adsorption into the hollow site and on the third layer atoms become the preferential adsorption channels. These adsorption states are associated with small entrance barriers. In general, our QCT calculations confirm general ideas proposed for the molecular adsorption dynamics of N_2 on Fe(111), extracted from previous experimental observations and static theoretical predictions.

As a continuation of the study of the elementary reactions of N_2 on Fe(111), we addressed the dissociative adsorption dynamics, using initial conditions similar to those of the study of molecular adsorption dynamics. Our results trace the dependence of the initial sticking probability on the angle of incidence. For normal incidence and impact energies lower than 3 eV, our theoretical results are below the experimental values. Better agreement with the experiment is obtained if we increase the surface temperature to promote the transfer to dissociation of molecules previously trapped. For high energies of the beam, the dynamics of the dissociated molecules shows that the dissociation process is a direct process that occurs via narrow dissociation paths. Most of the molecules dissociate very close to the Fe(111) third layer atoms and with an orientation parallel to the surface. We also introduced a comparison between our work and previous work on Fe(110) to understand the difference in reactivity between the two surfaces. Fe(111) is higher in reactivity than Fe(110), mainly due to the low entrance and activation barriers found by the N_2 molecule, a conclusion which is consistent with the experimental studies.

Finally, we have studied the isotope effects for different isotopic combinations of the hydrogen atom in the Eley-Rideal (ER) abstraction dynamics on the tungsten surfaces W(100) and W(110), in the single adsorbate limit. We have found, in general, that the ER cross-sections are relatively small. In addition, ER cross-sections for W(100) are larger than the corresponding ones in W(110). The ER cross-sections for D_2 are independent of the tungsten surface temperatures, a result that agrees with previous studies for hydrogen atoms. Within the Born-Oppenheimer static surface (BOSS) approach, the ER cross-section values are related to the projectile/target mass ratio m_p/m_t . The ER cross-sections are nearly identical for homonuclear combinations, larger when the m_p/m_t ratio is greater than 1, and smaller when the m_p/m_t ratio is smaller than 1. This effect is connected to the higher (lower) reflection probability of the heavy (light) projectile/target combinations. At both surfaces, ER proceeds through a collision of the projectile with a tungsten surface atom before being redirected toward the target.

9. CONCLUSIONS

Two different mechanisms are identified in the ER abstraction dynamics, namely a sideways mechanism and a push-up mechanism. The dependence of the former on the m_p/m_t ratio is the main responsible for the isotope effect. Moreover, isotope effects also appear in the final states of the formed molecules. Most of the released energy goes into the translational motion of the molecule. Our results show a good agreement with experimental measurements for the molecular vibrational distributions at room temperature.

All in all, the work presented in this manuscript proves that theoretical studies based on ab-initio calculations are accurate tools to describe, understand, and predict the dynamics of elementary reactive processes at surfaces.

Appendix A

Interpolation Procedures

This appendix is adapted to the study of the N₂/Fe(111) system. The material is mostly imported from the work of G.A. Bocan* *et al.* in their studies of nitrogen on Ag(111) systems [144, 157, 173], taking advantage of the similar symmetry that the Fe(111) and Ag(111) surfaces present.

In this appendix, we show the interpolation procedures that have been used to construct the six-dimensional potential energy surface (6DPES) of the N₂/Fe(111) system, via the CRP method, from the grid of DFT data points. In general, we have to perform interpolations over the molecule six-degrees of freedom (X, Y, Z, r, θ, ϕ). First, the interpolation over (r, Z) is performed through a cubic splines method. The interpolation over the molecular orientations (θ, ϕ) proceeds by employing trigonometric functions. Finally, the interpolation over the surface cartesian coordinates (X, Y) is carried out using a Fourier expansion.

In all cases, we have the following equivalent configuration:

$$(\theta, \phi) = (\pi - \theta, \phi + \pi). \quad (\text{A.1})$$

Interpolation in ϕ

- **Case 1: *top, hcp, and fcc***

The coordinates (X_{cm}, Y_{cm}) of the calculated ab-initio points are shown in Fig. 5.6. The three sites have identical symmetry. We have calculated six different configurations that are actually

* CONICET and Centro Atómico Bariloche (CNEA), Argentina.

A. INTERPOLATION PROCEDURES

representative of thirteen. They follow:

$$\begin{aligned}
 V_0 &\equiv V(\theta = 0^\circ, \phi = 0^\circ) = V(\theta = 180^\circ, \phi = 0) \\
 V_1 &\equiv V(\theta = 90^\circ, \phi = 30^\circ) \\
 V_2 &\equiv V(\theta = 90^\circ, \phi = 60^\circ) \\
 V_3 &\equiv V(\theta = 45^\circ, \phi = 30) = V(\theta = 135^\circ, \phi = 210) \equiv V(\theta = 135^\circ, \phi = 90^\circ) \\
 V_4 &\equiv V(\theta = 45^\circ, \phi = 60) = V(\theta = 135^\circ, \phi = 240) \equiv V(\theta = 135^\circ, \phi = 0) \\
 V_5 &\equiv V(\theta = 45^\circ, \phi = 90) = V(\theta = 135^\circ, \phi = 270) \equiv V(\theta = 135^\circ, \phi = 30),
 \end{aligned} \tag{A.2}$$

because Eq. A.1 implies rotational symmetry of 120° .

For $\theta = 0^\circ$ and 180° , we have to consider only one configuration ($\theta = 0^\circ, \phi = 0^\circ$):

$$\begin{aligned}
 V_0(\phi) &= V_0(0) = V_0 \\
 V_{180}(\phi) &= V_{180}(0) = V_0.
 \end{aligned} \tag{A.3}$$

For $\theta = 90^\circ$, we have two ab-initio configurations ($\theta = 90^\circ$ with $\phi = 30^\circ, 60^\circ$). According to the symmetry conditions we get :

$$\begin{aligned}
 V_{90}(\phi) &= V_{90}\left(\phi + \frac{\pi}{3}\right) \\
 V_{90}(\phi) &= V_{90}(\pi - \phi).
 \end{aligned} \tag{A.4}$$

By using the trigonometric functions that fulfill the symmetry conditions, we can obtain the coefficient for each calculated point as follows:

$$V_{90}(\phi) = A_0 + A_1 \cos(6\phi). \tag{A.5}$$

Then,

$$\begin{aligned}
 V_1 = V_{90}\left(\frac{\pi}{6}\right) &= A_0 + A_1 \cos\left(6\frac{\pi}{6}\right) = A_0 - A_1 \\
 V_2 = V_{90}\left(\frac{\pi}{3}\right) &= A_0 + A_1 \cos\left(6\frac{\pi}{3}\right) = A_0 + A_1,
 \end{aligned} \tag{A.6}$$

which finally yields,

$$V_{90}(\phi) = \frac{1}{2}(V_1 + V_2) + \frac{1}{2}(V_2 - V_1) \cos(6\phi). \tag{A.7}$$

For $\theta = 45^\circ$, we have three ab-initio calculated configurations ($\theta = 45^\circ$ with $\phi = 30^\circ, 60^\circ, 90^\circ$). According to the symmetry properties:

$$\begin{aligned}
 V_{45}(\phi) &= V_{45}\left(\phi + 2\frac{\pi}{3}\right) \\
 V_{45}(\phi) &= V_{45}(\pi - \phi).
 \end{aligned} \tag{A.8}$$

Consequently, by using the trigonometric functions, we get

$$V_{45}(\phi) = A_0 + A_1 \sin(3\phi) + A_2 \cos(6\phi). \quad (\text{A.9})$$

Then

$$\begin{aligned} V_3 &= V_{45}\left(\frac{\pi}{6}\right) = A_0 + A_1 \sin\left(3\frac{\pi}{6}\right) + A_2 \cos\left(6\frac{\pi}{6}\right) = A_0 + A_1 - A_2 \\ V_4 &= V_{45}\left(\frac{\pi}{3}\right) = A_0 + A_1 \sin\left(3\frac{\pi}{3}\right) + A_2 \cos\left(6\frac{\pi}{3}\right) = A_0 + A_2 \\ V_5 &= V_{45}\left(\frac{\pi}{2}\right) = A_0 + A_1 \sin\left(3\frac{\pi}{2}\right) + A_2 \cos\left(6\frac{\pi}{2}\right) = A_0 - A_1 - A_2, \end{aligned} \quad (\text{A.10})$$

which finally gives

$$V_{45}(\phi) = \frac{V_3 + 2V_4 + V_5}{4} + \frac{V_3 - V_5}{2} \sin(3\phi) + \frac{2V_4 - V_3 - V_5}{4} \cos(6\phi). \quad (\text{A.11})$$

Similarly, for $\theta = 135^\circ$, we have three different configurations ($\theta = 135^\circ$ with $\phi = 30^\circ, 60^\circ, 90^\circ$), then

$$V_{135}(\phi) = \frac{V_3 + 2V_4 + V_5}{4} + \frac{V_5 - V_3}{2} \sin(3\phi) + \frac{2V_4 - V_3 - V_5}{4} \cos(6\phi). \quad (\text{A.12})$$

• **Case 2: hollow, top-hcp, and top-fcc**

In this case, the coordinates (X_{cm}, Y_{cm}) of the calculated ab-initio points are those of *hollow*, *top-hcp*, and *top-fcc* sites (see Fig. 5.6). We have eight ab-initio configurations. The surface symmetry provides us with six additional configurations:

$$\begin{aligned} V_0 &\equiv V(\theta = 0^\circ, \phi = 0^\circ) = V(\theta = 180^\circ, \phi = 0^\circ) \\ V_1 &\equiv V(\theta = 90^\circ, \phi = 90^\circ) \\ V_2 &\equiv V(\theta = 90^\circ, \phi = 0^\circ) \\ V_3 &\equiv V(\theta = 45^\circ, \phi = 270^\circ) = V(\theta = 135^\circ, \phi = 90^\circ) \\ V_4 &\equiv V(\theta = 45^\circ, \phi = 0^\circ) = V(\theta = 135^\circ, \phi = 180^\circ) \\ V_5 &\equiv V(\theta = 45^\circ, \phi = 90^\circ) = V(\theta = 135^\circ, \phi = 270^\circ) \\ V_6 &\equiv V(\theta = 90^\circ, \phi = 30^\circ) \\ V_7 &\equiv V(\theta = 90^\circ, \phi = 60^\circ) \end{aligned} \quad (\text{A.13})$$

For $\theta = 0^\circ$ and $\theta = 180^\circ$, we have only one ab-initio calculated point:

$$V_0(\phi) = V_0(0) = V_{180}(0) = V_0 \quad (\text{A.14})$$

A. INTERPOLATION PROCEDURES

For $\theta = 90^\circ$ we have four calculated configurations ($\theta = 90^\circ$ with $\phi = 90^\circ, 0^\circ, 30^\circ, 60^\circ$). Applying symmetry conditions:

$$\begin{aligned} V_{90}(\phi) &= V_{90}(\pi - \phi) \\ V_{90}(\phi) &= V_{90}(\phi + \pi). \end{aligned} \tag{A.15}$$

We make the expansion in trigonometric functions

$$V_{90}(\phi) = A_0 + A_1 \cos(2\phi) + A_2 \cos(4\phi) + A_3 \cos(6\phi) \tag{A.16}$$

so that:

$$\begin{aligned} V_1 &= V_{90}\left(\frac{\pi}{2}\right) = A_0 + A_1 \cos\left(2\frac{\pi}{2}\right) + A_2 \cos\left(4\frac{\pi}{2}\right) + A_3 \cos\left(6\frac{\pi}{2}\right) \\ &= A_0 - A_1 + A_2 - A_3, \\ V_2 &= V_{90}(0) = A_0 + A_1 \cos(0) + A_2 \cos(0) + A_3 \cos(0) \\ &= A_0 + A_1 + A_2 + A_3, \\ V_6 &= V_{90}\left(\frac{\pi}{6}\right) = A_0 + A_1 \cos\left(2\frac{\pi}{6}\right) + A_2 \cos\left(4\frac{\pi}{6}\right) + A_3 \cos\left(6\frac{\pi}{6}\right) \\ &= A_0 + \frac{1}{2}A_1 - \frac{1}{2}A_2 - A_3, \\ V_7 &= V_{90}\left(\frac{\pi}{3}\right) = A_0 + A_1 \cos\left(2\frac{\pi}{3}\right) + A_2 \cos\left(4\frac{\pi}{3}\right) + A_3 \cos\left(6\frac{\pi}{3}\right) \\ &= A_0 - \frac{1}{2}A_1 - \frac{1}{2}A_2 + A_3, \end{aligned} \tag{A.17}$$

which finally results in

$$\begin{aligned} V_{90}(\phi) &= \frac{V_1 + V_2 + 2V_6 + 2V_7}{6} + \frac{V_2 - V_1 + V_6 - V_7}{3} \cos(2\phi) \\ &+ \frac{V_1 + V_2 - V_6 - V_7}{3} \cos(4\phi) + \frac{V_2 - V_1 - 2V_6 + 2V_7}{6} \cos(6\phi) \end{aligned} \tag{A.18}$$

For $\theta = 45^\circ$, we have only three ab-initio configurations (i.e., $\theta = 45^\circ$ with $\phi = 270^\circ, 0^\circ, 90^\circ$). The symmetry conditions are:

$$\begin{aligned} V_{45}(\phi) &= V_{45}(\phi + 2\pi) \\ V_{45}(\phi) &= V_{45}(\pi - \phi). \end{aligned} \tag{A.19}$$

Therefore:

$$V_{45}(\phi) = A_0 + A_1 \sin(\phi) + A_2 \cos(2\phi), \quad (\text{A.20})$$

and:

$$\begin{aligned} V_3 &= V_{45}\left(\frac{3\pi}{2}\right) = A_0 + A_1 \sin\left(\frac{3\pi}{2}\right) + A_2 \cos\left(2\frac{3\pi}{2}\right) = A_0 - A_1 - A_2, \\ V_4 &= V_{45}(0) = A_0 + A_1 \sin(0) + A_2 \cos(0) = A_0 + A_2, \\ V_5 &= V_{45}\left(\frac{\pi}{2}\right) = A_0 + A_1 \sin\left(\frac{\pi}{2}\right) + A_2 \cos\left(2\frac{\pi}{2}\right) = A_0 + A_1 - A_2, \end{aligned} \quad (\text{A.21})$$

and we finally find that:

$$V_{45}(\phi) = \frac{V_5 + 2V_4 + V_3}{4} + \frac{V_5 - V_3}{2} \sin(\phi) + \frac{-V_5 + 2V_4 - V_3}{4} \cos(2\phi) \quad (\text{A.22})$$

For $\theta = 135^\circ$ we have a case similar to $\theta = 45^\circ$. We have three additional configurations (i.e., $\theta = 45^\circ$ with $\phi = 90^\circ, 180^\circ, 270^\circ$):

$$V_{135}(\phi) = \frac{V_5 + 2V_4 + V_3}{4} + \frac{V_3 - V_5}{2} \sin(\phi) + \frac{-V_5 + 2V_4 - V_3}{4} \cos(2\phi) \quad (\text{A.23})$$

From Fig. 5.6, there are six additional sites according to the Fe(111) surface symmetry, which we also use in the interpolation procedures. The additional sites in cartesian coordinates are: *hollow*₂($a\frac{\sqrt{2}}{4}, a\frac{3}{2\sqrt{6}}$), *top-hcp*₂($a\frac{3\sqrt{2}}{4}, a\frac{1}{2\sqrt{6}}$), *top-fcc*₂($a\frac{3\sqrt{2}}{4}, a\frac{5}{2\sqrt{6}}$), *hollow*₃($a\frac{3\sqrt{2}}{4}, a\frac{3}{2\sqrt{6}}$), *top-hcp*₃($a\frac{\sqrt{2}}{4}, a\frac{1}{2\sqrt{6}}$), and *top-fcc*₃($a\frac{\sqrt{2}}{4}, a\frac{5}{2\sqrt{6}}$). Since they have the same symmetry conditions of their corresponding counterparts, the interpolation functions and their coefficients are computed as in Eqs. A.14, A.18, A.22, A.23.

Interpolation in θ

For the interpolation in θ , we have the following symmetry condition for all sites used as references in the interpolation procedure:

$$V(\theta) = V(\theta + \pi). \quad (\text{A.24})$$

The expansion in terms of trigonometric functions can be written as:

$$V(\theta) = B_0 + B_1 \sin(2\theta) + B_2 \cos(2\theta) + B_3 \sin(4\theta) + B_4 \cos(4\theta), \quad (\text{A.25})$$

A. INTERPOLATION PROCEDURES

where the coefficients B_0 , B_1 , B_2 , B_3 , and B_4 are evaluated from the substitution in this expression of the θ -values used in building the DFT-grid, i.e., $\theta = 0^\circ, 45^\circ, 90^\circ, 135^\circ$, and 180° :

$$\begin{aligned}
 V(0) &= B_0 + B_2 + B_4 = V_0, \\
 V\left(\frac{\pi}{4}\right) &= B_0 + B_1 - B_4 = V_{45}, \\
 V\left(\frac{\pi}{2}\right) &= B_0 - B_2 + B_4 = V_{90}, \\
 V\left(\frac{3\pi}{4}\right) &= B_0 - B_1 - B_4 = V_{135}. \\
 V(\pi) &= B_0 + B_2 + B_4 = V_{180}
 \end{aligned} \tag{A.26}$$

The coefficients are finally given by,

$$\begin{aligned}
 B_0 &= \frac{V_0 + V_{45} + V_{90} + V_{135}}{4} \\
 B_1 &= \frac{V_{45} - V_{135}}{2} \\
 B_2 &= \frac{V_0 - V_{90}}{2} \\
 B_4 &= \frac{V_0 + V_{90} - V_{45} - V_{135}}{4}
 \end{aligned} \tag{A.27}$$

XY interpolation using Fourier expansion

This is the third step in the interpolation of the DFT data. First, the interpolation over the (r, Z) coordinates is performed. Second, the interpolation over the angular variables (θ, ϕ) is performed. After this, the interpolation over the 2D surface coordinates (X, Y) is performed. For this purpose, twelve set of coordinates in (u, v) are used for the representation of the surface positions: *top* ($u = 0, v = 0$), *hcp* ($u = 1/3, v = 1/3$), *fcc* ($u = 2/3, v = 2/3$), *hollow* ($u = 1/2, v = 0$), *top-hcp* ($u = 1/6, v = 2/3$), *top-fcc* ($u = 5/6, v = 1/3$), *hollow₂* ($u = 0, v = 1/2$), *top-hcp₂* ($u = 2/3, v = 1/6$), *top-fcc₂* ($u = 1/3, v = 5/6$), *hollow₃* ($u = 1/2, v = 1/2$), *top-hcp₃* ($u = 1/6, v = 1/6$), and *top-fcc₃* ($u = 5/6, v = 5/6$). Here, (u, v) are the coordinates in the basis set of the unitary vectors \hat{e}_v and \hat{e}_u that define the unit cell as shown in Fig. A.1.

The Fourier expansion for the 2D interpolation function $F_{\text{mol}}^{6\text{D}}$ is given by:

$$F_{\text{mol}}^{6\text{D}}(u, v) = \sum_{l,m} C_1 (\vec{G}_{l,m}) \sin(\vec{G}_{l,m} \cdot \vec{\rho}_{CM}) + C_2 (\vec{G}_{l,m}) \cos(\vec{G}_{l,m} \cdot \vec{\rho}_{CM}), \tag{A.28}$$

The vectors used for the representation of the grid $\vec{\rho}_{CM}$ and $\vec{G}_{l,m}$ have the following expressions:

$$\begin{aligned}
 \vec{\rho}_{CM} &= X_{CM} \hat{x} + Y_{CM} \hat{y} \\
 &= u \hat{e}_u + v \hat{e}_v \\
 &= \delta \left(u + \frac{v}{2} \right) \hat{x} + \delta v \frac{\sqrt{3}}{2} \hat{y},
 \end{aligned} \tag{A.29}$$

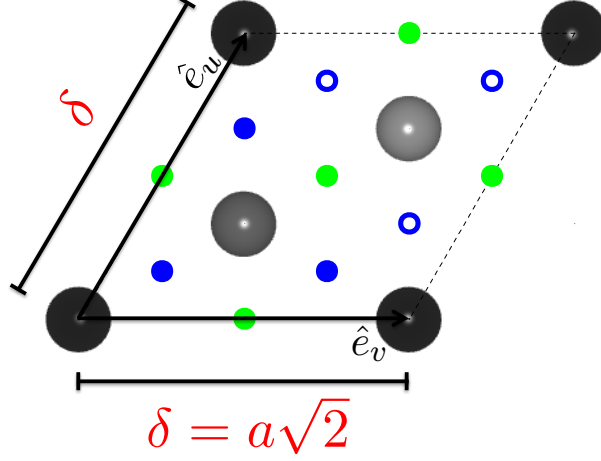


Figure A.1: Illustration of the unitary vectors \hat{e}_v and \hat{e}_u , which define the grid (u, v) , and the distance between the surface atoms δ in terms of the lattice parameter a .

where δ is the distance between the surface atoms (i.e., $\delta = a\sqrt{2}$, a being the lattice parameter), \hat{x} and \hat{y} are unitary vectors in the X and Y directions respectively and the unit cell vectors are given as

$$\begin{aligned}\hat{e}_u &= \delta \hat{x} \\ \hat{e}_v &= \delta \left(\cos\left(\frac{\pi}{3}\right) \hat{x} + \sin\left(\frac{\pi}{3}\right) \hat{y} \right),\end{aligned}\tag{A.30}$$

and

$$\begin{aligned}\vec{G}_{l,m} &= l \vec{b}_u + m \vec{b}_v \\ &= l \frac{2\pi}{\delta} \hat{x} + \frac{2\pi}{\delta\sqrt{3}} (-l + 2m) \hat{y},\end{aligned}\tag{A.31}$$

where

$$\begin{aligned}\bar{b}_u &= \frac{4\pi}{\delta\sqrt{3}} \left(\cos\left(-\frac{\pi}{6}\right) \hat{x} + \sin\left(-\frac{\pi}{6}\right) \hat{y} \right) \\ \bar{b}_v &= \frac{4\pi}{\delta\sqrt{3}} \left(\cos\left(\frac{\pi}{2}\right) \hat{x} + \sin\left(\frac{\pi}{2}\right) \hat{y} \right).\end{aligned}\tag{A.32}$$

Equation A.28 may be written in terms of the twelve (u, v) points representing the surface as:

$$F_{\text{mol}}^{6\text{D}}(u, v) = F_0 + F_1 + F_2 + F_3 + \dots,\tag{A.33}$$

A. INTERPOLATION PROCEDURES

which can be evaluated for each one of the positions considered by substituting the corresponding (u, v) values in the product

$$\vec{G}_{l,m} \cdot \vec{\rho}_{CM} = 2\pi (lu + mv) \quad (\text{A.34})$$

The 2D interpolation function will be finally given by

$$\begin{aligned} F_{\text{mol}}^{6\text{D}}(u, v) &= B_0 + B_1 \sin(2\pi(u+v)) + B_2 \cos(2\pi(u+v)) \\ &+ B_3 \sin(2\pi u) + B_4 \cos(2\pi u) + B_5 \sin(2\pi v) + B_6 \cos(2\pi v) \\ &+ B_8 \cos(2\pi(2u+v)) + B_{10} \cos(2\pi(u+2v)) + B_{12} \cos(2\pi(u-v)) \quad (\text{A.35}) \\ &+ B_{13} \left(\sin(2\pi(2u+2v)) - \sin(2\pi(2u)) - \sin(2\pi(2v)) \right) \\ &+ B_{14} \left(\cos(2\pi(2u+2v)) - \cos(2\pi(2u)) - \cos(2\pi(2v)) \right). \end{aligned}$$

References

- [1] R. DÍEZ MUIÑO AND H. F. BUSNENGO. *Dynamics of Gas-Surface Interactions: Atomic-level Understanding of Scattering Processes at Surfaces*, **50**. Springer Series of Surface Sciences, Berlin, 2013. 1, 3, 37, 38, 42, 43, 48
- [2] I. CHORKENDORFF AND J.W. NIEMANTSVERDRIET. *Concepts of Modern Catalysis and Kinetics*, **50**. Wiley-VCH Verlag GmbH Co. KGaA, Weinheim, FRG, 2005. 2, 5
- [3] G. A. SOMORJAI AND Y. LI. **Impact of surface chemistry**. *Proceedings of the National Academy of Sciences*, **108**(3):917, 2011. 2
- [4] O. DEUTSCHMANN, H. KNÖZINGER, K. KOCHLOEFL, AND T. TUREK. **Heterogeneous Catalysis and Solid Catalysts**. In *Ullmann's Encyclopedia of Industrial Chemistry*. Wiley-VCH Verlag GmbH Co. KGaA, 2000. 2
- [5] M. KITANO, Y. INOUE, Y. YAMAZAKI, F. HAYASHI, S. KANBARA, S. MATSUISHI, T. YOKOYAMA, S-W. KIM, M. HARA, AND H. HOSONO. **Ammonia synthesis using a stable electride as an electron donor and reversible hydrogen store**. *Nature Chemistry*, **4**(11):943, 2012. 3
- [6] I. RAFIQU, C. WEBER, B. LEHMANN, AND A. VOSS. **Energy efficiency improvements in ammonia production-perspectives and uncertainties**. *Energy*, **30**(13):2487, 2005.
- [7] Y. TANABE AND Y. NISHIBAYASHI. **Developing more sustainable processes for ammonia synthesis**. *Coordination Chemistry Reviews*, **257**(17-18):2551, 2013. 3
- [8] H. LIU. **Ammonia synthesis catalyst 100 years: Practice, enlightenment and challenge**. *Chinese Journal of Catalysis*, **35**(10):1619, 2014. 3
- [9] G. A. SOMORJAI. *Introduction to Surface Chemistry and Catalysis*. John Wiley & Sons, Inc., New York, 2nd edition, 2010. 3
- [10] Y. H. FLEMMING, N. E. HENRIKSEN, G. D. BILLING, AND A. GULDBERG. **Catalytic synthesis of ammonia using vibrationally excited nitrogen molecules: theoretical calculation of equilibrium and rate constants**. *Surface Science*, **264**(1):225, 1992. 3

REFERENCES

- [11] A. HELLMAN, E. J. BAERENDS, M. BICZYSKO, T. BLIGAARD, C. H. CHRISTENSEN, D. C. CLARY, S. DAHL, R. VAN HARREVELT, K. HONKALA, H. JONSSON, G. J. KROES, M. LUPPI, U. MANTHE, J. K. NØRSKOV, R. A. OLSEN, J. ROSSMEISL, E. SKULASON, C. S. TAUTERMANN, A. J. C. VARANDAS, AND J. K. VINCENT. **Predicting Catalysis: Understanding ammonia synthesis from first-principles calculations.** *The Journal of Physical Chemistry B*, **110**(1):17719, 2006.
- [12] M. KITANO, S. KANBARA, Y. INOUE, N. KUGANATHAN, P. V. SUSHKO, T. YOKOYAMA, M. HARA, AND H. HOSONO. **Electride support boosts nitrogen dissociation over ruthenium catalyst and shifts the bottleneck in ammonia synthesis.** *Nature Communications*, **6**:6731, 2015.
- [13] P. IYNGARAN, D. C. MADDEN, S. J. JENKINS, AND D. A. KING. **Hydrogenation of N over Fe(111).** *Proceedings of the National Academy of Sciences*, **108**(3):925, 2011.
- [14] G. ERTL. **Primary steps in catalytic synthesis of ammonia.** *Journal of Vacuum Science & Technology A*, **1**(2):1247, 1983.
- [15] G. ERTL. **Ammonia Synthesis - Heterogeneous.** In *Encyclopedia of Catalysis*. John Wiley & Sons, Inc., 2002.
- [16] P. STOLTZE AND J.K. NØRSKOV. **An interpretation of the high-pressure kinetics of ammonia synthesis based on a microscopic model.** *Journal of Catalysis*, **110**(1):1, 1988. 3
- [17] M. BOUDART. **Ammonia synthesis: The bellwether reaction in heterogeneous catalysis.** *Topics in Catalysis*, **1**(3):405, 1994. 3
- [18] C. DÍAZ. **Theoretical simulations of reactive and nonreactive scattering of light diatomic molecules from metal surfaces: Past, Present, and Future.** *Advances in Chemistry*, **2014**:175351, 2014. 3
- [19] B. HAMMER AND J.K. NØRSKOV. **Theoretical surface science and catalysis-calculations and concepts.** In *Impact of Surface Science on Catalysis*, **45** of *Advances in Catalysis*, page 71. Academic Press, 2000. 5, 6, 7
- [20] J. K. NØRSKOV. **Chemisorption on metal surfaces.** *Reports on Progress in Physics*, **53**(10):1253, 1990. 5
- [21] J. K. NØRSKOV, F. ABILD-PEDERSEN, F. STUDDT, AND T. BLIGAARD. **Density functional theory in surface chemistry and catalysis.** *Proceedings of the National Academy of Sciences*, **108**(3):937, 2011. 5
- [22] L. M. FALICOV AND G. A. SOMORJAI. **Correlation between catalytic activity and bonding and coordination number of atoms and molecules on transition metal**

- surfaces: Theory and experimental evidence.** *Proceedings of the National Academy of Sciences*, **82**(8):2207, 1985. 6
- [23] C. T. RETTNER, E. K. SCHWEIZER, H. STEIN, AND D. J. AUERBACH. **Role of surface temperature in the precursor-mediated dissociative chemisorption of N_2 on W(100).** *Physical Review Letters*, **61**:986, 1988. 6, 79
- [24] C. T. RETTNER, H. STEIN, AND E. K. SCHWEIZER. **Effect of collision energy and incidence angle on the precursor-mediated dissociative chemisorption of N_2 on W(100).** *The Journal of Chemical Physics*, **89**(5):3337, 1988.
- [25] R. PÉTUAYA, P.-A. PLÖTZ, C. CRESPOS, AND P. LARRÉGARAY. **Revisiting the non-reactive scattering of N_2 off W(100): On the influence of the scattering azimuth on In-plane angular distributions.** *The Journal of Physical Chemistry C*, **118**(38):21904, 2014. 6, 45
- [26] H. E. PFNÜR, C. T. RETTNER, J. LEE, R. J. MADIX, AND D. J. AUERBACH. **Dynamics of the activated dissociative chemisorption of N_2 on W(110): A molecular beam study.** *The Journal of Chemical Physics*, **85**(12):7452, 1986. 6
- [27] I. GOIKOETXEA, J. I. JUARISTI, M. ALDUCIN, AND R. DÍEZ MUIÑO. **Dissipative effects in the dynamics of N_2 on tungsten surfaces.** *Journal of Physics: Condensed Matter*, **21**(26):264007, 2009. 6
- [28] M. ALDUCIN, R. DÍEZ MUIÑO, H. F. BUSNENGO, AND A. SALIN. **Low sticking probability in the nonactivated dissociation of N_2 molecules on W(110).** *The Journal of Chemical Physics*, **125**(14):144705, 2006. 6, 74, 77
- [29] M. ALDUCIN, R. DÍEZ MUIÑO, H. F. BUSNENGO, AND A. SALIN. **Why N_2 molecules with thermal energy abundantly dissociate on W(100) and not on W(110).** *Physical Review Letters*, **97**:056102, 2006.
- [30] L. MARTIN-GONDRE, C. CRESPOS, P. LARRÉGARAY, J. C. RAYEZ, B. VAN OOTEGEM, AND D. CONTE. **Dynamics simulation of N_2 scattering onto W(100,110) surfaces: A stringent test for the recently developed flexible periodic London-Eyring-Polanyi-Sato potential energy surface.** *The Journal of Chemical Physics*, **132**(20):204501, 2010. 6
- [31] N.D. SPENCER, R.C. SCHOONMAKER, AND G.A. SOMORJAI. **Iron single crystals as ammonia synthesis catalysts: Effect of surface structure on catalyst activity.** *Journal of Catalysis*, **74**(1):129, 1982. 6, 97
- [32] C. T. RETTNER AND H. STEIN. **Effect of translational energy on the chemisorption of N_2 on Fe(111): Activated dissociation via a precursor state.** *Physical Review Letters*, **59**:2768, 1987. 7, 89, 91

REFERENCES

- [33] C. T. RETTNER AND H. STEIN. **Effect of vibrational energy on the dissociative chemisorption of N₂ on Fe(111).** *The Journal of Chemical Physics*, **87**(1):770, 1987. 7
- [34] L. VATTUONE, L. SAVIO, F. PIRANI, D. CAPPELLETTI, M. OKADA, AND M. ROCCA. **Interaction of rotationally aligned and of oriented molecules in gas-phase and at surfaces.** *Progress in Surface Science*, **85**(1-4):92, 2010. 7
- [35] K. REUTER. **Ab Initio thermodynamics and first-principles microkinetics for surface catalysis.** *Catalysis Letters*, **146**(3):541, 2016. 7
- [36] A. GROSS. *Theoretical Surface Science: A Microscopic Perspective.* Springer Berlin Heidelberg, Berlin, Heidelberg, 2009. 12, 19, 31
- [37] M. BORN AND R. OPPENHEIMER. **Zur Quantentheorie der Molekeln.** *Annalen der Physik*, **389**(20):457, 1927. 14, 38
- [38] R. P. FEYNMAN. **Forces in molecules.** *Physical Review*, **56**:340, 1939. 15
- [39] S. T. EPSTEIN, A. C. HURLEY, R. E. WYATT, AND R. G. PARR. **Integrated and integral Hellmann-Feynman formulas.** *The Journal of Chemical Physics*, **47**(4):1275, 1967. 15
- [40] K. BURKE. **Perspective on density functional theory.** *The Journal of Chemical Physics*, **136**(15):150901, 2012. 16
- [41] L. H. THOMAS. **The calculation of atomic fields.** *Mathematical Proceedings of the Cambridge Philosophical Society*, **23**:542, 1927. 17
- [42] E. FERMI. **Un metodo statistico per la determinazione di alcune proprietà dell'atomo.** *Rend. Accad. Naz. Lincei*, **6**:602, 1927. 17
- [43] G.R PARR AND W. YANG. *Density-Functional Theory of Atoms and Molecules.* International series of monographs on chemistry 16. Oxford University Press; Clarendon Press, 1994. 17
- [44] P. HOHENBERG AND W. KOHN. **Inhomogeneous electron gas.** *Physical Review*, **136**:B864, 1964. 18, 20, 23, 54, 62
- [45] W. KOHN AND L. J. SHAM. **Self-consistent equations including exchange and correlation effects.** *Physical Review*, **140**:A1133, 1965. 20, 54, 62
- [46] J. P. PERDEW AND K. SCHMIDT. **Jacob-s ladder of density functional approximations for the exchange-correlation energy.** *AIP Conference Proceedings*, **577**(1):1, 2001. 23, 26, 27

-
- [47] L.E.F. FOA TORRES, S. ROCHE, AND J.-C. CHARLIER. *Introduction to Graphene-Based Nanomaterials: From Electronic Structure to Quantum Transport*. CUP, 2014. 23, 28, 30, 32
- [48] P. A. M. DIRAC. **Note on exchange phenomena in the Thomas atom**. *Mathematical Proceedings of the Cambridge Philosophical Society*, **26**:376, 1930. 23
- [49] J. F. DOBSON, V. GIOVANNI, AND M. P. DAS. *Electronic Density Functional Theory: Recent Progress and New Directions*. Springer US, 1 edition, 1998. 24
- [50] J. P. PERDEW AND Y. WANG. **Accurate and simple analytic representation of the electron-gas correlation energy**. *Physical Review B*, **45**:13244, 1992. 24, 54, 62
- [51] J. P. PERDEW, K. BURKE, AND M. ERNZERHOF. **Generalized gradient approximation made simple**. *Physical Review Letters*, **77**:3865, 1996. 24
- [52] Y. ZHANG AND W. YANG. **Comment on “generalized gradient approximation made simple”**. *Physical Review Letters*, **80**:890, 1998. 24
- [53] B. HAMMER, L. B. HANSEN, AND J. K. NØRSKOV. **Improved adsorption energetics within density-functional theory using revised Perdew-Burke-Ernzerhof functionals**. *Physical Review B*, **59**:7413, 1999. 24
- [54] J. P. PERDEW, A. RUZSINSZKY, G. I. CSONKA, O. A. VYDROV, G. E. SCUSERIA, L. A. CONSTANTIN, X. ZHOU, AND K. BURKE. **Restoring the density-gradient expansion for exchange in solids and surfaces**. *Physical Review Letters*, **100**:136406, 2008. 24
- [55] J. TAO, J. P. PERDEW, V. N. STAROVEROV, AND G. E. SCUSERIA. **Climbing the density functional ladder: Nonempirical meta-generalized gradient approximation designed for molecules and solids**. *Physical Review Letters*, **91**:146401, 2003. 25
- [56] A. D. BECKE. **Density-functional thermochemistry. III. The role of exact exchange**. *The Journal of Chemical Physics*, **98**(7):5648, 1993. 26
- [57] J. P. PERDEW, M. ERNZERHOF, AND K. BURKE. **Rationale for mixing exact exchange with density functional approximations**. *The Journal of Chemical Physics*, **105**(22):9982, 1996. 26
- [58] J. HEYD, G. E. SCUSERIA, AND M. ERNZERHOF. **Hybrid functionals based on a screened Coulomb potential**. *The Journal of Chemical Physics*, **118**(18):8207, 2003. 26
- [59] J. C. PHILLIPS. **Energy-band interpolation scheme based on a pseudopotential**. *Physical Review*, **112**:685, 1958. 30

REFERENCES

- [60] D. VANDERBILT. **Soft self-consistent pseudopotentials in a generalized eigenvalue formalism.** *Physical Review B*, **41**:7892, 1990. 30
- [61] P. E. BLÖCHL. **Projector augmented-wave method.** *Physical Review B*, **50**:17953, 1994. 30, 54, 62
- [62] G. KRESSE AND D. JOUBERT. **From ultrasoft pseudopotentials to the projector augmented-wave method.** *Physical Review B*, **59**:1758, 1999. 30, 54, 62
- [63] J. RATH AND A. J. FREEMAN. **Generalized magnetic susceptibilities in metals: Application of the analytic tetrahedron linear energy method to Sc.** *Physical Review B*, **11**:2109, 1975. 33
- [64] H. J. MONKHORST AND J. D. PACK. **Special points for Brillouin-zone integrations.** *Physical Review B*, **13**:5188, 1976. 33, 54, 62
- [65] K. SCHWARZ, P. BLAHA, AND G.K.H. MADSEN. **Electronic structure calculations of solids using the WIEN2k package for material sciences.** *Computer Physics Communications*, **147**(1-2):71, 2002. 34
- [66] M. J. FRISCH, G. W. TRUCKS, AND SCHLEGEL ET AL. **Gaussian 03, Revision C.02,** 2004. 34
- [67] J. SOLER, E. ARTACHO, J. D. GALE, A. GARCÍA, J. JUNQUERA, P. ORDEJÓN, AND D. SÁNCHEZ-PORTAL. **The SIESTA method for ab initio order- N materials simulation.** *Journal of Physics: Condensed Matter*, **14**(11):2745, 2002. 34
- [68] M. D. SEGALL, P. J. D. LINDAN, M. J. PROBERT, C. J. PICKARD, P. J. HASNIP, S. J. CLARK, AND M. C. PAYNE. **First-principles simulation: Ideas, illustrations and the CASTEP code.** *Journal of Physics: Condensed Matter*, **14**(11):2717, 2002. 34
- [69] G. KRESSE AND J. HAFNER. **Ab-initio molecular dynamics for liquid metals.** *Physical Review B*, **47**:558, 1993. 34, 54, 62
- [70] G. KRESSE AND J. FURTHMÜLLER. **Efficient iterative schemes for ab-initio total-energy calculations using a plane-wave basis set.** *Physical Review B*, **54**:11169, 1996.
- [71] G. KRESSE AND J. HAFNER. **Norm-conserving and ultrasoft pseudopotentials for first-row and transition elements.** *Journal of Physics: Condensed Matter*, **6**(40):8245, 1994.
- [72] G. KRESSE AND J. FURTHMÜLLER. **Efficiency of ab-initio total energy calculations for metals and semiconductors using a plane-wave basis set.** *Computational Materials Science*, **6**(1):15, 1996. 34, 54, 62

- [73] D. D. JOHNSON. **Modified Broyden's method for accelerating convergence in self-consistent calculations.** *Physical Review B*, **38**:12807, 1988. 35
- [74] P. PULAY. **Convergence acceleration of iterative sequences. The case of scf iteration.** *Chemical Physics Letters*, **73**(2):393, 1980. 35
- [75] O. DEUTSCHMANN. *Modeling and Simulation of Heterogeneous Catalytic Reactions: From the Molecular Process to the Technical System.* Wiley-VCH Verlag GmbH & Co. KGaA, 2011. 37, 38
- [76] G. J. KROES. **Frontiers in surface scattering simulations.** *Science*, **321**(5890):794, 2008. 37
- [77] H. F. BUSNENGO, A. SALIN, AND W. DONG. **Representation of the 6D potential energy surface for a diatomic molecule near a solid surface.** *The Journal of Chemical Physics*, **112**(17):7641, 2000. 39, 64
- [78] R. A. OLSEN, H. F. BUSNENGO, A. SALIN, M. F. SOMERS, G. J. KROES, AND E. J. BAERENDS. **Constructing accurate potential energy surfaces for a diatomic molecule interacting with a solid surface: $\text{H}_2+\text{Pt}(111)$ and $\text{H}_2+\text{Cu}(100)$.** *The Journal of Chemical Physics*, **116**(9):3841, 2002. 39
- [79] M. A. DI CESARE, H. F. BUSNENGO, W. DONG, AND A. SALIN. **Role of dynamic trapping in H_2 dissociation and reflection on Pd surfaces.** *The Journal of Chemical Physics*, **118**(24):11226, 2003.
- [80] G. VOLPILHAC, H. F. BUSNENGO, W. DONG, AND A. SALIN. **Scattering of atomic nitrogen on $\text{W}(100)$.** *Surface Science*, **544**(2-3):329, 2003.
- [81] C. DÍAZ, R. A. OLSEN, H. F. BUSNENGO, AND G. J. KROES. **Dynamics on six-dimensional potential energy surfaces for $\text{H}_2/\text{Cu}(111)$: Corrugation reducing procedure versus modified shepard interpolation method and PW91 versus RPBE.** *The Journal of Physical Chemistry C*, **114**(25):11192, 2010. 39
- [82] F. LONDON. **Quantenmechanische Deutung Des Vorgangs der Aktivierung.** *Zeitschrift für Elektrochemie und angewandte physikalische Chemie*, **35**(9):552, 1929. 42
- [83] H. EYRING AND M. POLANYI. **On simple gas reactions.** *Zeitschrift für Physikalische Chemie*, **227**(9):1221, 2013. 42
- [84] S. SATO. **Potential energy surface of the system of three atoms.** *The Journal of Chemical Physics*, **23**(12):2465, 1955. 42
- [85] J. H. MCCREERY AND G. WOLKEN. **A model potential for chemisorption: $\text{H}_2+\text{W}(001)$.** *The Journal of Chemical Physics*, **63**(6):2340, 1975. 42

REFERENCES

- [86] J. H. MCCREERY AND G. WOLKEN. **Atomic recombination dynamics on a solid surface: $\text{H}_2 + \text{W}(001)$** . *The Journal of Chemical Physics*, **64**(7):2845, 1976. 42
- [87] J. H. MCCREERY AND G. WOLKEN. **Dynamics of adsorption: Model calculations for several interaction potentials**. *The Journal of Chemical Physics*, **65**(4):1310, 1976. 42
- [88] S. CARATZOULAS, B. JACKSON, AND M. PERSSON. **Eley-Rideal and Hot-Atom reaction dynamics of $\text{H}(\text{g})$ with H adsorbed on $\text{Cu}(111)$** . *The Journal of Chemical Physics*, **107**(16):6420, 1997. 43, 100, 103
- [89] Z. B. GUVENC, X. SHA, AND B. JACKSON. **Eley-Rideal and hot atom reactions between hydrogen atoms on $\text{Ni}(100)$: Electronic structure and quassi-classical studies**. *The Journal of Chemical Physics*, **115**(19):9018, 2001. 43
- [90] D. LEMOINE, J. G. QUATTRUCCI, AND B. JACKSON. **Efficient Eley-Rideal reactions of H atoms with single Cl adsorbates on $\text{Au}(111)$** . *Physical Review Letters*, **89**:268302, 2002. 43
- [91] Z. B. GUVENC, X. SHA, AND B. JACKSON. **The Effects of lattice motion on Eley-Rideal and Hot-Atom reactions: Quasi-classical studies of Hydrogen recombination on $\text{Ni}(100)$** . *The Journal of Physical Chemistry B*, **106**(33):8342, 2002. 44
- [92] L. MARTIN-GONDRE, C. CRESPOS, P. LARRÉGARAY, J.C. RAYEZ, D. CONTE, AND B. VAN OOTEGEM. **Detailed description of the flexible periodic London-Eyring-Polanyi-Sato potential energy function**. *Chemical Physics*, **367**(2-3):136, 2010. 44, 100
- [93] L. MARTIN-GONDRE, C. CRESPOS, P. LARRÉGARAY, J.C. RAYEZ, B. VAN OOTEGEM, AND D. CONTE. **Is the LEPS potential accurate enough to investigate the dissociation of diatomic molecules on surfaces?** *Chemical Physics Letters*, **471**(1-3):136, 2009. 44
- [94] L. MARTIN-GONDRE, C. CRESPOS, P. LARRÉGARAY, J.C. RAYEZ, B. VAN OOTEGEM, AND D. CONTE. **Dynamics simulation of N_2 scattering onto $\text{W}(100,110)$ surfaces: A stringent test for the recently developed flexible periodic London-Eyring-Polanyi-Sato potential energy surface**. *The Journal of Chemical Physics*, **132**(20):204501, 2010. 44, 100
- [95] R. PÉTUYA, C. CRESPOS, E. QUINTAS-SÁNCHEZ, AND P. LARRÉGARAY. **Comparative theoretical study of H_2 Eley-Rideal recombination dynamics on $\text{W}(100)$ and $\text{W}(110)$** . *The Journal of Physical Chemistry C*, **118**(22):11704, 2014. 45, 100, 101, 103

-
- [96] R. PÉTUYA, P. LARRÉGARAY, C. CRESPOS, P. AUREL, H. F. BUSNENGO, AND A. E. MARTÍNEZ. **Scattering of atomic Hydrogen off a H-covered W(110) surface: Hot-Atom versus Eley-Rideal abstraction dynamics.** *The Journal of Physical Chemistry C*, **119**(6):3171, 2015. 45, 102, 108
- [97] G. R. DARLING AND S. HOLLOWAY. **The dissociation of diatomic molecules at surfaces.** *Reports on Progress in Physics*, **58**(12):1595, 1995. 45
- [98] A. GROSS. **Reactions at surfaces studied by ab initio dynamics calculations.** *Surface Science Reports*, **32**(8):291, 1998.
- [99] G. J. KROES. **Six-dimensional quantum dynamics of dissociative chemisorption of H₂ on metal surfaces.** *Progress in Surface Science*, **60**(1-4):1, 1999. 85
- [100] J. STOER AND R. BULIRSCH. *Introduction to Numerical Analysis*. Springer, 1980. 46
- [101] S. A. ADELMAN AND J. D. DOLL. **Generalized Langevin equation approach for atom/solid-surface scattering: General formulation for classical scattering off harmonic solids.** *The Journal of Chemical Physics*, **64**(6):2375, 1976. 46, 78, 101
- [102] J. C. TULLY. **Dynamics of gas-surface interactions: 3D generalized Langevin model applied to fcc and bcc surfaces.** *The Journal of Chemical Physics*, **73**(4):1975, 1980. 48
- [103] H. F. BUSNENGO, M. A. DI CÉSARE, W. DONG, AND A. SALIN. **Surface temperature effects in dynamic trapping mediated adsorption of light molecules on metal surfaces: H₂ on Pd(111) and Pd(110).** *Physical Review B*, **72**:125411, 2005. 46, 48, 78, 80, 91, 101
- [104] H. F. BUSNENGO, W. DONG, AND A. SALIN. **Trapping, molecular Adsorption, and precursors for nonactivated chemisorption.** *Physical Review Letters*, **93**:236103, 2004. 47
- [105] J. I. JUARISTI, M. ALDUCIN, R. DÍEZ MUIÑO, H. F. BUSNENGO, AND A. SALIN. **Role of electron-hole pair excitations in the dissociative adsorption of diatomic molecules on metal surfaces.** *Physical Review Letters*, **100**:116102, 2008. 48
- [106] H. F. BUSNENGO AND A. E. MARTÍNEZ. **H₂ chemisorption on W(100) and W(110) surfaces.** *The Journal of Physical Chemistry C*, **112**(14):5579, 2008. 49
- [107] K. O. LEGG, F. JONA, D. W. JEPSEN, AND P. M. MARCUS. **Low-energy electron diffraction analysis of clean Fe (001).** *Journal of Physics C: Solid State Physics*, **10**(7):937, 1977. 53
- [108] H. D. SHIH, F. JONA, U. BARDI, AND P. M. MARCUS. **The atomic structure of Fe(110).** *Journal of Physics C: Solid State Physics*, **13**(19):3801, 1980.

REFERENCES

- [109] H.D. SHIH, F. JONA, D.W. JEPSEN, AND P.M. MARCUS. **Atomic structure of Fe (111)**. *Surface Science*, **104**(1):39, 1981. 53, 56
- [110] R. N. BARNETT, U. LANDMAN, AND C. L. CLEVELAND. **Multilayer lattice relaxation at metal surfaces**. *Physical Review B*, **27**:6534, 1983. 53
- [111] P. JIANG, P. M. MARCUS, AND F. JONA. **Relaxation at clean metal surfaces**. *Solid State Communications*, **59**(5):275, 1986. 53
- [112] M. J. S. SPENCER, A. HUNG, I. K. SNOOK, AND I. YAROVSKY. **Density functional theory study of the relaxation and energy of iron surfaces**. *Surface Science*, **513**(2):389, 2002. 53, 56, 57, 58
- [113] P. BŁOŃSKI AND A. KIEJNA. **Calculation of surface properties of bcc iron**. *Vacuum*, **74**(2):179, 2004. 58
- [114] P. BŁOŃSKI AND A. KIEJNA. **Structural, electronic, and magnetic properties of bcc iron surfaces**. *Surface Science*, **601**(1):123, 2007. 56, 57, 58
- [115] J. SOKOLOV, F. JONA, AND P. M. MARCUS. **Multilayer relaxation of a clean bcc Fe111 surface**. *Physical Review B*, **33**:1397, 1986. 57, 58
- [116] C. XU AND D. J. O'CONNOR. **Fe(111) surface relaxation analysis by in- and out-of-plane MEIS**. *Nuclear Instruments and Methods in Physics Research Section B: Beam Interactions with Materials and Atoms*, **51**(3):278, 1990. 57, 58
- [117] S. M. YALISOVE AND W. R. GRAHAM. **Medium energy ion scattering studies of relaxation at metal surfaces**. *Journal of Vacuum Science & Technology A*, **6**(3):588, 1988. 53, 57, 58
- [118] J. P. PERDEW, J. A. CHEVARY, S. H. VOSKO, K. A. JACKSON, M. R. PEDERSON, D. J. SINGH, AND C. FIOUHAIS. **Atoms, molecules, solids, and surfaces: Applications of the generalized gradient approximation for exchange and correlation**. *Physical Review B*, **46**:6671, 1992. 54, 62
- [119] S. R. HALL B. MCMAHON (EDS.) S. R. HALL, B. MCMAHON (AUTH.). *International Tables for Crystallography Volume G: Definition and Exchange of Crystallographic Data*. International Tables for Crystallography G. Springer Netherlands, 2005. 55, 56
- [120] C. KITTEL. *Introduction to Solid State Physics*. John Wiley & Sons, Inc., New York, 8th edition, 2004. 55, 56
- [121] B. MEDASANI, M. HARANCZYK, A. CANNING, AND M. ASTA. **Vacancy formation energies in metals: A comparison of MetaGGA with LDA and GGA exchange-correlation functionals**. *Computational Materials Science*, **101**:96, 2015. 55, 56

-
- [122] D. P. JACKSON. **Surface relaxations in cubic metals.** *Canadian Journal of Physics*, **49**(16):2093, 1971. 56
- [123] M. W. FINNIS AND V. HEINE. **Theory of lattice contraction at aluminium surfaces.** *Journal of Physics F: Metal Physics*, **4**(3):L37, 1974. 56
- [124] F. BOZSO, G. ERTL, M. GRUNZE, AND M. WEISS. **Interaction of nitrogen with iron surfaces.** *Journal of Catalysis*, **49**(1):18, 1977. 62, 63, 72, 78, 85, 87, 93, 97
- [125] M. GRUNZE, G. STRASSER, AND M. GOLZE. **Precursor mediated and direct adsorption of molecular nitrogen on Fe(111).** *Applied Physics A*, **44**(1):19, 1987. 62, 72, 78, 85, 87, 92, 93
- [126] J. J. MORTENSEN, M. V. GANDUGLIA-PIROVANO, L. B. HANSEN, B. HAMMER, P. STOLTZE, AND J. K. NØRSKOV. **Nitrogen adsorption on Fe(111), (100), and (110) surfaces.** *Surface Science*, **422**(1--3):8, 1999. 63
- [127] S. RIIKONEN, A. S. FOSTER, A. V. KRASHENINNIKOV, AND R. M. NIEMINEN. **Computational study of boron nitride nanotube synthesis: How catalyst morphology stabilizes the boron nitride bond.** *Physical Review B*, **80**:155429, 2009.
- [128] I. GOIKOETXEA, M. ALDUCIN, R. DÍEZ MUIÑO, AND J. I. JUARISTI. **Dissociative and non-dissociative adsorption dynamics of N₂ on Fe(110).** *Physical Chemistry Chemical Physics*, **14**:7471, 2012. 70, 87, 96
- [129] I. GOIKOETXEA, J. I. JUARISTI, R. DÍEZ MUIÑO, AND M. ALDUCIN. **Surface strain improves molecular adsorption but hampers dissociation for N₂ on the Fe/W(110) surface.** *Physical Review Letters*, **113**:066103, 2014.
- [130] I. GOIKOETXEA, M. ALDUCIN, R. DÍEZ MUIÑO, AND J. I. JUARISTI. **The dynamics of adsorption and dissociation of N₂ in a monolayer of iron on W(110).** *Physical Chemistry Chemical Physics*, **17**:19432, 2015.
- [131] S. PICK, P. LÉGARÉ, AND C. DEMANGEAT. **Density-functional study of the chemisorption of N on and below Fe(110) and Fe(001) surfaces.** *Physical Review B*, **75**:195446, 2007. 63
- [132] F. BOZSO, G. ERTL, AND M. WEISS. **Interaction of nitrogen with iron surfaces.** *Journal of Catalysis*, **50**(3):519, 1977. 63
- [133] G. ERTL, S. B. LEE, AND M. WEISS. **Kinetics of nitrogen adsorption on Fe(111).** *Surface Science*, **114**(2):515, 1982. 63, 72, 78, 79, 82, 85, 87, 92, 93
- [134] J. J. MORTENSEN, L. B. HANSEN, B. HAMMER, AND J. K. NØRSKOV. **Nitrogen adsorption and dissociation on Fe(111).** *Journal of Catalysis*, **182**(2):479, 1999. 65, 72, 78, 85

REFERENCES

- [135] M. GRUNZE, M. GOLZE, W. HIRSCHWALD, H. J. FREUND, H. PULM, U. SEIP, M. C. TSAI, G. ERTL, AND J. KÜPPERS. **π -Bonded N_2 on Fe(111): The precursor for dissociation.** *Physical Review Letters*, **53**:850, 1984. 72, 78, 82, 87, 92
- [136] M. C. TSAI, U. SHIP, I. C. BASSIGNANA, J. KÜPPERS, AND G. ERTL. **A vibrational spectroscopy study on the interaction of N_2 with clean and K-promoted Fe(111) surfaces: π -bonded dinitrogen as precursor for dissociation.** *Surface Science*, **155**(2):387, 1985. 87
- [137] L. J. WHITMAN, C. E. BARTOSCH, W. HO, G. STRASSER, AND M. GRUNZE. **Alkali-metal promotion of a dissociation precursor: N_2 on Fe(111).** *Physical Review Letters*, **56**:1984, 1986.
- [138] H. J. FREUND, B. BARTOS, R. P. MESSMER, H. GRUNZE, H. KUHLENBECK, AND M. NEUMANN. **The adsorption of N_2 on Fe(111): Angle resolved photoemission and theoretical model studies.** *Surface Science*, **185**(1):187, 1987. 72, 78, 82, 87, 92
- [139] D. TOMÁNEK AND K. H. BENNEMANN. **Total-energy calculations for N_2 dissociation on Fe(111): Characterization of precursor and dissociative states.** *Physical Review B*, **31**:2488, 1985. 72, 85
- [140] T. PANCZYK. **Comparative analysis of nitrogen adsorption kinetics on Fe(100) and Fe(111) based on applying the statistical rate theory.** *The Journal of Physical Chemistry C*, **111**(7):3175, 2007.
- [141] T. WANG, X. TIAN, Y. YANG, Y. W. LI, J. WANG, M. BELLER, AND H. JIAO. **Coverage-dependent N_2 adsorption and its modification of iron surfaces structures.** *The Journal of Physical Chemistry C*, **120**(5):2846, 2016. 72
- [142] C. DÍAZ, J. K. VINCENT, G. P. KRISHNAMOHAN, R. A. OLSEN, G. J. KROES, K. HONKALA, AND J. K. NØRSKOV. **Multidimensional effects on dissociation of N_2 on Ru(0001).** *Physical Review Letters*, **96**:096102, 2006. 74, 77
- [143] A. GROSS AND M. SCHEFFLER. ***Ab initio* quantum and molecular dynamics of the dissociative adsorption of hydrogen on Pd(100).** *Physical Review B*, **57**:2493, 1998. 74, 77
- [144] L. MARTIN-GONDRE, G.A. BOCAN, M. ALDUCIN, J.I. JUARISTI, AND R. DÍEZ MUIÑO. **Energy dissipation channels in the adsorption of N on Ag(111).** *Computational and Theoretical Chemistry*, **990**:126, 2012. 78, 100, 119
- [145] L. J. WHITMAN, C. E. BARTOSCH, AND W. HO. **A new mechanism for K promotion of surface reactions: N_2 on K-precovered Fe(111).** *The Journal of Chemical Physics*, **85**(6):3688, 1986. 87, 92

-
- [146] G. ERTL. **Surface science and catalysis-studies on the mechanism of ammonia Synthesis: The P. H. Emmett Award Address.** *Catalysis Reviews*, **21**(2):201, 1980. 97
- [147] D.R. STRONGIN, J. CARRAZZA, SIMON R. BARE, AND G.A. SOMORJAI. **The importance of C7 sites and surface roughness in the ammonia synthesis reaction over iron.** *Journal of Catalysis*, **103**(1):213, 1987. 97
- [148] A. W. KLEYN, N. J. LOPES CARDOZO, AND U. SAMM. **Plasma-surface interaction in the context of ITER.** *Physical Chemistry Chemical Physics*, **8**:1761, 2006. 99
- [149] J. ROTH, E. TSITRONE, A. LOARTE, TH. LOARER, G. COUNSELL, R. NEU, V. PHILIPPS, S. BREZINSEK, M. LEHNEN, P. COAD, CH. GRISOLIA, K. SCHMID, K. KRIEGER, A. KALLENBACH, B. LIPSCHULTZ, R. DOERNER, R. CAUSEY, V. ALIMOV, W. SHU, O. OGORODNIKOVA, A. KIRSCHNER, G. FEDERICI, AND A. KUKUSHKIN. **Recent analysis of key plasma wall interactions issues for ITER.** *Journal of Nuclear Materials*, **390-391**:1, 2009. 100
- [150] M. H. J. 'T HOEN, M. MAYER, A. W. KLEYN, AND P. A. Z. VAN EMMICHOVEN. **Strongly reduced penetration of atomic deuterium in radiation-damaged tungsten.** *Physical Review Letters*, **111**:225001, 2013.
- [151] M. JIMENEZ-REDONDO, E. CARRASCO, V. J. HERRERO, AND I. TANARRO. **Isotopic exchange processes in cold plasmas of H₂/D₂ mixtures.** *Physical Chemistry Chemical Physics*, **13**:9655, 2011. 99
- [152] C. T. RETTNER. **Dynamics of the direct reaction of hydrogen atoms adsorbed on Cu(111) with hydrogen atoms incident from the gas-phase.** *Physical Review Letters*, **69**:383, 1992. 99, 100, 108
- [153] C. T. RETTNER AND D. J. AUERBACH. **Dynamics of the Eley-Rideal Reaction of D Atoms with H Atoms Adsorbed on Cu(111): Vibrational and Rotational State Distributions of the HD Product.** *Physical Review Letters*, **74**:4551, 1995. 99, 108
- [154] M. PERSSON AND B. JACKSON. **Isotope effects in the Eley-Rideal dynamics of the recombinative desorption of hydrogen on a metal surface.** *Chemical Physics Letters*, **237**(5):468, 1995. 100, 105
- [155] M. PERSSON AND B. JACKSON. **Flat surface study of the Eley-Rideal dynamics of recombinative desorption of hydrogen on a metal surface.** *The Journal of Chemical Physics*, **102**(2):1078, 1995.
- [156] B. JACKSON AND M. PERSSON. **Effects of isotopic substitution on Eley-Rideal reactions and adsorbate-mediated trapping.** *The Journal of Chemical Physics*, **103**(14):6257, 1995. 100, 101, 103, 108

REFERENCES

- [157] M. BLANCO-REY, E. DÍAZ, G. A. BOCAN, R. DÍEZ MUIÑO, M. ALDUCIN, AND J. I. JUARISTI. **Efficient N₂ formation on Ag(111) by Eley-Rideal recombination of hyperthermal atoms.** *The Journal of Physical Chemistry Letters*, **4**(21):3704, 2013. 100, 119
- [158] T. ZAHARIA, A. W. KLEYN, AND M. A. GLEESON. **Eley-Rideal reactions with N atoms at Ru(0001): Formation of NO and N₂.** *Physical Review Letters*, **113**:053201, 2014. 100
- [159] E. QUINTAS-SÁNCHEZ, P. LARRÉGARAY, C. CRESPOS, L. MARTIN-GONDRE, J. RUBAYO-SONEIRA, AND J.-C. RAYEZ. **Dynamical reaction pathways in Eley-Rideal recombination of nitrogen from W(100).** *The Journal of Chemical Physics*, **137**(6):064709, 2012. 100, 105
- [160] E. QUINTAS-SÁNCHEZ, C. CRESPOS, P. LARRÉGARAY, J. C. RAYEZ, L. MARTIN-GONDRE, AND J. RUBAYO-SONEIRA. **Surface temperature effects on the dynamics of N₂ Eley-Rideal recombination on W(100).** *The Journal of Chemical Physics*, **138**(2):024706, 2013.
- [161] E. QUINTAS-SÁNCHEZ, P. LARRÉGARAY, AND C. CRESPOS. **Influence of Surface Symmetry on the Onset of Nitrogen Eley-Rideal Recombination on Tungsten.** *The Journal of Physical Chemistry C*, **118**(23):12224, 2014. 100
- [162] B. JACKSON AND M. PERSSON. **A quantum mechanical study of recombinative desorption of atomic hydrogen on a metal surface.** *The Journal of Chemical Physics*, **96**(3):2378, 1992. 100, 105
- [163] C. T. RETTNER AND D. J. AUERBACH. **Quantum-state distributions for the HD product of the direct reaction of H(D)/Cu(111) with D(H) incident from the gas-phase.** *The Journal of Chemical Physics*, **104**(7):2732, 1996. 108
- [164] TH. KAMMLER, J. LEE, AND J. KÜPPERS. **A kinetic study of the interaction of gaseous H(D) atoms with D(H) adsorbed on Ni(100) surfaces.** *The Journal of Chemical Physics*, **106**(17):7362, 1997.
- [165] J. DAI AND J. C. LIGHT. **Quantum dynamics of an Eley-Rideal gas-surface reaction: Four dimensional planar model for H(D)(gas)+D(H)-Cu(111).** *The Journal of Chemical Physics*, **110**(13):6511, 1999. 100, 105
- [166] R. PÉTUYA, P. LARRÉGARAY, C. CRESPOS, H. F. BUSNENGO, AND A. E. MARTÍNEZ. **Dynamics of H₂ Eley-Rideal abstraction from W(110): Sensitivity to the representation of the molecule-surface potential.** *The Journal of Chemical Physics*, **141**(2):024701, 2014. 100

-
- [167] J. STRÖMQUIST, L. BENGTSSON, M. PERSSON, AND B. HAMMER. **The dynamics of H absorption in and adsorption on Cu(111)**. *Surface Science*, **397**(1):382, 1998. 100
- [168] B. JACKSON AND D. LEMOINE. **Eley-Rideal reactions between H atoms on metal and graphite surfaces: The variation of reactivity with substrate**. *The Journal of Chemical Physics*, **114**(1):474, 2001. 103
- [169] R. MARTINAZZO, S. ASSONI, G. MARINONI, AND G. F. TANTARDINI. **Hot-Atom versus Eley-Rideal dynamics in hydrogen recombination on Ni(100). I. The single-adsorbate case**. *The Journal of Chemical Physics*, **120**(18):8761, 2004. 103
- [170] D. V. SHALASHILIN, B. JACKSON, AND M. PERSSON. **Eley-Rideal and Hot-Atom dynamics of HD formation by H(D) incident from the gas-phase on D(H)-covered Cu(111)**. *Faraday Discuss.*, **110**:287, 1998. 105
- [171] S. MARKELJ AND I. ADE. **Production of vibrationally excited hydrogen molecules by atom recombination on Cu and W materials**. *The Journal of Chemical Physics*, **134**(12):124707, 2011. 108, 112
- [172] M. RAMOS, M. MINNITI, C. DÍAZ, D. FARIAS, R. MIRANDA, F. MARTIN, A. E. MARTINEZ, AND H. F. BUSNENGO. **Environment-driven reactivity of H₂ on PdRu surface alloys**. *Physical Chemistry Chemical Physics*, **15**:14936, 2013. 108
- [173] M. S. GRAVIELLE, G. A. BOCAN, AND R. DÍEZ MUIÑO. **Diffraction of swift atoms after grazing scattering from metal surfaces: N/Ag(111) system**. *Physical Review A*, **82**:052904, 2010. 119

Resumen

La ciencia de superficies es una disciplina científica difícil pero al tiempo fascinante, por muchas razones. Aparece en la frontera entre distintas fases de la materia, pero también puede verse como un punto de encuentro entre la física de materia condensada y la química. Además, existen muchos ejemplos que involucran superficies en nuestra vida diaria. Por ejemplo, la corrosión de una moneda es debida a la interacción entre el oxígeno en el aire y la superficie metálica de la moneda. Los catalizadores instalados en los coches están basados en los procesos reactivos en superficies de distintas moléculas tóxicas que se recombinan y transforman en otros compuestos menos dañinos. La ciencia de superficies es, por tanto, capaz de explicar muchos aspectos distintos de nuestra vida. Industrialmente, el progreso en la comprensión de las interacciones entre moléculas y superficies tiene aplicaciones en ámbitos de gran importancia económica, como el almacenamiento de hidrógeno, los dispositivos basados en semiconductores, los dispositivos de diagnóstico o tratamiento médico, o la catálisis heterogénea. En este último campo, la ciencia de superficies tiene una enorme importancia práctica. Aproximadamente el 85-90 % de los procesos químicos industriales actuales están relacionado con la catálisis. Entre estos procesos, uno de los más importantes es la síntesis del amoníaco, a partir de la cual se producen más de 160 millones de toneladas de este producto anualmente. Es por ello por lo que la síntesis del amoníaco puede ser considerada como uno de los procesos más atractivos, tanto para la investigación científica como para las aplicaciones tecnológicas. El amoníaco se produce habitualmente mediante la interacción de moléculas de hidrógeno y moléculas de nitrógeno en catalizadores basados en hierro (Fe) o rutenio (Ru). En las últimas décadas, se ha dedicado mucho esfuerzo a mejorar el diseño de los reactores en que se producen estas reacciones y a comprender en mayor detalle la naturaleza del proceso catalítico y sus reacciones asociadas. En

relación con estas últimas, merece la pena mencionar que los procesos reactivos elementales en superficies son fenómenos muy complejos, que pueden depender mucho de pequeños detalles de la interacción electrónica. En el caso particular de la formación de amoníaco en superficies, el paso clave que pone límites a la formación de esta molécula es la disociación de la molécula de nitrógeno en la superficie.

La descripción teórica de los procesos físico-químicos en superficies es uno de los temas más importantes de la ciencia de superficies. Además de su importancia en la comprensión profunda de la información experimental, puede ser muy útil para reducir el número de intentos fallidos en distintos experimentos. Una de las mayores ventajas de la aproximación teórica al problema es que puede y debe proporcionar predicciones sobre tendencias generales en los procesos. Gracias a la significativa diferencia entre la masa de las moléculas en los procesos de interés en el presente manuscrito y los átomos de la superficie, una de las aproximaciones más útiles en la descripción de procesos físico-químicos en superficies es la aproximación de Born-Oppenheimer con una superficie estática (BOSS, por sus siglas en inglés: ‘Born-Oppenheimer static surface’). Dentro de la aproximación BOSS, se pueden realizar cálculos de estructura electrónica para definir el panorama energético del sistema, uno de los primeros pasos en una descripción adiabática de los procesos. La teoría del funcional de la densidad (DFT, ‘density functional theory’) es uno de los modelos teóricos más habituales para el cálculo de las estructuras de equilibrio, las energías de adsorción, los caminos de reacción, o las barreras de activación en distintos procesos que aparecen en la ciencia de superficies. En combinación con los cálculos de estructura electrónica, hay distintos métodos de interpolación que han sido concebidos y aplicados para construir representaciones de las superficies de energía potencial que contemplan todos los grados de libertad de los sistemas que se pretende estudiar. A partir de estos mapas globales de energía, se pueden realizar simulaciones de dinámica molecular para analizar la dinámica de los distintos procesos. Una aproximación muy útil en este nivel es permanecer al nivel de la dinámica clásica, en la que las trayectorias clásicas se obtienen a partir de la integración de las ecuaciones clásicas de movimiento. Promediando sobre todas las posibles configuraciones iniciales, se puede obtener así información estadística sobre las probabilidades individuales de reacción. En la descripción de procesos macroscópicos, como aquellos que tienen lugar en los reactores químicos experimentales, son necesarios modelos estadísticos más generales, en los que las probabilidades de reacción de los

distintos procesos se toman como información de entrada.

En este trabajo de tesis presento un estudio teórico de la interacción entre moléculas de nitrógeno, N_2 , y superficies de hierro Fe(111). Además, he estudiado también los efectos isotópicos en la dinámica reaccional del átomo de hidrógeno y sus isótopos en las superficies de tungsteno W(100) y W(110). He descrito los procesos reactivos elementales aplicando distintas metodologías teóricas. En primer lugar, la teoría DFT ha servido para obtener una descripción cuantitativa de la geometría y energía de los reactantes. A partir de ahí, he combinado la descripción cuantitativa a nivel atómico, basada en DFT, con métodos termodinámicos y estadísticos para calcular las probabilidades de reacción de los distintos procesos.

Desde el punto de vista teórico, en el manuscrito presento una introducción de la metodología DFT independiente del tiempo, además de una descripción de su implementación para cálculos de estructura electrónica. Incluyo también una visión detallada de los métodos de interpolación que he utilizado para construir las superficies de energía potencial (PES, ‘potential energy surfaces’) que describen la energía de los sistemas estudiados. Por fin, añado también una visión general del método utilizado para realizar los cálculos de dinámica clásica.

En el estudio de las propiedades estructurales de la superficie de Fe(111), hemos realizado cálculos DFT para estudiar las propiedades del hierro sólido, así como la relajación estructural de las capas más externas de la superficie. Nuestros resultados para el módulo de bulk o la constante de red presentan un buen acuerdo con los resultados experimentales. Las capas cercanas a la superficie se relajan tan solo en la dirección perpendicular a la superficie y no se observa reconstrucción. Las distancias intercapa se reducen en sus dos primeros valores (entre la primera y segunda capa y entre la segunda y tercera capa) mientras que la tercera distancia intercapa (entre la tercera y cuarta capa) aumenta. Nuestros resultados muestran que estas relajaciones no dependen del número de capas considerado en el sistema. Las relajaciones intercapa muestran un acuerdo cualitativo, aun con algunas diferencias cuantitativas, con las medidas experimentales. Mostramos también que el valor de la energía de interacción de la molécula de nitrógeno con la superficie de Fe(111) no depende del número de capas considerado en el sistema.

Posteriormente, aplicamos la aproximación de superficie congelada a un sistema compuesto de nueve capas de átomos de hierro, que representa la superficie de Fe(111), para

plantear el cálculo de la dinámica de reacción de átomos y moléculas de nitrógeno sobre esta superficie. En primer lugar, realizamos cálculos DFT para el nitrógeno atómico aproximándose en una dirección perpendicular a varios sitios de alta simetría de la superficie de Fe(111). La posición atómica preferida para la adsorción atómica es la denominada hollow, con una energía de adsorción consistente con aquella encontrada en estudios previos de la interacción de átomos de nitrógeno con superficies de Fe(111). Después, creamos una red de puntos mediante cálculos DFT que describen la interacción de una molécula de N_2 en distintas posiciones y distintas configuraciones con la superficie de Fe(111), teniendo en cuenta los seis grados de libertad de la molécula. A partir de aquí, construimos las superficies de energía potencial tridimensionales (3D) y hexadimensionales (6D) que describen la interacción de nitrógeno atómico y molecular respectivamente con la superficie de hierro, mediante la interpolación de la red de puntos DFT utilizando el método de la reducción de la corrugación (CRP, ‘corrugation reducing procedure’). La comparación de los resultados de la interpolación con las energías DFT muestra la enorme eficacia del método CRP como herramienta de interpolación. Un análisis sistemático de la PES-6D muestra que hay cuatro mínimos locales de adsorción de la molécula de N_2 sobre Fe(111). A la distancia de equilibrio internuclear de la molécula, hay dos estados de adsorción con el eje molecular orientado en dirección perpendicular a la superficie de hierro, con la molécula colocada justo encima de los átomos de hierro de la primera y segunda capa. Encontramos además dos estados de adsorción adicionales, con la distancia internuclear ligeramente aumentada, con el eje molecular colocado ahora en orientación paralela a la superficie y con la molécula situada en la posición hollow, en un caso, y encima de un átomo de hierro de la tercera capa, en el otro caso. Los estados de adsorción situados encima de los átomos de hierro de la primera, segunda y tercera capas se caracterizan por energías de adsorción levemente distintas. El pozo de adsorción más profundo en la PES-6D es el que corresponde a la posición hollow.

El estudio de la dinámica de adsorción del N_2 en la superficie de Fe(111) lo hemos realizado a partir de cálculos de trayectorias cuasiclásicas (QCT, ‘quasiclassical trajectories’), en un espectro muy amplio de energías de impacto y para varias temperaturas de la superficie. Nuestros cálculos QCT muestran la dependencia de la dinámica de adsorción molecular y de la probabilidad de adsorción con la temperatura de la superficie. El estudio detallado de la dinámica de adsorción muestra que la adsorción molecular

depende fundamentalmente del valor de la energía inicial de la molécula y de la magnitud de la barrera de entrada. Para energías muy bajas, la adsorción dominante es la que se produce en el pozo situado encima de los átomos de hierro de la primera capa atómica. El acceso a este estado de adsorción no presenta ninguna barrera energética y la probabilidad de adsorción molecular es cercana a la unidad. Cuando la energía inicial de la molécula aumenta, los canales de adsorción más importantes cambian. Así, son ahora la adsorción molecular al pozo situado en hollow, así como al pozo situado sobre los átomos de la tercera capa, los predominantes para energías más altas. El motivo es que el acceso a estos dos estados está controlado por dos pequeñas barreras de energía en el canal de entrada. En general, nuestros cálculos QCT confirman las ideas que habían sido propuestas anteriormente sobre la dinámica de la adsorción molecular de N_2 en Fe(111), a partir de medidas experimentales y cálculos teóricos estáticos.

Un paso más allá en el estudio de los procesos reactivos elementales de N_2 en Fe(111) es el estudio de la dinámica de adsorción disociativa, utilizando condiciones iniciales muy similares a las del caso anterior. Estudiamos, en este contexto, la dependencia de la probabilidad de adsorción disociativa con el ángulo de incidencia de las moléculas de N_2 . Para incidencia perpendicular y energías de impacto menores que 3eV, nuestros resultados teóricos están por debajo de los valores experimentales. El acuerdo, sin embargo, es mejor, si aumentamos la temperatura de la superficie para incentivar el paso a la disociación de moléculas que habían quedado previamente atrapadas en la superficie. Para energías más altas de la molécula incidente, el estudio de la dinámica de las moléculas disociadas muestra que el proceso de disociación es directo y ocurre siguiendo caminos de disociación muy estrechos. La mayoría de las moléculas se disocian muy cerca de los átomos de hierro de la tercera capa atómica y con una orientación de su eje molecular paralela a la superficie. Además, incluimos una comparación entre nuestro trabajo y trabajos anteriores en la superficie (110) del hierro para entender la diferencia en reactividad entre las dos superficies. La cara (111) es más reactiva que la (110), principalmente por la reducción de las barreras energéticas en la aproximación de la molécula de N_2 a la superficie en el caso de la primera de estas caras, una conclusión que es consistente con los estudios experimentales.

Por último, hemos estudiado los efectos isotópicos en la dinámica de abstracción Eley-Rideal (ER) de átomos de hidrógeno y sus isótopos en las superficies de tungsteno

W(100) y W(110), en el límite de un adsorbato aislado. En general, hemos encontrado que las secciones eficaces ER son relativamente pequeñas. Además, las secciones eficaces en el caso de la cara (100) son mayores que las correspondientes a la cara (110). La sección eficaz para el caso de D₂ es independiente del valor de la temperatura en la superficie, una conclusión que concuerda con estudios previos para átomos de hidrógeno. Dentro de la aproximación BOSS, mostramos que las secciones eficaces ER tienen una clara dependencia con el cociente entre la masa del proyectil y la masa del blanco (m_p/m_t). Las secciones eficaces ER son casi idénticas para combinaciones homonucleares, son mayores cuando el cociente m_p/m_t es mayor que uno y menores cuando m_p/m_t es menor que uno. Este efecto está relacionado con la mayor (menor) probabilidad de reflexión del átomo incidente cuando es pesado (ligero). En ambas superficies, la reacción ER se produce a partir de una colisión del átomo incidente con el adsorbato, después de haber rebotado aquel en uno de los átomos de tungsteno de la superficie, en un rebote que redirige al átomo incidente hacia el blanco. Además, aparecen efectos isotópicos en los estados finales de las moléculas formadas. La mayoría de la energía disponible se transfiere al movimiento traslacional de la molécula que se desorbe de la superficie. Nuestros resultados muestran un buen acuerdo con medidas experimentales de las distribuciones vibracionales moleculares a temperatura ambiente. En resumen, el trabajo presentado en este manuscrito prueba una vez más que los estudios teóricos basados en cálculos de primeros principios son herramientas muy precisas para describir, entender y predecir la dinámica de los procesos reactivos elementales en superficies.

Publications

- **Density Functional Theory Study of Nitrogen Atoms and Molecules Interacting with Fe(111) Surfaces**

M. A. Nosir, L. Martin-Gondre, G. A. Bocan, and R. Díez Muiño;

Nuclear Instruments and Methods in Physics Research Section B: Beam Interactions with Materials and Atoms, **382**, 105, 2016.

- **Adsorption Dynamics of Molecular Nitrogen at a Fe(111) Surface**

M. A. Nosir, L. Martin-Gondre, G. A. Bocan, and R. Díez Muiño;

Submitted

- **Dissociative Adsorption Dynamics of Nitrogen at a Fe(111) Surface**

M. A. Nosir, L. Martin-Gondre, G. A. Bocan, and R. Díez Muiño;

In preparation

- **Isotope Effects in Eley-Rideal and Hot-Atom Abstraction Dynamics of Hydrogen from Tungsten (100) and (110) Surfaces**

R. Pétuya, M. A. Nosir, C. Crespos, R. Díez Muiño, and P. Larrégaray;

The Journal of Physical Chemistry C, **115**, 15325, 2015.



This work has been partially supported by the Basque Departamento de Educación, Universidades e Investigación, the University of the Basque Country UPV/EHU (Grant No. IT-756-13) and the Spanish Ministerio de Economía y Competitividad (Grants No. FIS2013-48286-C02-02-P and FIS2016-76471-P). I acknowledge financial support by the Ministerio de Economía y Competitividad (Grant No. BES-2011-045536). Computational resources were provided by the DIPC Computing Center.